

UNIVERSITY OF SURREY

DOCTORAL THESIS

High Precision Measurements of Isomeric States in $^{94,96}\text{Pd}$ and ^{94}Ru

Author:
Shaheen Jazrawi

Supervisors:
Prof. Patrick Regan
Dr. Daniel Doherty
Dr. Giuseppe Lorusso

*A thesis submitted in fulfilment of the requirements
for the degree of Doctor of Physics*

in the

Department of Physics
Faculty of Engineering and Physical Sciences

23rd September 2022

Declaration of Authorship

I, Shaheen Jazrawi, declare that this thesis titled, 'High Precision Measurements of Isomeric States in $^{94,96}\text{Pd}$ and ^{94}Ru ' and the work presented in it are my own. I confirm that:

- This work was done wholly or mainly while in candidature for a research degree at this University.

Signed: S. Jazrawi

Date: 12th January 2023

Abstract

This thesis presents the first results using the FAst TIMing Array (FATIMA) spectrometer for electromagnetic transition rate measurements within the NuSTAR facility at GSI-FAIR phase-0. The Monte-Carlo simulated response for gamma-ray detection by FATIMA for exploitation within the the DEcay SPECtroscopy (DESPEC) experimental system at the FAIR Phase-0 facility at Darmstadt, Germany is presented. In this configuration, FATIMA consisted of 36 LaBr₃(Ce) detectors surrounding the AIDA, position sensitive charged-particle active stopper detection system. The decay of the I^π=8⁺ isomerically decaying cascade in ⁹⁶Pd was measured in the first DESPEC experiment at the FAIR-0 facility following the projectile fragmentation of a ¹²⁴Xe primary beam incident on a ⁹Be target and was used to validate the simulations. The experimental data yielded full energy peak efficiency values for FATIMA of 11.2(11)%, 6.8(7)%, 3.8(6)% and 2.1(5)% at 106 keV, 325 keV, 684 keV and 1415 keV respectively, consistent with the values derived from the simulated GEANT4 response. This thesis also reports on the scientific output of the first experiment of the DESPEC Phase-0 campaign at GSI, which focussed on the study of neutron-deficient nuclei approaching ¹⁰⁰Sn. Results are presented on electromagnetic transition rates associated with the decays from excited states populated following the formation of I^π = 8⁺ proton ‘seniority isomer’ states in the N = 50 isotones ⁹⁴Ru and ⁹⁶Pd and the I^π = 14⁺ isomer in ⁹⁴Pd. Direct half-life measurements via $\gamma-\gamma$ coincidences using the FATIMA detector array have been used to determine the reduced matrix elements associated with decays between low-lying states in these semi-magic nuclei. The extracted half-lives for the yrast I^π = 6⁺ and 4⁺ states in ⁹⁶Pd were measured to be 6.4(4) ns and 1.0(1) ns respectively with a prompt decay observed from the 2⁺ to ground state. Additionally, the 8⁺ and 6⁺ yrast states in ⁹⁴Ru were measured to posses half-lives of 64(1) μs and 63(4) ns respectively. These measurements are consistent with the published, highest-precision values for these nuclei. The data on ⁹⁴Pd provide the first measurement of the B(E2:8⁺ → 6⁺) for this N = 48 nucleus at 5.3(1)×10⁻³ e²b² for a half-life of 1.2(3) ns. The measured B(E2) value compare favourably with predictions from state-of-the-art shell model calculations using the Gross-Fenkel and JUN45 interactions assuming a closed ⁷⁶Sr₃₈ core.

Acknowledgements

First and foremost I must give a huge thank you to my PhD supervisor, Professor Patrick Regan. To be the latest in the line of his PhD students has truly been an honour and his years of experience as a supervisor have shone through over the course of my studies. He has provided me with incredible opportunities to travel around the world to present my work and collaborate with exceptional nuclear physicists, allowing me to expand my physics knowledge as well as my viewpoints of the world. Not only is he an excellent physics Professor who has acted as a vast source of academic knowledge and advice, but he has shown me time and time again that he is an exceptionally personable and kind human being. I will forever appreciate the wisdom, knowledge and pep talks over the course of my PhD. Dr Daniel Doherty and Dr Giuseppe Lorusso have been excellent secondary and industrial supervisors who have always been available to explain concepts, assist me and provide guidance and insight for my work whenever needed, which I am very grateful for. The work done in this PhD was sponsored by the STFC along with an iCase sponsorship from the National Physical Laboratory. I would like to acknowledge and thank both the STFC and NPL for their financial support provided for the last four years as these organisations made my work possible.

I hold a huge appreciation for everybody I came across at the University of Surrey Physics department throughout my 8 years of study there. Everybody I have met and worked with through my undergraduate and PhD has been exceptionally friendly and kind to me, especially those students who I shared the PhD office with - I have no doubt that every one of them will go on to do great things when they finish at Surrey, be that in academia or industry, with many of them already having done so. A special thanks must go out to Dr Gavin Lotay who gave me the opportunity to carry out an incredible 6 month placement at TRIUMF Labs, Vancouver. I must also extend my thanks to the Nuclear Metrology group at NPL, firstly for offering me a fascinating MPhys year research project in 2017 then welcoming me back in 2018 to begin a new chapter of research. The entire group has always been nothing but friendly to me, incredibly inclusive and a joy to be around. A special mention must go to Robert Shearman and Sean Collins, respective former and current students of Paddy who have always provided me with valuable advice and encouragement along with many laughs and interesting conversations throughout my MPhys year and PhD. I also extend my gratitude to all those involved in the DESPEC collaboration at GSI, as this thesis would not exist without the hard work and effort put in by the local and external teams.

My parents, Fariba and Mahmood, thank you for making the brave decisions to leave your war torn countries which led to you meeting in the UK and starting a warm, loving family. Your strength, courage, love and unwavering belief in me has made me

the person I am today. I can never repay the debt that I owe you, no child ever could, but I promise that I will do my best to continue to make you proud. Thank you to my beautiful brother and sister, Behdeen and Shereen for the fond memories that we made together growing up, I will treasure them forever and look forward to making many more.

Finally, I would like to thank the many friends I have made along the way. I could not have asked for better flatmates upon my first year of arriving at Surrey. To Kathleen, Siobhan, Ted and Cam - thank you for the good times and laughs, I learned a lot from you. Last but by no means least I must thank my closest friends; Ieuan, Ryan, John, James, Lyall and Richard. Thank you for being there for me when I've needed you, the intriguing discussions we've had over the years, the compliments when I've deserved them and the ego checks when I've needed them - here's to many more. I am eternally grateful to have met you, thank you for your friendship, I love you all.

Writing these acknowledgements has allowed me to truly appreciate my irreplaceable friends, family, supervisors and colleagues who have supported me over the years along with the amazing opportunities I have been presented with. I wish you all nothing but the best of fortune. I am very lucky.

Contents

Declaration of Authorship	i
Abstract	ii
Acknowledgements	iii
Contents	v
List of Figures	viii
List of Tables	xiii
1 Introduction	1
1.1 Introduction	1
1.2 Physics Motivation	2
1.3 Thesis Outline	8
2 Nuclear Structure Theory	9
2.1 The Independent Particle Shell Model	9
2.1.1 The Nuclear Shell Model	9
2.1.2 The Nuclear Potential	10
2.1.2.1 The Woods-Saxon Potential	10
2.1.2.2 The Spin-Orbit Potential	12
2.1.3 Configuration Mixing	13
2.1.4 Nuclear Isomerism	15
2.1.4.1 Seniority	15
2.1.5 Nuclear Decay	15
2.1.5.1 Beta Decay	15
2.1.5.2 Internal Conversion	18
2.2 Electromagnetic Transitions Between Excited Nuclear States	18
2.2.1 Characteristics of EM Transitions	19
2.2.2 EM Transition Rates in Nuclei	19
2.2.3 Weisskopf Single-Particle Estimates	20
2.3 Enhanced Shell Model Calculations	21

3 Experimental Considerations	24
3.1 Gamma-Ray Interaction Cross-sections	24
3.1.1 Operation of Semiconductor Detectors	24
3.1.2 Operation of Scintillation Detectors for Gamma-ray Spectroscopy .	25
3.2 Nuclear Reaction Mechanisms	26
3.2.1 LISE++ Simulations	27
3.2.2 Projectile Fragmentation Reaction.	27
3.3 Interaction of Gamma rays with Matter	28
3.3.1 Compton Scattering	30
3.3.2 Photoelectric Effect	30
3.3.3 Pair Production	31
3.4 The GSI Accelerator System	31
3.5 The Fragment Recoil Separator	32
3.6 The DESPEC @ GSI Set-up for S480	34
3.6.1 AIDA	35
3.6.2 β -Plastic	35
3.6.3 High Purity Germanium	36
3.6.4 The FAst TIming Array - FATIMA	36
3.7 Event Building	38
3.7.1 MBS	38
3.7.2 White Rabbit	39
3.7.3 ucesb Timestitching	40
4 Gamma-ray Spectroscopy using DeSPEC	41
4.1 Experimental Details	41
4.2 Particle Identification Spectra and Gating	41
4.3 Gamma-ray Analysis	51
4.3.1 Previously Reported Isomeric States	51
4.3.2 Isomer Half-life Measurements	56
4.3.3 Determination of FATIMA Full Energy Peak Detection Efficiency .	59
4.3.4 Calculation of Isomeric Ratios	62
4.4 DESPEC NPTool Simulation	66
5 Fast Timing Measurements and Discussion	74
5.1 Fast Timing Results	74
5.1.1 Transitions Populated Following the Decay of the 8^+ Isomer in ^{96}Pd .	75
5.1.2 Transitions Populated Following the Decay of the 14^+ Isomer in ^{94}Pd	78
5.1.3 Transitions Populated Following the Decay of the 8^+ Isomer in ^{94}Ru	82
5.1.4 Calculation of B(E2) Values	85
5.2 Comparison of Results With Shell Model Calculations	85
6 Conclusion	88
6.1 Future Work	89
A Research Outputs	91

A.1 Main Author Publications	91
A.2 Other Publications as Contributing Author	91
A.3 Presentations Given	92
A.3.1 Oral Presentations	92
A.3.2 Poster Presentations	93
 Bibliography	 94

List of Figures

1.1	The region of interest on the nuclear chart this work pertains to. Nuclei with only the ground state half-lives known and no excited states reported are highlighted with a yellow square with the nuclei to the left of them having only been produced experimentally. Taken from [24].	3
1.2	A side by side comparison between experimental results from [26, 40] and shell model calculations in the pg space from [34]. The figure shows the evolution of the proton-neutron interaction and even-parity yrast structure. Taken from reference [41].	5
1.3	The experimental level scheme of excited states in ^{94}Pd [11, 14, 15, 42, 43] along with shell model calculations from varying model spaces [11, 34]. Previously reported $I^\pi = 19^-$ and 14^+ isomeric states are reported in red with reported half-lives of 197(22) ns and 499(13) ns respectively [11]. Taken from reference [41].	6
1.4	The partial decay schemes of ^{94}Pd (left) and ^{96}Pd (right) below their isomeric 14^+ and 8^+ states respectively [11, 16, 44].	7
2.1	A plot showing the trend of first ionisation energies across the periodic table. Peaks in ionisation energies are seen in the noble gases (and mercury) as a result of filled p sub-shells, implying a heightened binding energy [47].	10
2.2	A plot displaying the 2 neutron and 2 proton separation energies for a number of nuclei across the nuclear chart. The neutron and proton magic numbers are circled and the "magic nuclei" are shown to have heightened separation energies reflecting an increased stability [49].	11
2.3	The independent particle shell model configuration in which nucleons are arranged. The effects of l.s coupling are represented on the right of the diagram in the form of sub-shells which combine to form filled shells, giving rise to the magic numbers indicated in bold. The degeneracy of each subshell is shown to its right and is equal to $2j+1$. Adapted from [49].	23
3.1	A schematic describing the operation of a scintillation detector. The absorption of a gamma ray leads to the de-excitation of an electron from the crystal, releasing a photon which in turn interacts with the photocathode. Here, an electron is released which is multiplied through the use of a photomultiplier tube. The number of electrons is proportional to the energy of the original incident gamma ray.	26
3.2	The projectile fragmentation process used at various particle accelerator facilities to create nuclear species of interest.	28
3.3	A plot displaying the cross-sections of the competing processes by which gamma rays interact with matter at different energies. Taken from [75] . .	29

3.4	A schematic of the beam production and delivery system at GSI taken from [78].	32
3.5	A diagram detailing the path a beam takes through the FRS and the magnets which are used to steer the beam, adapted from figure 7 of reference [79].	33
3.6	A photograph of the DESPEC set-up in March 2020 as used for the commissioning run of the set-up.	34
3.7	A photograph showing an interior view of the FATIMA array taken at GSI in March 2020.	37
3.8	A flowchart explaining the datastream coming from the various DESPEC detectors showing the processes which combine them into coherent analysable data. Taken from reference [8].	39
4.1	The measured, calibrated Z vs A/Q matrix for nuclei passing through the FRS from a subset of the data from S480.	42
4.2	The γ rays detected by the FATIMA array between 40 ns and 400 ns after prompt implantation when gating on ^{96}Pd ions seen in the Z vs A/Q matrix.	43
4.3	The γ rays detected by the FATIMA array between 40 ns and 400 ns after prompt implantation when gating on ^{94}Pd ions seen in the Z vs A/Q matrix.	43
4.4	The γ rays detected by the germanium detectors between 500 ns and 6 μs after prompt implantation when gating on ^{96}Pd ions seen in the Z vs A/Q matrix.	44
4.5	The γ rays detected by the germanium detectors between 500 ns and 6 μs after prompt implantation when gating on ^{94}Pd ions seen in the Z vs A/Q matrix.	44
4.6	The Z vs A/Q of ions generated in the FRS detected in coincidence with a 106 keV γ ray detected by FATIMA 40 ns - 400 ns after prompt implantation (upper), the background region of 106 keV (central) and the subtraction of the central plot from the upper plot (bottom).	45
4.7	The Z = 46 projections of the Z vs A/Q of ions measured in the FRS detected in coincidence with the 106 keV (upper), 684 keV (central) and 1415 keV (bottom) transitions in ^{96}Pd measured 40 ns to 400 ns after prompt implantation. These spectra have been background subtracted and the γ rays of interest were detected post-prompt.	46
4.8	The Z = 46 projection of the Z vs A/Q of ions generated in the FRS detected in coincidence with the 96 keV (upper), 659 keV (central) and 814 keV (bottom) transitions in ^{96}Pd measured 40 ns to 400 ns after prompt implantation. These spectra have been background subtracted and the γ ray of interest were detected post-prompt.	47
4.9	The Z = 46 projection of the Z vs A/Q of ions generated in the FRS detected in coincidence with the 905 keV (upper), 994 keV (central) and 1092 keV (bottom) transitions in ^{94}Pd measured 40 ns to 400 ns after prompt implantation. These spectra have been background subtracted and the γ rays of interest were detected post-prompt.	48
4.10	The SC41-42 energy spectra when gating on the prompt-delayed γ rays seen in FATIMA from the decays of ^{96}Pd (1415 keV) and ^{94}Pd (1092 keV). The black ellipse indicates the location of the resulting gate.	49

4.11	The β -Plastic Time Over Threshold (TOT) signal seen when gating on the prompt-delayed γ rays seen in FATIMA from the decays of ^{96}Pd (1415 keV) and ^{94}Pd (1092 keV).	50
4.12	The location of ions deposited in AIDA detected in coincidence with 1415 keV (blue) and 1092 keV (red) gamma rays from ^{96}Pd and ^{94}Pd ions, detected in FATIMA.	51
4.13	The γ -ray energy versus detected by FATIMA versus FATIMA - SC41 time difference when gating on the Z versus A/Q of ^{96}Pd ions seen in the FRS. Additional gating conditions are also applied on energy deposited in scintillators 41 and 42, the β -Plastic Time over Threshold (ToT) and the 'stopped' tag in AIDA	52
4.14	The γ -ray energy versus detected by FATIMA versus FATIMA - SC41 time difference. These events are gated on the Z vs A/Q of ^{94}Pd ions seen in the FRS and the energy deposited in scintillators 41 and 42.	52
4.15	The different ^{96}Pd γ -ray spectra from isomeric cascades when gating on the different particle detectors in the DESPEC set-up.	53
4.16	The different ^{94}Pd γ -ray spectra from isomeric cascades when gating on the different particle detectors in the DESPEC set-up.	53
4.17	The γ -ray energy vs time difference with respect to scintillator 41 matrix measured by the GTC array when gating on ^{96}Pd detected in the FRS.	54
4.18	The γ -ray energy vs time difference matrix measured by the GTC array when gating on ^{94}Pd detected in the FRS.	55
4.19	The FATIMA energy versus White Rabbit time difference with respect to the FRS for ^{94}Ru events. The 1431 keV transition partially overlaps with the activity associated with the internal decay in ^{138}La	56
4.20	Gamma ray singles projections for ^{96}Pd (above) and ^{94}Pd (below) showing the energy cascades below the isomeric 8^+ and 14^+ states respectively. The decay curves seen in the insets were created by summing the background subtracted time projections of each individual transition (not including those below 200 keV) which was detected between 0 μs - 8 μs and fitting them with a single component exponential over a time range of 0.1 - 6.0 μs	57
4.21	Gamma rays detected following the decay of the 8^+ isomeric state in ^{94}Ru within the White Rabbit timing range of a) the decay region of 80 μs to 350 μs , b) the background region 350 μs to 620 μs and c) spectra b subtracted from spectra a to form a normalised background subtracted spectra.	58
4.22	A singles γ -ray spectrum of the ^{94}Ru isomeric cascade generated from the extended timing window of the FATIMA - FRS White Rabbit time differences over the range of 80 μs - 350 μs . A background subtraction has been carried out whereby the region from 350 μs - 620 μs was taken away to minimise the impact of background peaks. The inset shows a combination of background subtracted timing projections on the 146 keV, 311 keV, 755 keV and 1431 keV γ -ray transitions in ^{94}Ru with an exponential plus linear background fit over a range of 150 μs - 650 μs	59

4.23 A set of gamma-ray spectra showing a) the singles FATIMA spectra projected on events detected 40 ns - 400 ns after the prompt flash, b) the total projection of a $\gamma - \gamma$ matrix sorted with a condition that two gamma rays had to arrive at FATIMA detectors within 40 ns of each other and c) through to f) showing the various coincidence gated projections of the $\gamma - \gamma$ matrix.	61
4.24 Weighted mean values for the calculated γ -ray full-energy peak efficiencies for the 106 keV, 325 keV, 684 keV and 1415 keV transitions associated with the decay of the isomeric 8^+ state. The dashed line represent the uncertainties in the weighted mean averages for each transition.	62
4.25 The decays of the ^{96}Pd and ^{94}Pd isomers through the separator. The dashed lines represent the timing window which FATIMA was used to measure decays. A clear change in the decay regimes can be seen to occur for both nuclei at 325 ns which is the time of flight through the separator. The neutral atom half-life used in equation 4.5 for the 8^+ state in ^{96}Pd is equal to to 1.81(1) μs while the fully stripped ion has a half-life of 3.86(2) μs . Similarly the 14^+ state in ^{94}Pd has a half-life of 499(9) ns as a neutral ion and 1.32(3) μs when fully stripped. These increased half-lives are associated with the internal conversion coefficients from the 106 keV and 96 keV E2 transitions from these states in ^{96}Pd and ^{94}Pd respectively.	64
4.26 The singles γ rays detected in FATIMA gated on the different ion species seen in the FRS projected across the time ranges.	65
4.27 The isomeric ratios of the isomeric states in ^{96}Pd , ^{94}Pd and ^{94}Ru . Each data point was calculated using a different energy transition and were combined using weighted means to determine a final value. The solid lines correspond to the final value of the isomeric ratio for each nuclei and the dashed lines show the margin of error.	66
4.28 The GEANT4/NPTool simulation representation of the DESPEC set-up featuring the 36 FATIMA detectors.	67
4.29 A GEANT4 simulated spectra for FATIMA run with 10^6 simulated events. The simulation emulates the $I^\pi = 8^+$ isomeric cascade in ^{96}Pd for a source placed in the centre of the array with the DESPEC configuration.	68
4.30 A GEANT4 simulated spectra displaying the FATIMA response for 10^6 decays of ^{241}Am , ^{109}Cd , ^{57}Co , ^{139}Ce , ^{51}Cr , ^{83}Sr , ^{137}Cs , ^{54}Mn , ^{88}Y , ^{65}Zn and ^{60}Co	69
4.31 A comparison between the full energy peak efficiencies measured in experiment S480 and those simulated through the mixed γ -ray source.	70
4.32 A measure of the value of the σ of Gaussian peaks in FATIMA vs gamma ray energy. A power law fit was used to determine the relationship $\sigma = 0.92E^{0.39}$	71
4.33 FATIMA spectra comparing the experimental (black) and simulated (red shaded) responses for decays of the ^{96}Pd isomer for decays between 40 and 400 ns following implantation in AIDA. The simulated spectra was generated for 97,970 isomeric cascades in this timing window. The figures show a) singles spectra and b) total projections for the coincidence matrices. c) - f) show the background subtracted coincidence spectra gated on the 106 keV, 325 keV, 684 keV and 1415 keV transitions respectively.	72

5.1	Background subtracted $E_\gamma - E_\gamma$ coincidence spectra for isomer delayed events gated on ^{96}Pd with the conditions that both gamma rays were detected between 40 and 400 ns after the implantation in AIDA.	75
5.2	Background subtracted $E_\gamma - E_\gamma$ coincidence spectra for isomer delayed events gated on ^{96}Pd with the conditions that both gamma rays were detected between 40 and 400 ns after the implantation in AIDA.	76
5.3	The ^{96}Pd isomer gated time difference spectra for the $8^+ \rightarrow 6^+ \rightarrow 4^+ \rightarrow 2^+ \rightarrow 0^+$ yrast decay sequence using FATIMA at DESPEC. The time spectra are fitted to a single exponential decay function between 2 and 40 ns after the nominal $\Delta T = 0$ time.	77
5.4	The FATIMA gamma-rays energy vs FATIMA - SC41 time difference spectra resulting from a gate on ^{96}Pd ions from the FRS detectors, a high energy ion event in the bFast plastic scintillation detector, a clean signal through the SC41 and SC42 scintillators and an implantation in AIDA.	78
5.5	The FATIMA - FATIMA TDC time differences for various combinations of start stop timing conditions. The plots show from the top row left to right the 2^+ , 4^+ and 6^+ half-lives which all appear to be prompt transitions. The central plot and the plot to its right show the 10^+ and 12^+ half-lives which are also prompt. The central-left plot in red shows the half-life of the state of interest with a half-life value of 1.2(3) ns. The bottom row of figures from left to right show a series of time difference plots gated above and below the 8^+ state.	79
5.6	Time difference figures for isomeric transitions above and below the 8^+ state in ^{94}Pd . The top figure shows the combinations of transitions above the state while the bottom figure shows those time differences for the combinations below. The central figure is a measurement of the half-life of the 8^+ state fit with an exponential decay function. This plot was constructed by using all gamma rays above the state as a start condition and any of those below as a stop.	81
5.7	The background subtracted $\gamma - \gamma$ coincidence spectra for isomer delayed events gated on ^{94}Ru with the condition that the gamma rays were detected between 80 μs and 350 μs after the implantation in the AIDA stopper. The EC label represents the La K x-rays in coincidence with the 1436 keV $2^+ \rightarrow 0^+$ transition in ^{138}Ce arising from the internal activity of the $\text{LaBr}_3(\text{Ce})$ detectors.	83
5.8	^{94}Ru isomer-gated time difference spectra for the $8^+ \rightarrow 6^+ \rightarrow 4^+ \rightarrow 2^+ \rightarrow 0^+$ yrast decay sequence using the FATIMA system at DESPEC. The time spectra are fitted to a single exponential decay function between 2 and 300 ns after the nominal $\Delta T = 0$ time.	84
5.9	A plot comparing the Gross-Fenkel and JUN45 interaction force predictions of the $B(E2)$ values of the transitions below the isomeric cascade in ^{96}Pd	86
5.10	A plot comparing the Gross-Fenkel and JUN45 interaction force predictions of the $B(E2)$ values for the transitions below the isomeric cascade in ^{94}Pd	87
6.1	The schematic of the proposed IDATEN array consisting of 36 1.5" x 2" $\text{LaBr}_3(\text{Ce})$ FATIMA detectors, 48 1.5" x 1.5" $\text{LaBr}_3(\text{Ce})$ KHALA detectors and 2 SNU clover type HPGe detectors taken from work done by Y. Jang.	90

List of Tables

2.1	A summary of the angular momentum and parity selection rules of β decay from reference [49].	17
2.2	A summary of the properties of different orders of electromagnetic transitions.	20
2.3	A table listing the Weisskopf estimates for electric and magnetic single particle transition rates. A is the atomic mass of the nucleus and E is the energy in MeV.	21
3.1	A summary of the timestamp accuracy of the White Rabbit clock for the different DESPEC subsystems depending on their timing electronics.	40
4.1	A summary of the measured half-lives and isomeric ratios of ^{96}Pd , ^{94}Pd and ^{94}Ru	66
5.1	A summary of the half-life measurements and calculated $B(E:I \rightarrow I-2) \downarrow$ values in ^{96}Pd , ^{94}Pd and ^{94}Ru . The literature values are taken from [12, 44] and the internal coefficients are taken from the BRICC database [53].	85

Dedicated to my family and friends.

Chapter 1

Introduction

1.1 Introduction

Today's understanding of the atom as a small concentrated collection of protons and neutrons surrounded by a cloud of electrons required much research and experimentation to develop. It is through this route that the field of nuclear physics aims to uncover and explain the interactions of protons and neutrons which make up the nucleus of the atom. The best way to study these interactions is to take measurements of the radiation which is emitted from nuclei in unstable states but one must go through the tasks of creating these nuclei within measurable conditions along with the instrumentation required to detect and measure the outgoing radiation. By then comparing experimentally collected data with predictions from theoretical models it is possible to further the understanding of nuclear structure across the nuclear chart.

The NuSTAR collaboration based at the Facility for Antiproton and Ion Research (FAIR) radioactive-ion beam facility in Germany currently conducts research focussed on radioactive nuclei with abnormal combinations of protons and neutrons. The FAIR Phase-0 GSI facility [1–3] provides radioactive and stable beams which can then be transported through the Fragment Recoil Separator (FRS) to the DEcay SPECtroscopy (DESPEC) radiation detection system. The setup is a state-of-the-art multi-modal radiation detection system with the ability to experimentally discern the half-lives of isomers and the low-lying states in exotic, neutron-deficient radioisotopes. The DESPEC setup consists of a number of different radiation detection arrays; the LaBr₃(Ce) gamma-ray scintillation detector FAst TIMing Array (FATIMA)[4, 5], the Advanced Implantation Detector Array (AIDA) [6], the β Plast plastic scintillation detector, seven Galileo Triple Cluster (GTC) High Purity Germanium (HPGe) detectors as well as various scintillators

used for Time of Flight (ToF) measurements. All of these subsystems may be used to view data in coincidence mode or singles.

In the work done in this thesis FATIMA consisted of 36 individual 2" x 1.5" LaBr₃(Ce) detectors with a full width at half maximum (FWHM) energy resolution of 3.4 keV at 662 keV [7]. These along with the seven GTC HPGe detectors made up the gamma ray detection portion of the array and surrounded the AIDA active stopper which is made up of three stacked Double Sided Silicon Strip Detectors (DSSSDs), sandwiched between two fast plastic ' β -Plastic' particle detectors. A more detailed and recent review of the range of equipment associated with the DESPEC collaboration with alternative configurations can be found in [8]. Additionally, number of experiments have since been performed using DESPEC to measure isomeric and beta-delayed spectroscopy in exotic radioisotopes [9, 10].

One focus of this thesis is the simulated full-energy peak efficiency performance of FATIMA for DESPEC experiments. A Monte-Carlo Model of the setup for its configuration in the commissioning run, experiment S480, has been created for this comparison. The simulations were performed using the open source analysis frame work Nuclear Physics Tool (NPTool) which is based on the GEANT4 simulation package. The NPTool package offers modular approach for the design, simulation and analysis of complex multi-faceted radiation and particle detection arrays which can be analysed in coincidence mode. These gamma-ray simulations were validated by directly comparing the simulated output with experimental data from the commissioning run of the DESPEC setup which was performed in March 2020 at FAIR Phase-0. This thesis will also present the fast-timing analysis from experiment S480 and will focus on the decay properties of previously reported isomeric states in three radionuclides - ⁹⁶Pd, ⁹⁴Pd and ⁹⁴Ru [11–17]. The isomeric ratios and half-lives of the 8+, 14+ and 8+ states in ⁹⁶Pd, ⁹⁴Pd and ⁹⁴Ru respectively were measured along with the half-lives of the shorter lived states below the isomer. These half-lives may be used to calculate B(E2) values which can be used to provide validation for shell model calculations pertaining to the effect of the seniority interaction on nuclei near ¹⁰⁰Sn.

1.2 Physics Motivation

Tin-100 is the heaviest stable, self-conjugate doubly-magic nucleus with 50 protons and 50 neutrons. The region 'south-west' of the ¹⁰⁰Sn shell closure highlighted in figure 1.1 to the N = Z line is dominated by the interactions within the 0g_{9/2} intruder orbit from the N = 4 harmonic oscillator shell. These are separated well from the N = 3 pf orbitals by energy and parity which allow only 2 particle, 2 hole excitations into the orbital

space. A new quantum number, seniority, is required in the n-particle wave functions [18–21]. Seniority is a measure of the number of unpaired nucleons occupying the same shell-model orbital. The $0g_{\frac{9}{2}}$ orbit gives rise to interesting structural phenomena such as spin-gaps, seniority and parity changing isomerism, pn pairing as well as seniority-induced symmetries which all arise due to the dominant proton-neutron interaction [22, 23]. Resultantly, the region to the south-west of ^{100}Sn has and continues to be an interesting area of research for theoretical and experimental nuclear physics.

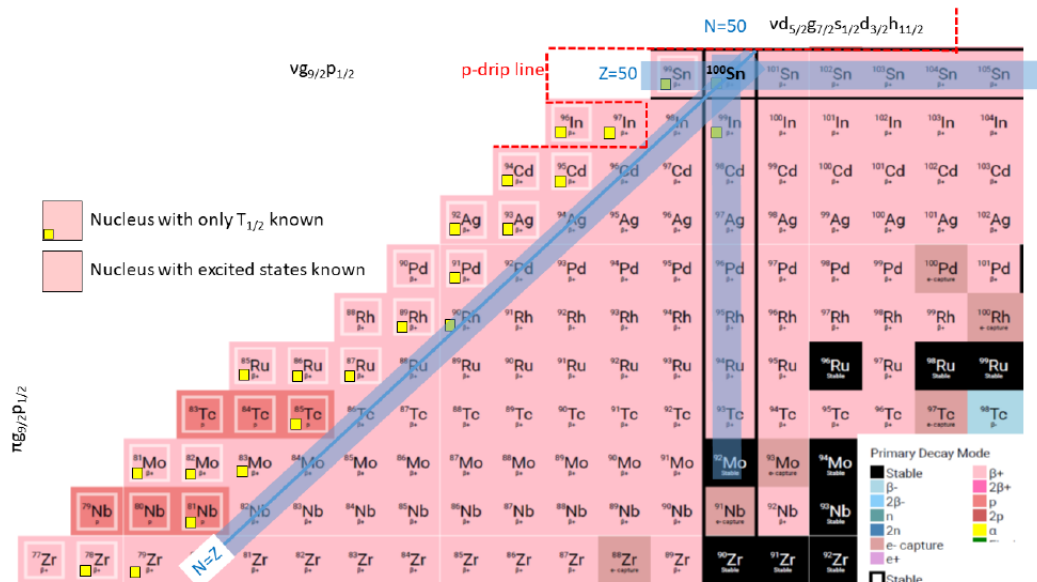


FIGURE 1.1: The region of interest on the nuclear chart this work pertains to. Nuclei with only the ground state half-lives known and no excited states reported are highlighted with a yellow square with the nuclei to the left of them having only been produced experimentally. Taken from [24].

A number of long standing theoretical questions about the behaviour of shell model states approaching ^{100}Sn [1, 25] motivate this study and in particular the competing seniority coupling associated with proton $g_{\frac{9}{2}}$ sub-shell excitations at $N = 50$ and pn pairing effects which are competitive at the $N = Z$ line [14, 26]. These questions include the evolution of single particle shell structure, the robustness of shell closure, the proton-neutron interaction at $N=Z$ and pn pairing, the validity of the seniority scheme and the distortion between competing cross-shell excitations from the lower $N = 3$ to the higher $N = 4$ orbitals.

A review of studies employing empirical interactions in the $(1p_{\frac{1}{2}}; 0g_{\frac{9}{2}})$ model space can be found in [1]. Large Scale Shell Model (LSSM) calculations have also been carried out for the full $\pi\nu(f_{\frac{5}{2}}pg_{\frac{9}{2}})$ [2] as well as the upper $\pi\nu(sdg)$ shell using the Nowacki-Sieja interaction [27] with remnants of the seniority level scheme in the $\pi\nu g_{\frac{9}{2}}$ shell having also been addressed. Recent experimental highlights include the discovery of core-excited

isomers in ^{98}Cd [7, 10], ^{96}Ag [28] as well as the spectroscopy of the $N = Z$ nucleus ^{92}Pd [26] and the decay of the ^{96}Cd [29] isomer and the $I^\pi = 16^+$ spin trap isomer [30]. Additional work has also been done on the comprehensive isomer, beta-delayed and beta-p decay spectroscopy of the projectile fragmentation products in the region [12, 31, 32].

The $\pi\nu$ interaction strength in the $\pi\nu g_{\frac{9}{2}}$ orbit manifests itself most clearly in the strongly binding $T = 0$ ($g_{\frac{9}{2}}$) $I^\pi = 9^+$ Two-Body Matrix Element (TBME) which is comparable with the $T = 1$ pairing [33, 34]. The role of $\pi\nu g_{\frac{9}{2}}$ pairs with a maximum 9^+ spin in the $N = Z$ nuclei ^{96}Cd , ^{94}Ag and ^{92}Pd has been investigated through the use of multi-step shell model and Interacting Boson Model (IBM) studies with respect to the dependence on the powerful 9^+ Two Body Matrix Element (TBME) [26, 35–38]. While the $\pi\nu$ -pairs in these nuclei were discussed at increasing spins the overlap with the 9^+ boson wave functions could only be established for low and high spin states with little overlap discovered for intermediate spin [38]. These conclusions were subject to changes when the full $\pi\nu(f_{\frac{5}{2}}pg_{\frac{9}{2}})$ and $\pi\nu(sdg)$ spaces are brought into effect.

Comparisons between these model spaces are made to a pure $\pi\nu g_{\frac{9}{2}}$ approach by comparing the $B(E2)$ values and spectroscopic quadrupole moments in ^{96}Cd and ^{92}Pd . The different approaches share likeness in excitation energies and $B(E2)$ values but display substantial differences in the quadrupole moments which are currently inaccessible by experimental means. Conclusions were being drawn which expect changes to be seen for higher spins close to the magic numbers due to model space exhaustion. This places ^{94}Pd at a pivotal point in this structural evolution as it is the even-even neighbour of the $N=Z$ systems of ^{92}Pd , ^{96}Cd and ^{94}Ag , being the $T = 1$ variant of the silver isotope. On the seniority front it reflects the $\nu p = 2,4$, $\nu\pi = 2$ transition from $\nu = \nu\pi = 2,4$ ^{92}Pd to the $\nu = 2$ ^{96}Cd with an intermediate $B(E2: I \rightarrow I - 2)$ pattern in $\pi g_{\frac{9}{2}}$ [39].

Figure 1.2 shows a comparison between the experimental spectra of $^{92-96}\text{Pd}$ with the shell model results from [34] in order to highlight the role of the isoscalar $T = 0$ versus the isovector $T = 1$ interaction. The evolution of the seniority type $N = 50$ $^{96}\text{Pd}_{50}$ to $^{92}\text{Pd}_{46}$ comes from the strong $T = 0$ interaction while the $T_z = 1^+$ nucleus ^{94}Pd displays an intermediate character. A vibrational style spectra is seen for ^{92}Pd below $I^\pi = 12^+$ mainly resulting from the $T = 0$ part of the $\pi\nu$ interaction while the $T = 1$ part maintains the seniority type ^{96}Pd spectrum. The transition point of ^{94}Pd violates this with a decrease in energy of the $\nu = 4$ $I^\pi = 6^+$ state from the $\pi\nu$ interaction through a small $I^\pi = 8^+ \rightarrow 6^+$ transition energy and a small $B(E2)$ being maintained. When looking at the higher spin region the effect of the 9^+ TBME creates the $I^\pi = 14^+$ isomer in ^{94}Pd with the analogous $I^\pi = 16^+$ spin trap isomer being created in ^{96}Cd [3].

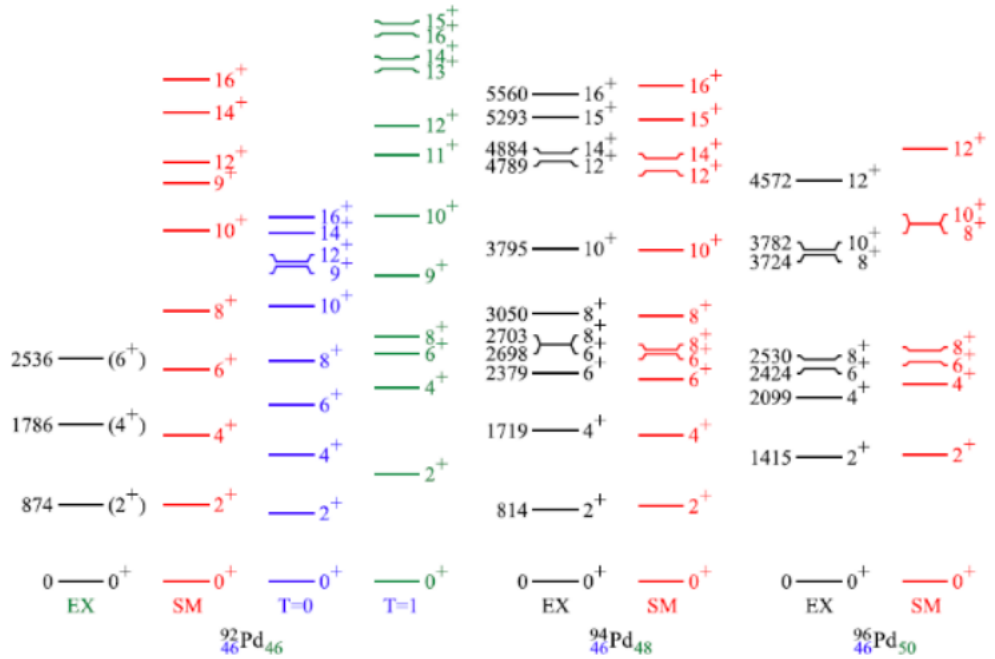


FIGURE 1.2: A side by side comparison between experimental results from [26, 40] and shell model calculations in the pg space from [34]. The figure shows the evolution of the proton-neutron interaction and even-parity yrast structure. Taken from reference [41].

Figure 1.3 shows the current known level scheme of ^{94}Pd [11, 13] compared with shell model calculations. The experimental information on these states were gathered from studies using the FRS in conjunction with the RISING gamma-ray spectrometer at GSI in which the decays of the isomeric 14^+ and 19^- states were observed and studied [11, 13–15] along with high spin beta decay research of ^{94}Ag . At current, only beta delayed or isomeric transitions have been observed with no prompt gamma-ray radiation from states of ^{94}Pd having been measured.

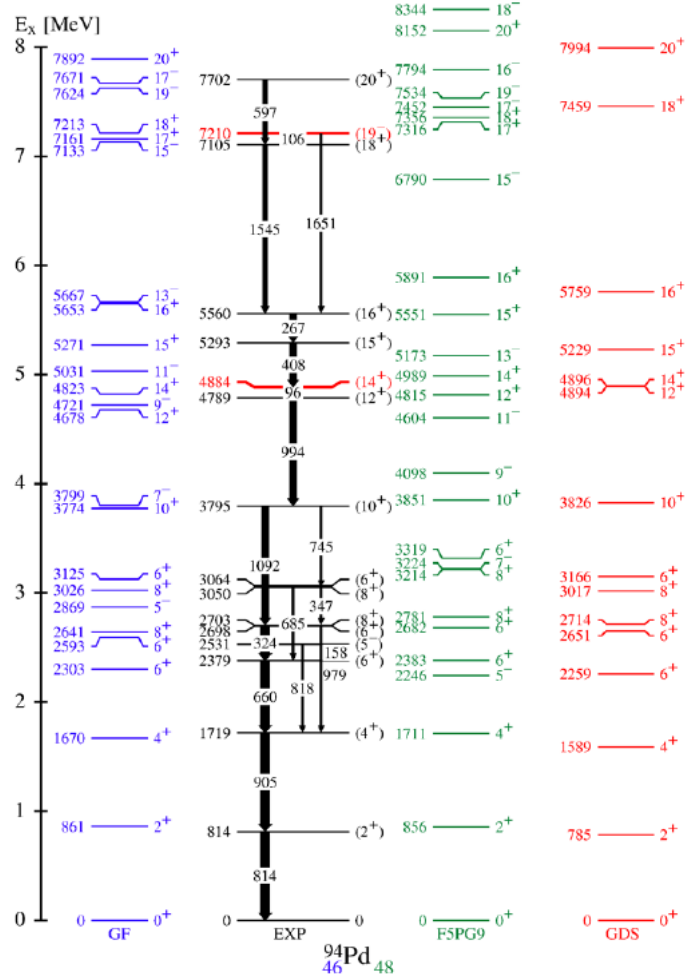


FIGURE 1.3: The experimental level scheme of excited states in ^{94}Pd [11, 14, 15, 42, 43] along with shell model calculations from varying model spaces [11, 34]. Previously reported $I^\pi = 19^-$ and 14^+ isomeric states are reported in red with reported half-lives of 197(22) ns and 499(13) ns respectively [11]. Taken from reference [41].

The goal of experiment S480, as the commissioning run of the DESPEC set-up, was to take high-precision measurements of the half-lives of the $I^\pi = 8^+$ and 6^+ states in the region of interest of $\text{B}(\text{E}2)$ evolution at ^{94}Pd . As well as this the experiment sought to prove the efficacy of the DESPEC set-up when conducting future decay spectroscopy experiments while simultaneously providing in-situ data for the validation of a NPTool/GEANT4 simulation. Shell model calculations predict these half-lives to be in the nanosecond to hundreds of picoseconds time scale making the FATIMA gamma-ray array the perfect tool for these measurements.

Specifically, the debate between the $I^\pi = 6^+$ and 8^+ states where the G9 and F5G9-basis models agree for the first GDS and F5G9 for the second will be solved in this work with the goal of developing the understanding of the evolution of the wave

function towards $N = Z$ and therefore the purity of the $g_{\frac{9}{2}}$ wave-function in this nucleus. This work will provide validation to calculations carried out using the Gross-Fenkel and Jun45 interaction models which operate in the $g_{\frac{9}{2}}p_{\frac{1}{2}}$ and the $f_{\frac{5}{2}}p_{\frac{3}{2}}p_{\frac{1}{2}}g_{\frac{9}{2}}$ respectively. The partial decay schemes of both ^{96}Pd and ^{94}Pd below their isomeric states of interest are shown in figure 1.4.

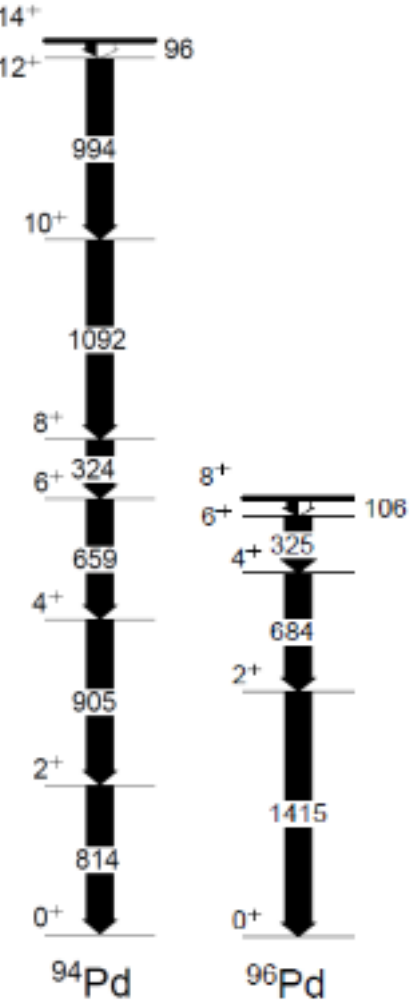


FIGURE 1.4: The partial decay schemes of ^{94}Pd (left) and ^{96}Pd (right) below their isomeric 14^+ and 8^+ states respectively [11, 16, 44].

A number of technical difficulties were prevalent when carrying out this work. The largest of these was the limited range of the FATIMA TDCs which were only able to measure coincidence data within a range of 450 ns after implantation. The next of these was the limited functionality of the AIDA array due to the high intensity of statistics which made the separation of implant and decay data difficult. Moreover, a problem arose between the timing clocks of the FATIMA TDC boards which limited the efficiency

of the array when measuring half-lives longer than 20 ns. Finally, with this being the first DESPEC experiment, initial tuning took more time than required and a number of subsystems crashed throughout the runtime. These crashes led to fewer statistics being gathered than initially desired but despite this, enough data was collected to allow for a rigorous analysis.

1.3 Thesis Outline

The subsequent chapters of this thesis are laid out as follows. Chapter 2 provides a brief overview of nuclear structure physics and in particular the role of electromagnetic decays in probing the nuclear structure of excited nuclear states. Chapter 3 presents a number of experimental conditions as well as an overview of the FATIMA set-up, geometry. Chapter 4 begins by listing the experimental details of S480 and goes on to describe the data reduction and PID selection carried out. The results of the GEANT4 simulation are presented here and compared with the experimentally extracted efficiencies using the singles to coincidence ratios for transitions in the ^{96}Pd isomeric decay. The measurements of the isomeric ratios are also included in this chapter. Chapter 5 presents the analysis of the nanosecond fast-timing measurements for $^{94,96}\text{Pd}$ and ^{94}Ru and compares the extracted results with the shell model calculations for these nuclei. The thesis concludes with a summary and suggestions for future work in Chapter 6.

Chapter 2

Nuclear Structure Theory

2.1 The Independent Particle Shell Model

2.1.1 The Nuclear Shell Model

The nuclear shell [45] model draws many parallels with the shell model of atomic physics where the structure of electrons is described as existing in a shell configuration of states. These electrons have discrete angular momentum and energy and obey the Pauli exclusion principle [46]. Shells of increasing energy are built up by sub-shells with a defined maximum occupancy or "degeneracy" determined by quantum numbers which describe each state. Filling electron shells in this way results in an inert core of filled shells with heightened stability and a number of valence electrons which end up governing the chemical properties of the atom.

One may solve the Schrödinger equation for these electrons to determine the energy levels of the shells which arise. The energy levels arise from the potential generated by the Coulomb force from the nucleus, however, this is one key difference between nucleons and atomic electrons. While electrons lie in an external potential field generated by the protons in the nucleus, the constituent protons and neutrons of the nucleus reside within their own generated potential and as a second difference they are constantly undergoing collisions with each other. These effects must be considered when creating models to explain the nature of nuclear structure.

The effects described by the atomic shell model can be seen experimentally, where the ionisation energy, the energy required to remove a bound electron from an atom, sees huge increases when an atomic shell is filled as seen in figure 2.1.

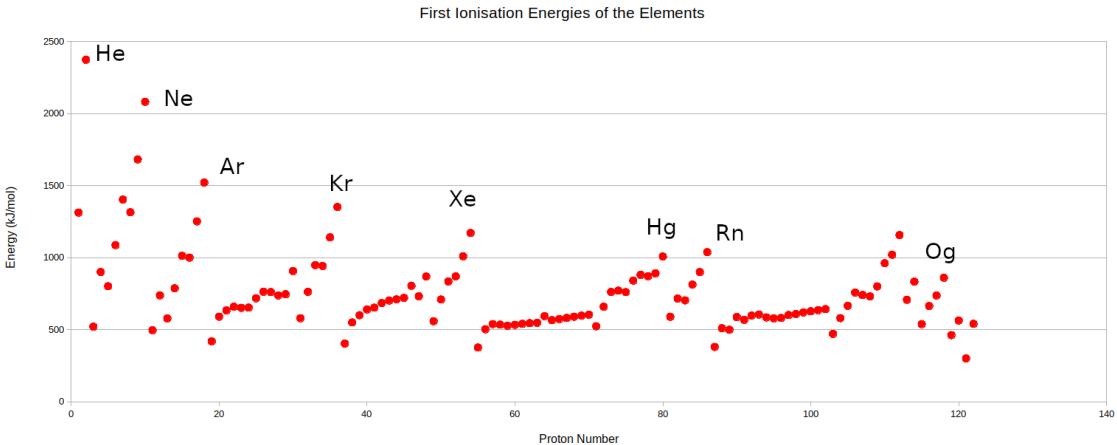


FIGURE 2.1: A plot showing the trend of first ionisation energies across the periodic table. Peaks in ionisation energies are seen in the noble gases (and mercury) as a result of filled p sub-shells, implying a heightened binding energy [47].

Strong evidence for this shell structure can be seen in the noble gases which have filled shells. This is reflected in their chemically inert behaviour along with their significantly higher first ionisation energies when compared with their neighbouring elements. Analogously, experimentally determined nucleon separation energies gradually rise with N and Z for particular isotones and isotopes but increases are consistently seen at particular neutron and proton numbers as shown in figure 2.2.

The phrase "magic numbers" was coined by Eugene Wigner when describing the work of Maria Goeppert-Mayer who proposed a shell-like structure of the nucleus with significantly increased stability for nuclei with 2, 8, 20, 28, 50, 82 or 126 protons, neutrons or an additional level of reinforced stability for those possessing a combination of the two. There exists further evidence which supports this model such as richer isotopic abundances for magic nuclei and many stable nuclei at the end of naturally occurring radioactive decay chains possessing a magic number. Additionally they often retain a higher first excited state energy than expected and have near zero electric quadrupole moments, the latter of which having implications on the shape of the nucleus, with both being observable in practice.

2.1.2 The Nuclear Potential

2.1.2.1 The Woods-Saxon Potential

The central component in any nuclear model is an accurate estimate of the nuclear potential which explains the macroscopic effects of the short range attraction experienced by the nucleons as a result of the strong nuclear force. The Woods-Saxon potential [48]

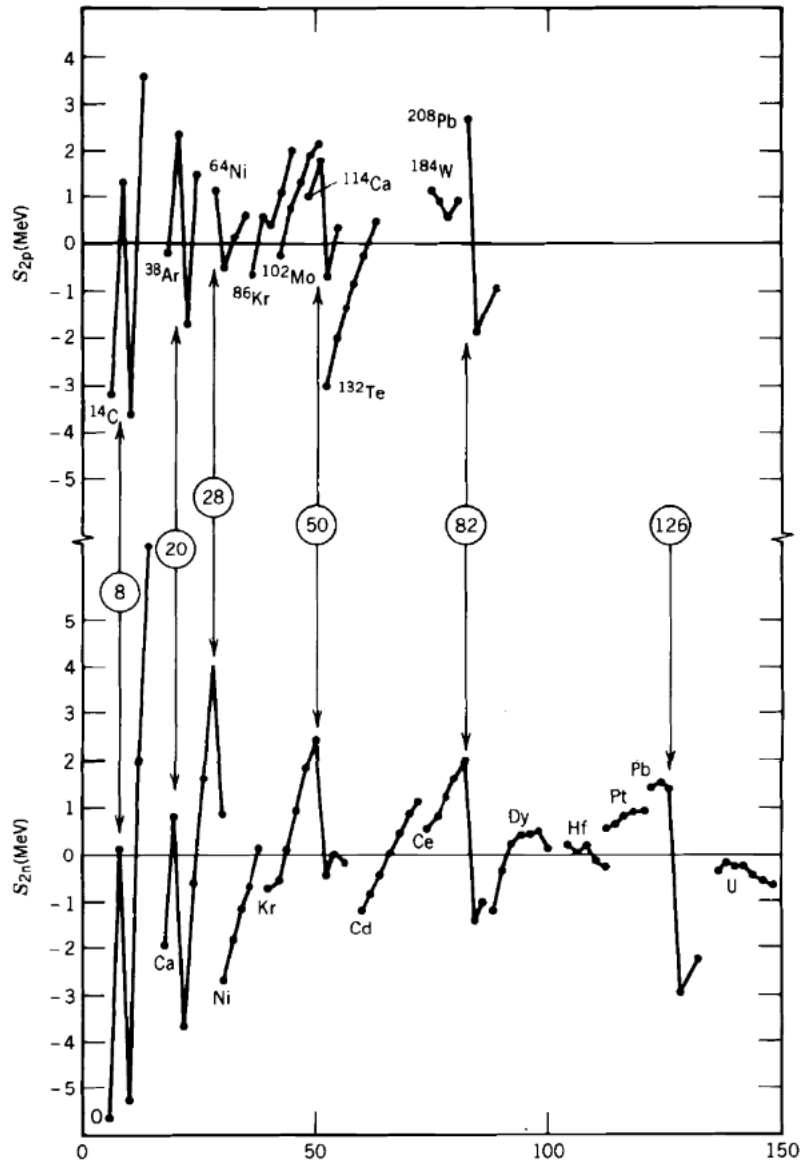


FIGURE 2.2: A plot displaying the 2 neutron and 2 proton separation energies for a number of nuclei across the nuclear chart. The neutron and proton magic numbers are circled and the "magic nuclei" are shown to have heightened separation energies reflecting an increased stability [49].

was developed as an intermediary between the infinite well and harmonic oscillator potentials to define the average potential of the nucleus and is described by equation 2.1.

$$V(r) = \frac{-V_o}{1 + e^{\frac{r-R}{a}}} \quad (2.1)$$

Where V_o is the potential depth at ~ 50 MeV, a represents the surface thickness

of the nucleus at ~ 0.5 fm and R is the mean nuclear radius which can be estimated by equation 2.2.

$$R = r_o A^{\frac{1}{3}} \quad (2.2)$$

Where r_o is a constant equal to 1.25 fm and A is the mass number. Here, the infinite potential well component is able to predict the first three magic numbers of 2, 8 and 20 while the harmonic oscillator component describes the smooth edge to the potential which sensibly mirrors the distribution of charge and mass. These are good indicators of an accurate nuclear potential when filling the shells with the $2(2l+1)$ degeneracy where the $(2l+1)$ term is present due to the m_l quantum number and the factor of 2 comes from the spin degeneracy of the fermionic nucleons with $m_s = \pm\frac{1}{2}$. It is important to note that protons and neutrons are distinguishable particles and therefore do not have to obey the Pauli exclusion principle with each other. Resultantly they occupy the same states in separate configurations. Nonetheless, there is clearly something missing from this description of the nuclear potential which is unable to reproduce the larger magic numbers which can be observed experimentally.

2.1.2.2 The Spin-Orbit Potential

The Woods-Saxon potential lacks a term to describe the spin-orbit phenomenon but thankfully atomic physics can once again provide some insight into this interaction. The atomic shell model describes an electromagnetic spin-orbit interaction between the intrinsic magnetic dipole of the electrons and the generated electric field from their orbit. This type of force also appears to be present in the interaction between nucleons, with the $l.s$ term altering the ordering of states and introducing sub-states which differ in energy. This makes the m_l and m_s quantum numbers obsolete and a new quantum number, j , is introduced. This is known as the total angular momentum and is a linear combination of the orbital and spin angular momenta i.e. $j = l \pm s$ depending on whether the spins align (+) or not (-). However, unlike in atomic physics an alignment of the nuclear spins actually leads to a lower energy state due to both potentials being negative. The energy splitting caused by these states is directly proportional to l as seen in equation 2.3.

$$\Delta E \propto \frac{1}{2\hbar}(2l + 1) \quad (2.3)$$

This new arrangement of levels requires a notation, for example, $2d_{\frac{5}{2}}$ refers to a state in the second n shell, with an orbital angular momentum of 2 (where $l = 0, 1, 2, 3$

... corresponds to s, p, d, f ... etc) with a total angular momentum of $j = \frac{5}{2}$. The total angular momentum of the state can be used to determine the degeneracy of the state which is given by $(2j+1)$, this is equal to the range of values that can be occupied by the m_j quantum number which takes values between $-j$ and j in unitary increments. An example of shell model states being filled can be seen below in figure 2.3 with protons and neutrons being filled independently.

The shell model is successful in reproducing the energetics of nuclei close to the magic proton and neutron numbers, however its major limitation is that it assumes that the structure and properties of the nucleus are determined by the highest energy unpaired valence nucleon. Indeed, this is viable when predicting the ground state spins and parities of nuclei with the only required knowledge being the number of protons and neutrons in the nucleus. This means the shell model predicts that nuclei with an even number of protons and neutrons (even-even nuclei) all have a 0^+ ground state, which they do. This is due to the way sub-shells are filled, which is generally in pairs of opposing m_j values. These predictions are also accurate for nuclei with an odd number of protons or neutrons. Another notable prediction for even-even shell model nuclei is the presence of a first excited 2^+ state at roughly half the energy required to break a pair of nucleons apart. Moving forward with this, we realise that this property is not limited to shell model nuclei, but all even-even nuclei meaning a more complex nuclear model is required. More recent shell model calculations using Monte Carlo methods can be more effective but models which focus on collective excitations are required. It is often the case in these models that unrealistic effective charges are invoked, such as the proton no longer carrying a positive charge and the neutron not being neutral.

2.1.3 Configuration Mixing

If two states share the same spin and parity it is possible for the configurations of these states to mix. For two initial unperturbed energy levels E_1 and E_2 described by the wave functions ϕ_1 and ϕ_2 respectively, an interaction between them, V , will result in a mixing matrix element of $\langle \phi_1 | V | \phi_2 \rangle$. The degree to which the mixing occurs depends on the energy separation of the two states $\Delta E_u = (E_2 - E_1)$ along with the magnitude of the mixing matrix element with small mixing matrix elements still contributing to large changes to the energies of states for small values of ΔE_u . The relationship, R , between the states is defined in equation 2.4 [50].

$$R = \frac{\Delta E_u}{V} \quad (2.4)$$

Where V represents the mixing matrix element. The perturbed energy of the two states $E_{1'}$ and $E_{2'}$ can be represented as described in equations 2.5 and 2.6.

$$E_{1'} = \frac{1}{2}(E_1 + E_2) - \frac{\Delta E_u}{2} \sqrt{1 + \frac{4}{R^2}} \quad (2.5)$$

$$E_{2'} = \frac{1}{2}(E_1 + E_2) + \frac{\Delta E_u}{2} \sqrt{1 + \frac{4}{R^2}} \quad (2.6)$$

The perturbed wave functions of the two states are defined in equations 2.7 and 2.8.

$$\epsilon_1 = \alpha\phi_1 + \beta\phi_2 \quad (2.7)$$

$$\epsilon_2 = \alpha\phi_2 - \beta\phi_1 \quad (2.8)$$

β is defined in equation 2.9 and $\alpha^2 + \beta^2 = 1$.

$$\beta = \frac{1}{[1 + [\frac{R}{2} + \sqrt{1 + \frac{R^2}{4}}]^2]} \quad (2.9)$$

Two mixed states may approach each other which presents itself as a function of some type of structural effect, namely deformation. The two states will never truly meet but instead repel each other with a minimum range equal to twice the mixing matrix element - this is known as the inflection point. The wave functions following this point will be dominated by the unperturbed wave function of the other state. These states are said to be 'non-crossing' because the states which do not mix maintain their trajectories and cross at the inflection point.

Multi-state mixing can be thought of as a series of two state mixings. For N degenerate states which are all able to mix with equal matrix elements the net result will be a lowering of one state by $(N - 1)V$ and a raising of the other state by V with the wave function of the lowered state being described in equation 2.10 for a completely mixed state.

$$\epsilon = \sum_{i=1}^N \frac{1}{\sqrt{N}} \phi_i \quad (2.10)$$

2.1.4 Nuclear Isomerism

Excited gamma-decaying nuclear states are often defined as having half-lives of $>10^{-9}$ s but in some cases half-lives up to hours or even days are seen in some states. These states are known as isomeric states or isomers are also sometimes labelled as metastable. Isomeric states come in four different forms: spin trap, K, shape and seniority isomers, the latter of which is relevant to the nuclei studied in this work [51, 52].

2.1.4.1 Seniority

Seniority, ν is a quantum number which describes the number of unpaired nucleons which form an excited state in a nucleus [18–20, 50]. For example, if two protons in the $g_{\frac{9}{2}}$ shell were coupled and formed an 8^+ state the seniority of that state would be $\nu = 2$ because the remaining protons would be coupled to $J^\pi = 2^+$. Following this logic the ground state of an even-even nucleus will always have a seniority of zero because in this case all of the nucleons are paired. Seniority is only present in the excited states of a nucleus with the maximum angular momentum that can be created being defined by equation 2.11.

$$J^{max} = nj - \frac{n(n-1)}{2} \quad (2.11)$$

Where n is the number of nucleons in the shell. The highest angular momentum state created this way will usually be a longer-lived isomeric state. This long half-life is brought about by a low transition rate as well as a small transition energy which also brings a competing process in internal conversion meaning these transitions often have large internal conversion coefficients.

2.1.5 Nuclear Decay

The optimal way to study the properties of the nucleus is by observing the decay of nuclei into other isotopes along with the de-excitations that follow this process. There are a number of different ways in which nuclei can decay which depends on the stability of the nucleus in question.

2.1.5.1 Beta Decay

Beta decay is a process which many nuclei undergo in an attempt to approach stability. Beta decays are sanctioned by the weak nuclear force following the exchange

of a W boson which allows quarks to change type. Proton-rich nuclei will undergo β^+ decay, where a proton in the nucleus decays into a neutron, releasing a positron and an electron neutrino. On the other hand, if the nucleus has a largely disproportionate amount of neutrons it will undergo a β^- decay where a neutron decays to a proton with the nucleus releasing an electron and an electron anti-neutrino. Equations 2.12 and 2.13 describe these contrasting forms of decay.



Electron capture is a competing process to β^+ decay. An atomic electron can be absorbed by the nucleus which in turn allows a proton to convert into a neutron, releasing an electron neutrino. This reaction is detailed in the equation 2.14.



These interaction happens due to a particular nuclei not having the nuclear binding energy required to keep its constituent nucleons in a fully bound state. Positive Q values, such as in beta decays, represent a release of nuclear binding energy and can be calculated by equations 2.15, 2.16 and 2.17 for the various forms of decay.

$$\beta^- \text{decay} : Q = [m(Z, A) - Zm_e]c^2 - [(m(Z + 1, A) - (Z + 1)m_e + m_e)]c^2 \quad (2.15)$$

$$\beta^+ \text{decay} : Q = [m(Z, A) - Zm_e]c^2 - [(m(Z - 1, A) - (Z - 1)m_e + m_e)]c^2 \quad (2.16)$$

$$e^- \text{capture} : Q = [m(Z, A) - Zm_e]c^2 - [m(Z - 1, A) - (Z - 1)m_e]c^2 \quad (2.17)$$

The Q value of a beta decay is equal to the highest energy nuclear state which can be populated following a beta decay and consequently the highest energy coincident gamma ray which can be emitted. Beta decays can be classified depending on the change in angular momentum and parity between the initial and final nuclear states of the mother and daughter nuclei. The selection rules of beta decay are defined in table 2.1.

Changes in angular momentum between the initial and final states of the mother and daughter nuclei must be accounted for by the angular momentum of the emitted beta particle and neutrino. Fermi transitions correspond to those in which the spins of

Transition	L	ΔL	$\Delta \pi$
Super-allowed	0	0	0
Allowed	0	0,1	0
1 st Forbidden	1	0,1,2	1
2 nd Forbidden	2	2,3	0
3 rd Forbidden	3	3,4	1
4 th Forbidden	4	4,5	0

TABLE 2.1: A summary of the angular momentum and parity selection rules of β decay from reference [49].

the neutrino and beta particle lie anti-parallel, giving a spin of $S = 0$, resulting in an unchanged nuclear spin. Meanwhile, Gamow-Teller transitions have a spin of 1 resulting from the aligned spins of the neutrino and beta particle. Forbidden decays are not impossible as their name suggests but instead reflect their notably lower probability of occurring which falls with larger values of ΔL and the violation of parity conservation. The comparative half-life or ft value provides an excellent point of comparison for beta decay probabilities in different nuclei. This value can be calculated by equation 2.18.

$$ft_{\frac{1}{2}} = \ln 2 \frac{2\pi^3 \hbar^7}{g^2 M_e^5 c^4 |M_{fi}|^2} \quad (2.18)$$

Here, g is a constant which describes the strength of the interaction, M_{fi} is the nuclear matrix element, $t_{\frac{1}{2}}$ is the half-life of the decay and f is the Fermi integral which depends on the proton number of the daughter nucleus and the maximum electron energy. The log of this value is often a preferred form of the value and provides a measure of the forbiddenness of the decay.

By observing the beta decay selection rules it is possible to make predictions on the populated states of the daughter nuclei using literature knowledge. For example, the $(2, 3^+)$ assignment of the ground state of ^{110}Tc . The large Q value and the beta decays likely being mainly allowed or super-allowed in nature would result in a number of high energy states between spin 1 and 4 being populated in ^{110}Ru . However, along with this one must consider the nucleon separation energies for high Q value beta decays, which in the case of ^{110}Ru sits at 8796 keV for neutrons and 10621 keV for protons. This means an amount of beta delayed neutron emission is possible, resulting in states being populated in ^{109}Ru as well. This method is also useful in the determination of spin parities of unknown states, provided there are sufficient statistics and knowledge of at least the ground state spins and parities.

2.1.5.2 Internal Conversion

An excited nucleus may go through a process known as internal conversion [53]; a competing mode of de-excitation to gamma decay. In this process the nuclear electromagnetic field interacts with a K-shell electron which is then ejected from the atom. The excess energy in the system is then converted into the kinetic energy of the electron, T_e defined in equation 2.19.

$$T_e = \Delta E - BE \quad (2.19)$$

Where BE is the binding energy of the electron and ΔE is the energy difference between the initial and final nuclear states. A cascade of higher energy electrons will then de-excite to fill the holes left in the atomic shells. This results in a burst of characteristic X-rays being emitted which may interact with less tightly bound electrons, emitting Auger electrons. K-shell electrons have the closest proximity to the nucleus and are therefore most commonly ejected but electrons occupying the s state in the L, M and N atomic shells may also interact with the nucleus producing the same effect. These electrons are ejected if the nuclear field can not provide the binding energy required to convert the K shell electron.

The internal conversion coefficient (α) is a ratio between the rates of internal conversion and gamma decay for a particular transition [53]. This is outlined in equation 2.20.

$$\alpha = \frac{\Gamma_{IC}}{\Gamma_\gamma} \quad (2.20)$$

Internal conversion is responsible for all E0 transitions (i.e. $0^+ \rightarrow 0^+$) as the conservation of angular momentum forbids this transitions from gamma decay.

2.2 Electromagnetic Transitions Between Excited Nuclear States

The previously established beta decay selection rules often result in the decay leaving the daughter nucleus in an excited state. These states are exceedingly unstable and this is reflected in their half-lives which are often in the picosecond ($\sim 10^{-12}$ s) to nanosecond ($\sim 10^{-9}$ s) range [52, 54–56]. A nucleus can decay from its excited states to its ground state through a cascade of gamma-ray emissions which strip the

nucleus of its angular momentum. Gamma rays are a form of ionising electromagnetic radiation with wavelengths generally ranging between 10^4 fm - 10^2 fm, corresponding to energies of 0.1 to 10 MeV. The energy carried by the gamma ray will not be equal to the exact difference between the energies of the initial and final nuclear states. This small difference comes from a kick received by the nucleus which is required to fulfil the conservation of momentum.

2.2.1 Characteristics of EM Transitions

As with beta decays, gamma transitions follow selection rules based on the parities and angular momenta of the initial and final states. The conservation of angular momentum in gamma decay described in 2.21 [52, 54–56] and must be upheld.

$$I_i = L + I_f \quad (2.21)$$

Where I_i and I_f are the initial and final nuclear spins respectively, and L is the angular momentum carried by the gamma ray, also known as the order. This relationship means L can hold any value in a range of integers described by $|I_i - I_f| < L < |I_i + I_f|$. As a result, many different orders of gamma decay can occur between states, meaning transitions between states often have a mixed multi-polarity. An L of 1 corresponds to a dipole transition, while $L = 2, 3$ and 4 are called quadrupole, octupole and hexadecapole transitions respectively.

The second characteristic concerns the conservation of parity, which relegates the decays to being magnetic or electric in nature. Change in parities are permitted for odd electric and even magnetic transitions, i.e. E1, M2, E3 and M4 transitions are all able to pass between states with opposite parities. Conversely, even electric and odd magnetic transitions will not occur between states of different parity, meaning parity must be conserved between states in M1, E2, M3 and E4 transitions. The properties of these different types of transitions are summarised in table 2.2.

2.2.2 EM Transition Rates in Nuclei

The electromagnetic transition rates of decays depend on the multipolarity of the decay mode and can be calculated using equation 2.22 [49].

$$T(\sigma L) = \frac{2(L+1)}{\epsilon_o \hbar L [(2L+1)!!]^2} \left(\frac{\omega}{c} \right)^{2L+1} B(\sigma L) \quad (2.22)$$

Notation	l	π_γ	Radiation Type
E1	1	-1	Electric Dipole
M1	1	+1	Magnetic Dipole
E2	2	+1	Electric Quadrupole
M2	2	-1	Magnetic Quadrupole
E3	3	-1	Electric Octupole
M3	3	+1	Magnetic Octupole

TABLE 2.2: A summary of the properties of different orders of electromagnetic transitions.

Where $B(\sigma L)$ is the reduced transition probability which is dependant on the overlap of the initial and final wave-functions of the initial and final states. Most transitions between states are mixed in multi-polarity, however, in reality these mixing ratios are incredibly small as gamma-ray transitions favour low spin parity changes making the lower L transitions (E1, M1, E2, M2) many more orders of magnitude likely to occur than those of a higher order.

2.2.3 Weisskopf Single-Particle Estimates

The Weisskopf estimates take a single particle approach whereby the case of a single proton excitation is considered and can be used to calculate the reduced transition probabilities for electric (EL) equation 2.23 and magnetic (ML) 2.24 transitions [57].

$$B(EL) = \frac{e^2}{4\pi} \left(\frac{3R^L}{L+4} \right) \quad (2.23)$$

$$B(ML) = 10 \left(\frac{\hbar}{cRm_p} \right)^2 \frac{e^2}{4\pi} \left(\frac{3R^L}{L+4} \right) \quad (2.24)$$

The Weisskopf estimates for electric and magnetic transitions up to order 5 are listed in 2.3 where one can clearly see the a strong preference for transitions with a small change in spin and a slight lean towards electric transitions.

To summarise, mixed transitions are far more significant when multiple lower order transitions are sanctioned between initial and final states. For instance, it is not uncommon to see a strongly mixed E2/M1 transition between states such as $2_2^+ \rightarrow 2_1^+$. If one wishes to measure the mixing ratio of such a transition, one may construct an angular correlation between the transition of interest and another transition in the same cascade. Mixing ratios each posses a characteristic angular correlation depending on the initial and final magnetic sub-states. By measuring this correlation and fitting it to

Multi-polarity	Electric Transition Rates (s^{-1})	Magnetic Transition Rates (s^{-1})
1	$1.0 \times 10^{14} A^{\frac{2}{3}} E^3$	$3.1 \times 10^{13} E^3$
2	$7.3 \times 10^7 A^{\frac{4}{3}} E^5$	$2.2 \times 10^7 A^{\frac{2}{3}} E^5$
3	$3.4 \times 10^1 A^2 E^7$	$1.0 \times 10^1 A^{\frac{4}{3}} E^7$
4	$1.1 \times 10^{-5} A^{\frac{8}{3}} E^9$	$3.3 \times 10^{-6} A^2 E^9$
5	$2.4 \times 10^{-12} A^{\frac{10}{3}} E^{11}$	$7.4 \times 10^{-13} A^{\frac{8}{3}} E^{11}$

TABLE 2.3: A table listing the Weisskopf estimates for electric and magnetic single particle transition rates. A is the atomic mass of the nucleus and E is the energy in MeV.

a Legendre polynomial of the form shown in equation 2.25, one is able to extract the relevant coefficients which can be compared to nuclear data to determine the mixing ratio.

$$W(\theta) = A_o(1 + A_2 P_2 \cos(\theta) + A_4 P_4 \cos(\theta)) \quad (2.25)$$

In this work the electric transition probabilities for E2 transitions are the measurements of interest and were calculated using equation 2.26.

$$B(E2 : I+2 \rightarrow I) = \frac{0.0566}{E_\gamma^5 (1+\alpha) T_{\frac{1}{2}}} \quad (2.26)$$

Where E_γ is the energy of the associated transition, α is the internal conversion coefficient and $T_{\frac{1}{2}}$ is the half-life of the nuclear state. These equations allow one to compare the predictions made by various nuclear physics models with accurate experimentally gathered data via measurements of the half-lives of nuclear states.

2.3 Enhanced Shell Model Calculations

For the realms of the nuclear chart which begin to veer away from the magic numbers of protons and neutrons, the shell model becomes incapable of accurately predicting nuclear structure. In these zones more complex nuclear models are required. Models often begin by simulating filled sub-shells whose energetics can be accurately predicted using the shell model. This approach allows theorists to make changes to the interactions experienced by the nucleons which populate the outer most sub-shells of the nucleus, called the model space, which govern the energetics of the nucleus when excited.

Summaries of the evolutions of shell model calculations can be found in general reviews written by Brown [58] and Coraggio [59] with reviews focussed on the ^{100}Sn

region of the nuclear chart having been published by Faesetermann [1] and most recently Gorska in 2022 [24]. In the context of this work enhanced shell model calculations were carried out to determine the effect of seniority on the nuclear half-life of the gamma decaying 8^+ state in ^{94}Pd . Two sets of calculations were carried out using the Gross-Fenkel and JUN45 interactions. The gf calculations were focussed in the proton $g_{\frac{9}{2}}p_{\frac{1}{2}}$ model space while the JUN45 interaction was simulated in the proton $f_{\frac{5}{2}}p_{\frac{3}{2}}p_{\frac{1}{2}}g_{\frac{9}{2}}$ space with the gf calculations implementing and reproducing energy levels consequent of a seniority scheme and JUN45 describing more collective excitations. It was the goal of experiment S480 to determine which of these models, and therefore interactions, accurately define the half-life of the 8^+ state in ^{94}Pd .

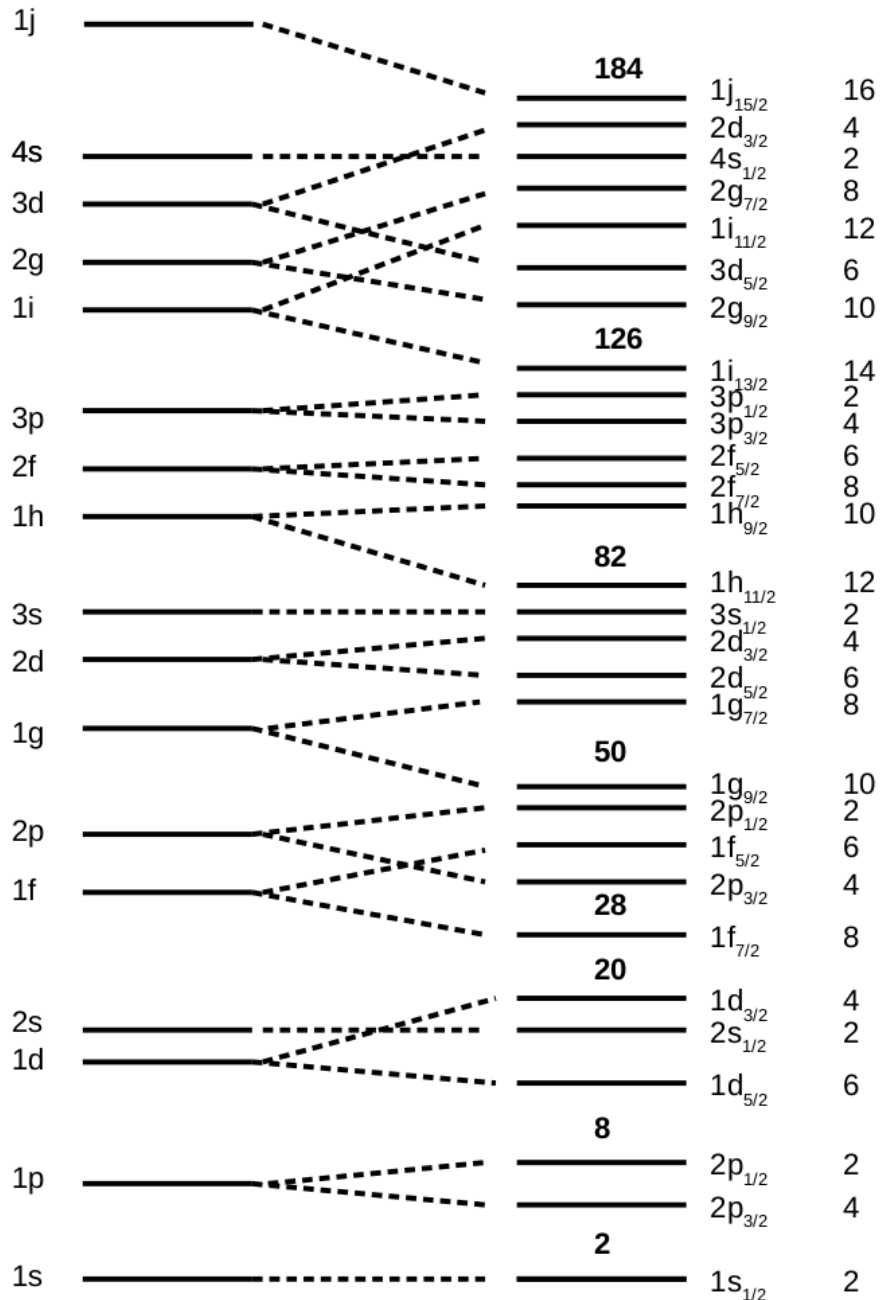


FIGURE 2.3: The independent particle shell model configuration in which nucleons are arranged. The effects of 1.s coupling are represented on the right of the diagram in the form of sub-shells which combine to form filled shells, giving rise to the magic numbers indicated in bold. The degeneracy of each subshell is shown to its right and is equal to $2j+1$. Adapted from [49].

Chapter 3

Experimental Considerations

3.1 Gamma-Ray Interaction Cross-sections

3.1.1 Operation of Semiconductor Detectors

High Purity Germanium (HPGe) detectors are the current preferred form of semiconductor detector for high precision gamma-ray spectroscopy studies. They provide radiation detection capabilities for gamma rays in the range of 0 MeV to 20 MeV with efficiencies of 1 % along with excellent resolutions of 0.5% at 1 MeV with efficiency and resolution decreasing with energy. The rate of this decrease depends on the dimensions of the detector. Their largest limitation is their constant requirement to be cooled to temperatures of 85 K - 100 K to ensure their operation with changes in temperature negatively affecting their response. Low temperature conditions separate the electrons from the lattice-structured germanium atoms into a valence band and a conduction band. In an idealised case of 0 K temperatures and 100 % Germanium purity all of these electrons will reside in a fully occupied valence band where, if provided with enough thermal excitation energy, they will cross the band gap into the conduction band. This leaves a hole in the valence band which, along with the electron, act as the charge carriers of the system. In practice, there are often impurities in the crystal which create an uneven split of electrons in the valence and conduction bands. Germanium is a group IV element with each constituent atom forming four covalent bonds in its lattice structure. The presence of impurities often comes in the form of group III or group V elements existing in place of some germanium atoms in the lattice. In the case of group III elemental impurities only three covalent bonds would be formed leaving an electron hole. This is known as an acceptor (p-type) impurity while the opposite, a donor impurity (n-type) is defined by the presence of a group V element which results in an extra covalent bond being formed. Depending on the type of impurity in the semiconductor crystal either the hole (p-type)

or the electron (n-type) acts as the charge carrier. In HPGe detectors these impurities often exist on the scale of $\leq 2 \times 10^{-4}$ particles per billion [60]. In general, doping is used to create a certain value of charge carrier which is not temperature sensitive. This allows the operator slightly more control in the electrical properties of the device such as the conductivity.

The structure of the semiconductor lends itself well to the detection of radiation. The interaction of photons via the photoelectric effect, compton scattering or pair production excites the electrons across the band gap, into the conduction band with the number of electron-hole pairs being proportional to the energy of the radiation. The energy of the band gap is generally on the scale of ~ 1 eV meaning there is only a small statistical fluctuation in the number of charge carriers per pulse which results in a good signal to noise ratio and energy resolution. If an electric field is then applied to the crystal the relevant charge carriers will travel through the crystal allowing for signal processing and the high precision energy measurement to be taken.

3.1.2 Operation of Scintillation Detectors for Gamma-ray Spectroscopy

Scintillation detectors are often used in gamma-ray spectroscopy for their reasonably good energy resolution and extremely fast timing resolution of up to 320 ps. Scintillator materials are defined by their fluorescent response to interactions with radiation. This fluorescence is caused by the excitation of an electron due to the photoelectric effect or compton scattering from an incident photon. The excited molecule then de-excites and emits a photon which is used to produce electrons at the photocathode that are then in turn are multiplied through the use of a photomultiplier tube. These electrons then travel to the anode with the application of a potential voltage of ~ 500 V with the amount of charge collected being proportional to the energy of the initial incident photon. The photon dependent operation of a scintillation detector is what allows for their fast timing response when gathering data making them the state of the art tool when determining timing information between two gamma rays. The internal design of a typical scintillation detector can be seen in figure 3.1. Cerium doped Lanthanum Bromide detectors ($\text{LaBr}_3(\text{Ce})$) are the current state-of-the-art scintillators for fast timing measurements when compared to other scintillators with a better energy resolution of 3% at 1 MeV and faster timing capabilities than its counterparts [61, 62] with differences in the timing and energy resolutions depending on the geometry of the crystal [63]. However, one downside of using $\text{LaBr}_3(\text{Ce})$ detectors is the internal activity of ^{138}La which decays via electron capture and may cause contaminants in data sets depending on the energy region of interest [64]. The combination of a good energy resolution and fast

timing response make $\text{LaBr}_3(\text{Ce})$ detectors an obvious choice for fast timing measurements along with gamma-ray spectroscopy resulting in the commissioning of arrays such as FATIMA [8] and the LaBr_3 array at NSCL/FRIB [65].

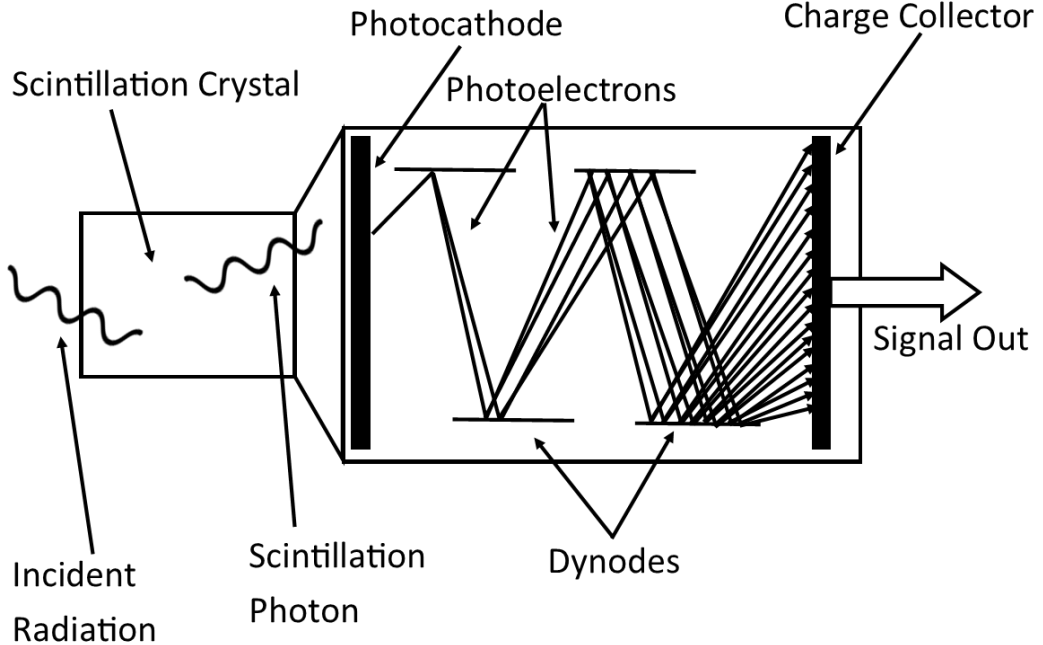


FIGURE 3.1: A schematic describing the operation of a scintillation detector. The absorption of a gamma ray leads to the de-excitation of an electron from the crystal, releasing a photon which in turn interacts with the photo-cathode. Here, an electron is released which is multiplied through the use of a photomultiplier tube. The number of electrons is proportional to the energy of the original incident gamma ray.

3.2 Nuclear Reaction Mechanisms

If one wishes to determine fundamental properties of a nucleus they must first be able to access it for the purpose of studying its nuclear decays. Radioactive nuclei to be studied generally fall into one of two categories; they can either be naturally occurring or have to be produced in nuclear reactions with the latter forming the majority of cases. Projectile fragmentation, induced fission and deep inelastic collisions are favourably utilised to produce many exotic and non-naturally occurring radionuclides while more controlled reactions in the form of coulomb excitation and nucleon transfer reactions can also be used. Induced fission reactions involve the reaction of a neutron with a fissile material such as ^{235}U or ^{239}Pu . These nuclei will become unstable due to their abundance of neutrons and undergo fission whereby they reform into a mixture of lighter, more stable nuclei. Deep inelastic collisions can be used to probe the hadrons within a nucleus through the use of an interacting electron while nucleon transfer reactions

can be used to simulate stellar reactions in laboratory settings through the addition of one group of nucleons to another, usually followed by a decay of some form. Moreover, coulomb excitation experiments involve no physical collisions but use a beam of ions to interact with the target nucleus through only the electromagnetic interaction by narrowly missing the target. Through this reaction a nuclei may become excited through a series of E2 excitations into low lying even angular momentum states. The work in this thesis was carried out through the use of a projectile fragmentation reaction which will be described in detail in section 3.2.2.

3.2.1 LISE++ Simulations

The LISE++ simulation package [66] is a tool that can be used to emulate the transfer of projectile fragmentation products through a magnetic separator such as the FRS. The software calculates ion-optics, nuclear cross-sections, energy losses in materials, separator acceptances as well as charge-state distributions. Simulations are conducted in a Monte Carlo style and direct comparisons with the data can be made once these are carried out.

3.2.2 Projectile Fragmentation Reaction.

Projectile fragmentation [67] is a nuclear reaction mechanism which can be used to produce heavy, exotic, neutron rich nuclei. These reactions take place under relativistic conditions with beam energies ranging from tens of MeV/nucleon to hundreds of MeV/nucleon. As a result of these high energies the beam and target nuclei will only be in contact for a time on the order of $\sim 10^{-23}$ s which is marginally smaller than the orbital period of a single nucleon in a nucleus meaning the target nucleons are stationary in the reference frame of the beam particles. Therefore it can be assumed that the first part of this reaction, known as abrasion, has no collective component and only depends on the interactions between nucleons. The "participant" nucleons involved in the reaction depends on the physical overlap of one nuclei with the other, with non interacting nuclei being known as "spectators". These two groups of particles are known as the pre-fragments and the participant nucleons are removed as a "pre-equilibrium emission". The remaining pre-fragments then attempt to re-arrange themselves through nucleon (primarily neutron) evaporation reaction channels which precede gamma-ray de-excitations. This process, known as ablation, results in many reaction channels which produce a cocktail of ion fragments at energies of tens of MeV/nucleon that can then be separated by use of a recoil separator to access the nuclei of interest. The ions which are produced in this cocktail often end up populating high spin states which preferentially

decay via high energy gamma ray emissions between 1 MeV - 10 MeV into yrast states [68–71]. The projectile fragmentation process is summarized in figure 3.2.

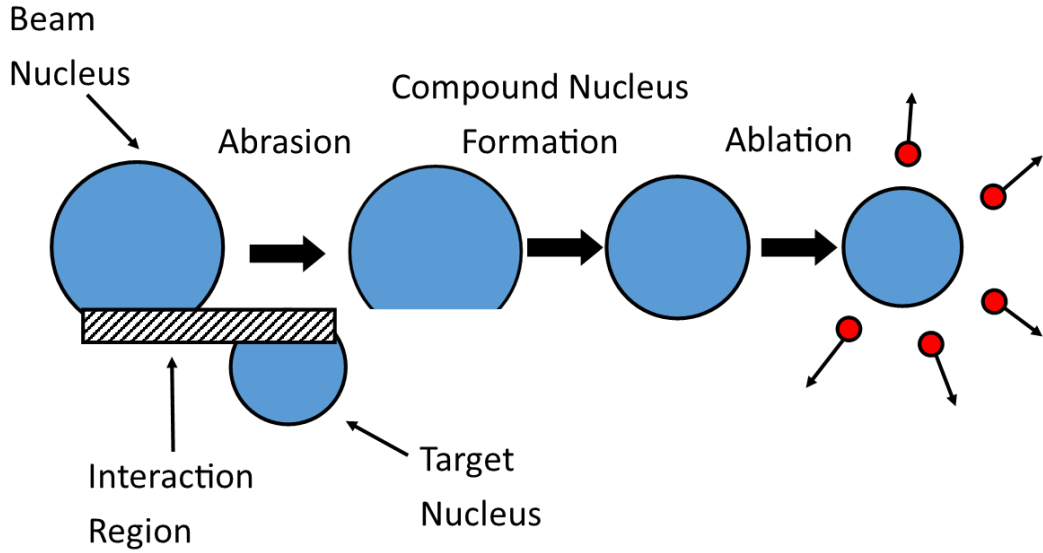


FIGURE 3.2: The projectile fragmentation process used at various particle accelerator facilities to create nuclear species of interest.

The ABRABLA code is a Monte-Carlo simulation package which is used at GSI to calculate the cross-sections and momentum of the products following heavy ions at relativistic speeds using the abrasion-ablation model. It is made up of ABRA - the improved version of the abrasion model for relativistic heavy ion collisions [72, 73] and ABLA - an efficient code for calculating the de-excitation routes of excited nuclei through particle evaporation and fission pathways [74]. The code is primarily used to determine the desired input parameters for projectile fragmentation reactions such as the beam energy.

3.3 Interaction of Gamma rays with Matter

When concerning the interaction of gamma rays with matter there are three ways which they may do so. These are compton scattering, the photoelectric effect and pair production. A comparison of the cross-sections of these interactions in pure germanium is shown in figure 3.3. When interacting with matter at low energies the dominant effect is the photoelectric effect at energies of less than 100 keV. Compton scattering is then effective at the MeV range with pair production beginning to occur at energies above 1.022 MeV. The final interaction listed in figure 3.3 is coherent or "Rayleigh" scattering which is an elastic interaction that happens when the energy of the incident photon is very small, causing it to scatter after colliding with an orbital electron which it does not

have the energy to liberate. This process is not considered to be a major interaction as it never dominates the cross-section. This section will describe the major interactions and their mechanisms.

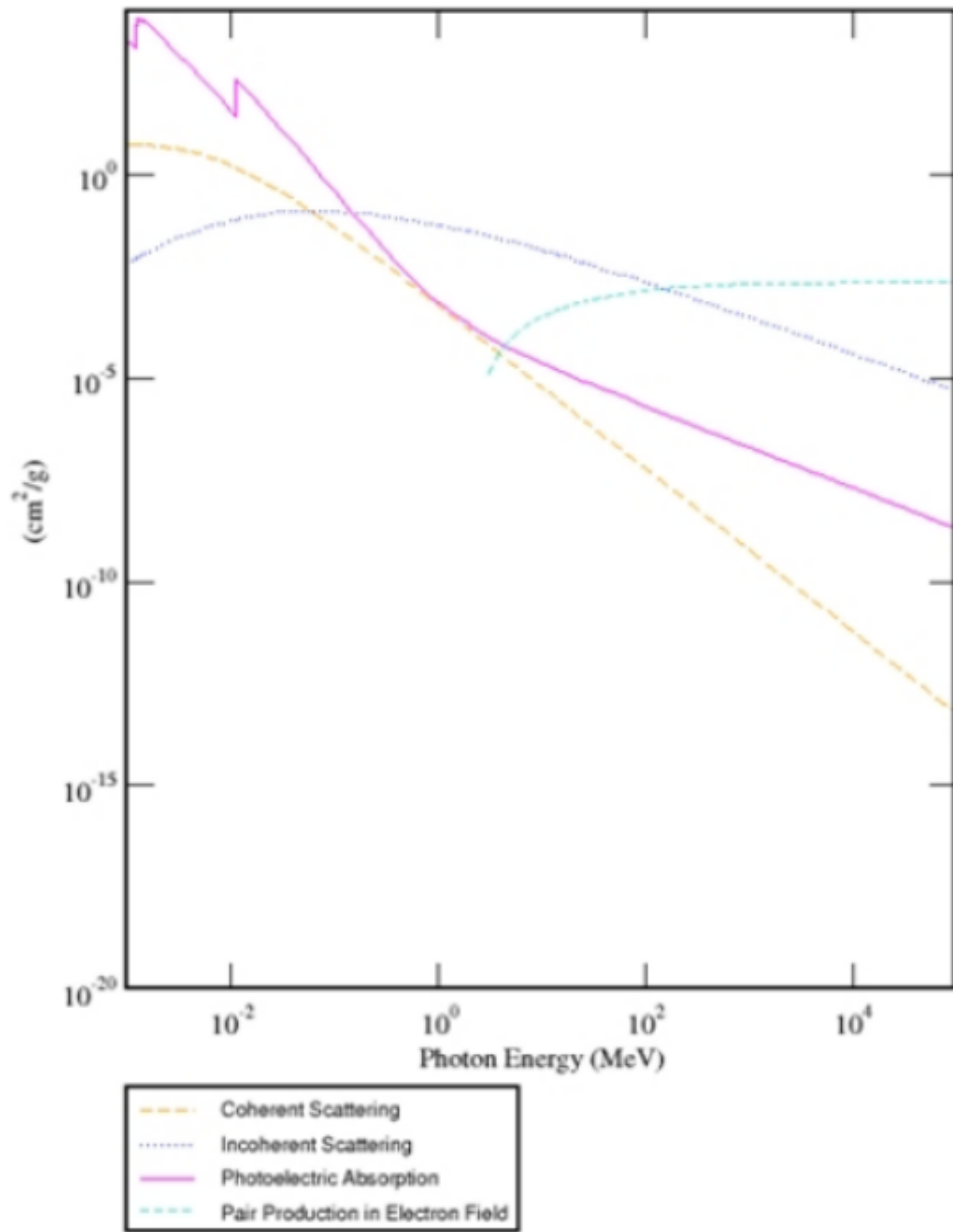


FIGURE 3.3: A plot displaying the cross-sections of the competing processes by which gamma rays interact with matter at different energies. Taken from [75]

3.3.1 Compton Scattering

Compton scattering occurs when an incoming photon deposits an amount of its energy into an atomic electron, changing its wavelength as defined in equation 3.1.

$$\Lambda' - \Lambda = \frac{hc}{mc^2}(1 - \cos(\theta)) \quad (3.1)$$

Where Λ' and Λ are the final and initial wavelengths of the gamma ray, h is Planck's constant, c is the speed of light in a vacuum, m is the rest mass of the electron and θ is the scattering angle of the gamma ray. The energy of the gamma ray after scattering is defined in 3.2

$$E'_\gamma = \frac{E_\gamma}{1 + \frac{E_\gamma}{mc^2}}(1 - \cos\theta) \quad (3.2)$$

where E_γ and $E'_{\gamma'}$ are the initial and final energies of the photon. The kinetic energy of the recoil electron is then defined in equation 3.3.

$$E_e = E_\gamma - E'_{\gamma'} \quad (3.3)$$

The cross-section of compton scattering decreases with the energy of the gamma ray while increasing with the number of available electrons in the scattering material i.e. the Z value. The Klein-Nishina formula defines the probability of a photon to scatter at an angle θ into a solid angle $d\Omega$ [76].

$$\frac{d\theta}{d\Omega} = Z^2 r_0 \left(\frac{1}{1 + \alpha(1 - \cos\theta)} \right)^2 \left(\frac{1 + \cos^2\theta}{2} \right) \left(1 + \frac{\alpha^2(1 - \cos\theta)^2}{(1 + \cos^2\theta)[1 + \alpha(1 - \cos\theta)]} \right) \quad (3.4)$$

Where r_0 is the radius of the electron, α is the photon energy in units of the electron rest mass ($\alpha = \frac{E_\gamma}{mc^2}$).

3.3.2 Photoelectric Effect

The photoelectric effect is a phenomena which occurs when an incident photon deposits its full energy into an atomic electron of the detector material. Provided that the energy of the photon, E_γ is greater than the atomic binding energy of the electron,

BE, the electron will be ejected from the nucleus with kinetic energy, E_{e^-} as defined by equation 3.5.

$$E_{e^-} = E_\gamma - BE \quad (3.5)$$

This vacancy left in an electron shell will lead to successive de-excitations of higher orbital electrons resulting in the release of characteristic X-rays. The cross-section of such a reaction happening can be described by equation 3.6 [77].

$$\tau \propto \frac{Z^x}{E_\gamma^{3.5}} \quad (3.6)$$

Where x can take values of 4 or 5 depending on the energy of the electron, Z is the proton number of the material and E_γ is the energy of the gamma ray.

3.3.3 Pair Production

Pair production is a process which photons can undergo when interacting with the Coulomb field of the nucleus if they are above 1.022 MeV in energy - the rest mass of an electron-positron pair. This particle-antiparticle pair is spontaneously created with the photon losing energy and the nucleus experiencing a kick from the change in momentum. The positron will go on to interact with the detector material resulting in an annihilation and the release of a 0.511 MeV gamma ray which is often seen in gamma-ray spectra when observing high energy emissions. This process also gives rise to single and double escape peaks with the original gamma ray appearing either 0.511 MeV or 1.022 MeV lower than its actual energy.

3.4 The GSI Accelerator System

Beams provided at GSI begin their life at the UNIversal Accelerator (UNILAC) which can accelerate ion species from protons to Uranium ions to 11.4 MeV/u (16%c). The Electron Cyclotron Resonance source is used to create highly charged ions at low intensities by feeding a radiation with frequency equal to the natural frequency of rotation of electrons in magnetic fields. The source injects microwaves into a gas filled volume with a magnetic field applied across it which gradually increases the perpendicular kinetic energy of the electrons which can then in turn ionise the gas. These ions are then pre-accelerated along a Radio Frequency Quadrupole (RFQ). The beam is then

accelerated further along the Inter-Digital (IH) cavities to 14 MeV/u through a gaseous medium with the goal of stripping electrons to alter the ionic charge of the beam. The modular Alvarez DTL cavities then sequentially accelerate the beam to its maximum energy with a series of single gap resonators by providing a longitudinally constant axial electric and an azimuthally constant magnetic field. This allows the operators to set the beam energy to a desired value, the maximum and minimum of which depends on the mass to charge ratio of the ion.

The beam from the UNILAC is injected into the SIS18 synchrotron where the beam is further stripped through the use of carbon foils. The synchrotron has a circumference of 216 m with a maximum bending power of 18 Tm. RF acceleration is then achieved with 2 16 kV cavities. The ion beam is then delivered to the various experimental chambers. In the case of S480 the SIS18 delivered a ^{124}Xe beam at an energy of 980 MeV/u. An overall view of GSI beam production and delivery system is displayed in figure 3.4.

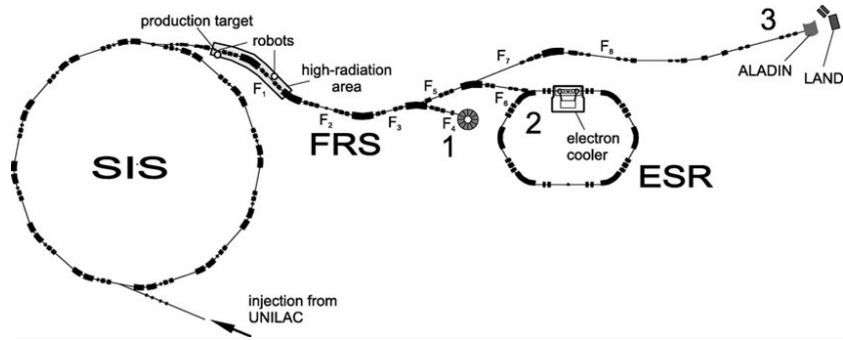


FIGURE 3.4: A schematic of the beam production and delivery system at GSI taken from [78].

3.5 The Fragment Recoil Separator

The GSI Fragment Recoil Separator (FRS) [79] is a magnetic spectrometer designed to separate cocktail beams of the products of nuclear fragmentation reactions. The FRS is coupled to the SIS18 synchrotron where stable beams may be accelerated to 4.5 GeV/u for H beams and up to 1 GeV/u for uranium beams and are then impinged upon Be and Pb targets between thicknesses of 1 to 8 g/cm². A combination of magnetic quadrupoles and dipoles, slits and degraders allow the beam to be selected and transported through the separator where they are separated using the $B\rho - \Delta E - B\rho$ method. This method separates fully stripped ions via the different magnitudes of their deposited energy in the degrader with the energy deposited being proportional to their mass to charge ratio or A/Z. This separation works up to a magnetic rigidity of $B\rho = 18$ Tm with the

separator being available for use in monochromatic and achromatic modes by use of a wedge-shaped degrader in S2. A full schematic of the FRS can be seen in figure 3.5.

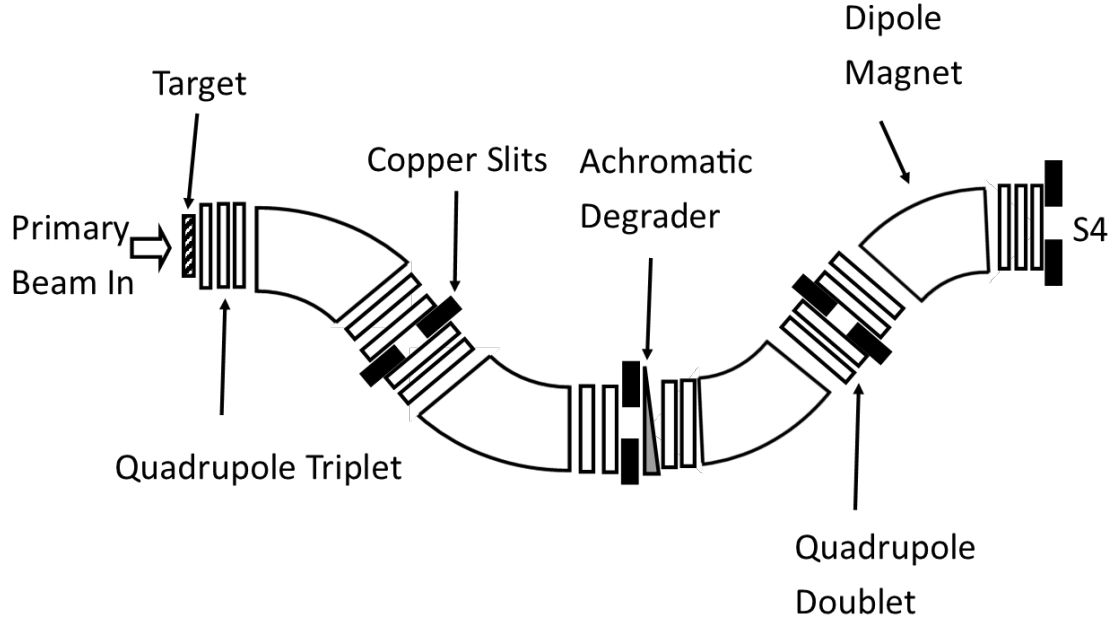


FIGURE 3.5: A diagram detailing the path a beam takes through the FRS and the magnets which are used to steer the beam, adapted from figure 7 of reference [79].

Achromatic mode is the standard mode of operation where the final fragment position is independent of its momentum and angular spread which results in ions with the same $B\rho$ being focussed to the same position in the focal plane. The motion of ions in the magnetic fields within the separators are defined by the Lorentz force and is described by equation 3.7.

$$B\rho = \frac{p}{qe} = B\gamma \frac{m_0}{qe} = B\gamma c \frac{uA}{qe} \quad (3.7)$$

Where B is the magnetic field of the dipole magnets, ρ defines the radius of bending, p is the ion's momentum, q is the charge state of the ion, and e is the charge of an electron. A number of X-directional slits exist in the focal planes of S1, S2, S3, and S4 which are enabled to reduce contaminants across different projected paths in the separators with an additional homogeneous degrader in S1 for certain use cases. Keeping the energy of the fragments as high as possible, generally >400 MeV/u, helps in improving separation and minimises the production of unwanted charge states. Due to the high energy of the ions a degrader is required in the S4 focal plane to reduce the velocity of the ions to ensure implantation in the AIDA DSSSD. In the case of the S480 experiment the ions were fully stripped meaning the charge, q , was equivalent to the proton number.

Particle identification is calculated via the $B\rho - TOF - \Delta E$ method which reconstructs the position of the ions through a measure of their magnetic rigidity at S2 and S4 as well as the TOF between the two focal planes. An analysis of this data allows for the calculation of Z and A for each ion. A pair of time projection chambers exist between the two focal planes to precisely determine the position of the ions and fast plastic scintillators are used to measure the TOF with high rates at the S2 focal plane limiting the performance of the scintillators. Two Multiple Sampling Ionisation Chambers (MUSIC) detectors are positioned either side of a stripper foil to measure the charge of the ions with an additional scintillators present after the S4 degrader (SC42) to help with the identification of unreacted ions incident on AIDA.

3.6 The DESPEC @ GSI Set-up for S480

The DESPEC [8] set-up is positioned in the S4 focal plane of the FRS. This section will discuss the detectors which were present and used in the experiment and analysis of S480. A photograph of the 2020 set-up is seen in figure 3.6.

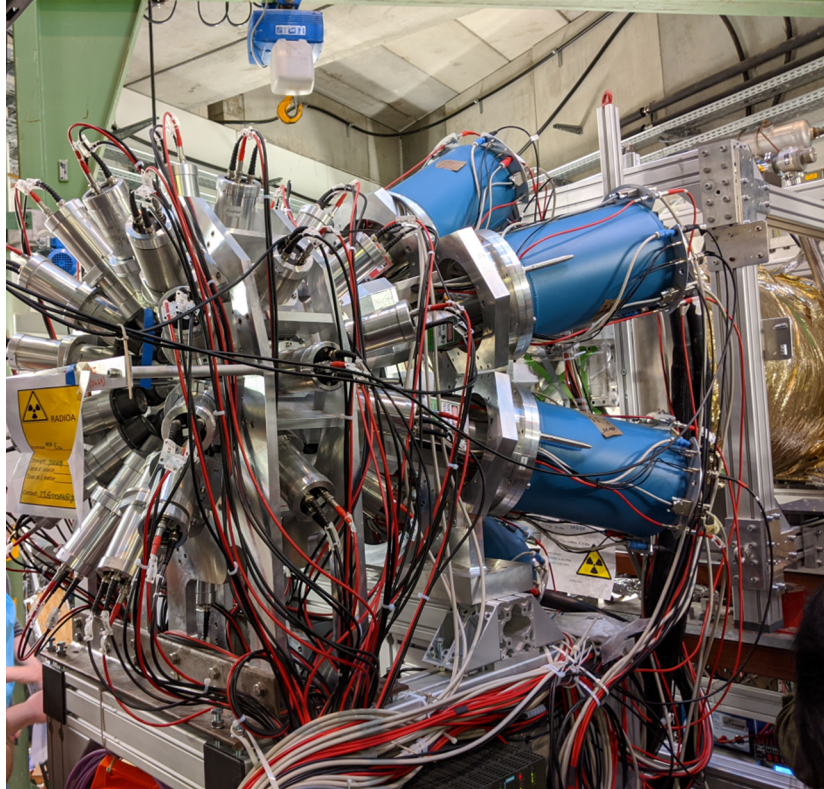


FIGURE 3.6: A photograph of the DESPEC set-up in March 2020 as used for the commissioning run of the set-up.

3.6.1 AIDA

The Advanced Implantation Detector Array (AIDA) is comprised of a variable number of Double Sided Silicon Strip Detectors (DSSSDs) which are used for the detection of implanted heavy ions as well as beta decays from the implanted species. The number of layers used depends on the variation of energies between the radionuclides of interest being transported through the FRS as the layers work in tandem with degraders and the active stopper to slow ions which ensures implantation. Each DSSSD measures $8 \times 8 \text{ cm}^2$ or $8 \times 24 \text{ cm}^2$ depending on the distribution of ions coming from the FRS with either 128×128 or 128×384 strips which result in 16384 or 49152 pixels. This high degree of pixelation allows for a highly sensitive position identification of implants which are then able to be correlated with consequent decays. In the case of S480 AIDA was set up in its $8 \times 8 \text{ cm}^2$ format.

Ions stopped in the DSSSDs often deposit energies in the range of several GeV while the following decays deposit energies on the order of $\sim 50 \text{ keV}$ to several MeV with a delay between the two events on the order of tens of ms to several tens of seconds depending of the half-life of the implanted species. The Application Specific Integration Circuit (ASIC) chip was developed [80] to cope with the high volume of data being collected over different energy ranges by autonomously switching between the high and low energy ranges required with a recovery time of $<40 \mu\text{s}$. The ASIC chip is timestamped by a 500 kHz clock while the ADC data is timestamped by a 500 MHz clock the high speeds of which are vital due to the high frequency of data generated by beam implants and subsequent decays. The AIDA DAQ consists of 64 channel FEE64 modules which takes in the data from 4x16 channel AIDA ASICs with each FEE64 being able to handle data rates of up to 500,000 data items/s. AIDA runs in a triggerless mode where the FEE64 produces time ordered data with a 64-bit White Rabbit (WR) timestamp. The WR timestamp is provided via VETAR2 and PEXARIA5 receiver modules and are distributed through all of the FEE64 modules by MACB clock distribution modules. In the case of S480 AIDA was run in a single stack of three DSSSDs.

3.6.2 β -Plastic

The β -Plastic detector is a fast-timing plastic scintillation detector designed for the detection of β particle decays from implants in the AIDA DSSSDs. The detector is composed of a square 3 mm thick sheet of BC-404 plastic scintillation material and is coupled to a $3 \times 3 \text{ mm}^2$ SensL C-series Silicon PhotoMultiplier (SiPM). The detectors are able to measure beta implants in a range of $\sim 80 \text{ keV}$ to 8 MeV with excellent, precise

timing abilities in the 1 ns range with one being placed either side (up and down stream) of AIDA. The SiPM signals are passed through 'booster boards' which boost the signal by a factor of 10 and are then fed into TAMEX cards with TwinPeaks front ends, both of which were developed at GSI. The detector measures $8 \times 8 \text{ cm}^2$ but can also be set-up in a $24 \times 8 \text{ cm}^2$ configuration depending on whether the single or wide AIDA set-ups are used.

The output of the detector comes in the form of the time-over-threshold (ToT) which refers to the time difference between the leading and trailing edge discriminator threshold crossings. This time is proportional to the amount of light collected by the SiPMs and is therefore also proportional to the energy of the implanted particle or photon. The β -Plastic detector can also be used as implantation detectors which can allow for vetoes to be placed on light ions passing through the DSSSD stack without being stopped.

3.6.3 High Purity Germanium

At the time of S480 six triple Germanium Cluster detectors (GTCs) from the GALILEO array were positioned centred on the AIDA array to capture the energy and timing data of isomer delayed gamma rays. The detectors are set-up to run in normal or addback mode with the addback algorithm combining compton scattered gamma rays back together to reconstruct full energy peaks. The array reads out data through a 14 Bit 100 MHz FEBEX digitiser developed at GSI. This system contains an on board FPGA which applies a trapezoidal filter algorithm to obtain information about the energy while the timing information is obtained by a constant fraction discriminator (CFD).

3.6.4 The FAst TIMing Array - FATIMA

The FAst TIMing Array (FATIMA) [4] is a key part of the DESPEC setup in the context of carrying out highly precise measurements of the half-lives of nuclear states. The array has been used in a vast range of laboratories and experimental settings accross the world. Some of these research applications include detecting gamma rays from 2n-transfer reactions at IFNN-HH as part of the ROSPHERE experimental group [81, 82], thermal neutron induced fission on ^{235}U and ^{239}Pu [83–86] at the FATIMA + EXILL campaign and ^{252}Cf fission source experiments [87]. More recently FATIMA has been involved in the NuBALL collaboration giving rise to $\gamma - \gamma$ fast timing spectroscopy results [88–90] as well as involvement in the STELLA setup for nuclear astrophysics for $^{12}\text{C} + ^{12}\text{C}$ fusion event identification [91, 92] and finally at RIKEN in conjuction with the EURICA array for beta-delayed fast timing measurements [93, 94]. The array consists

of 36 cerium doped Lanthanum Bromide ($\text{LaBr}_3(\text{Ce})$) scintillation detectors which are used for the acquisition of energy and timing information of gamma rays. The crystals measure a 1.5" diameter with a length of 2" and are hermetically sealed within an aluminium casing along with a removable 4 mm lead shield which acts to minimise the scattering between detectors. The detectors are coupled to fast R9779 photomultiplier tubes (PMT) and were arranged in 3 rings of 12 detectors. Figure 3.7 shows an view of the array from the inside. The 36 FATIMA detectors were evenly split between 3 rings positioned at angles of $\theta = 46^\circ$, 94° and 134° with each detector in the ring being separated by $\phi = 30^\circ$ at a distance of 17 cm from the center of the central AIDA DSSSD.

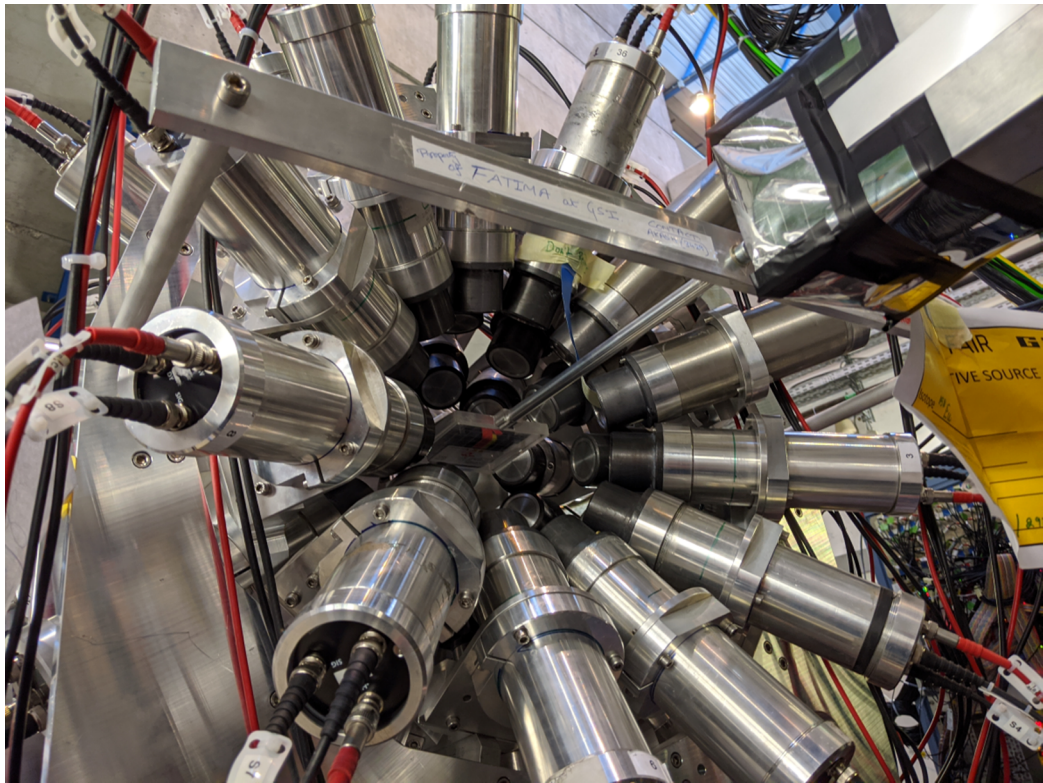


FIGURE 3.7: A photograph showing an interior view of the FATIMA array taken at GSI in March 2020.

FATIMA runs in a triggerless mode to maximise data collection with two signals being sent out to VME and TAMEX electronic systems which operate mutually exclusively of each other. The VME-DAQ signals are processed using V1751 CAEN digitisers which operate using the Digital Pulse Processing - Pulse Shape Discrimination (DPP - PSD) firmware created by CAEN. A charge to digital conversion (QDC) system is used to extract energies while CAEN V812 CFDs coupled with V1290 Time to Digital Converters (TDC) are used to obtain timing information. Each TDC board consists of 32 channels with 2 boards being required for S480. This allowed for the inclusion of a

TDC readout for scintillators 41 and 42 which provided an easy method for observing time differences between a heavy ion signal very close to AIDA and a gamma-ray time. Following the experimental runtime an error was found in the synchronisation of clock times between the TDC boards which caused a small portion of the time differences between two boards to be offset by 25 ns. This relic was not treatable in the analysis stage of the data but only affected the measurements of half-lives of states longer than 5 ns as after the 25 ns had passed the state would have almost completely decayed, having existed for 5 half-lives.

The TAMEX-DAQ system acts on similar principles to the β -Plastic TAMEX system with the electronics being optimised for use on FATIMA-PMT signals. TAMEX modules are FPGA based TDCs which measure the leading and trail edge of signals to determine their ToT which has a logarithmic relationship with the energy deposited into the detector. The TAMEX system offers a timing resolution of 11 ps along with a low dead time ($20\ \mu\text{s}$) and a collection window of $\sim 320\ \mu\text{s}$.

The combined employment of both HPGe and LaBr₃ detectors in the set-up provide an excellent balance of fast timing response and high resolution when compared to other detectors. While other scintillation detectors such as NaI, CeBr₃, BGO and many others exist, none provide a better timing resolution for time differences between gamma rays as LaBr₃ which possesses a timing resolution of 320 ps. The downsides of using LaBr₃ mainly comes from their internal radioactivity and their relatively high cost when compared to other crystals but these are worth the best possible timing resolution. Similarly, HPGe detectors are the state-of-the-art for peak identification in spectroscopy due to their excellent energy resolving capabilities of 0.5% at 1 MeV. The combined use of these gamma-ray detectors therefore provide the best combination of energy and timing measurement capabilities - the prime quantities of concern in experiment S480.

3.7 Event Building

In order to combine and create coincidence data a rigorous event building method is used. This section will discuss the data stream which can be seen in figure 3.8, the White Rabbit clock which is pivotal to the realisation of coincidences as well as the timestamping process.

3.7.1 MBS

Each DESPEC subsystem other than AIDA has its own Multi Branch System (MBS) DAQ which was developed at GSI. These data streams are then merged using

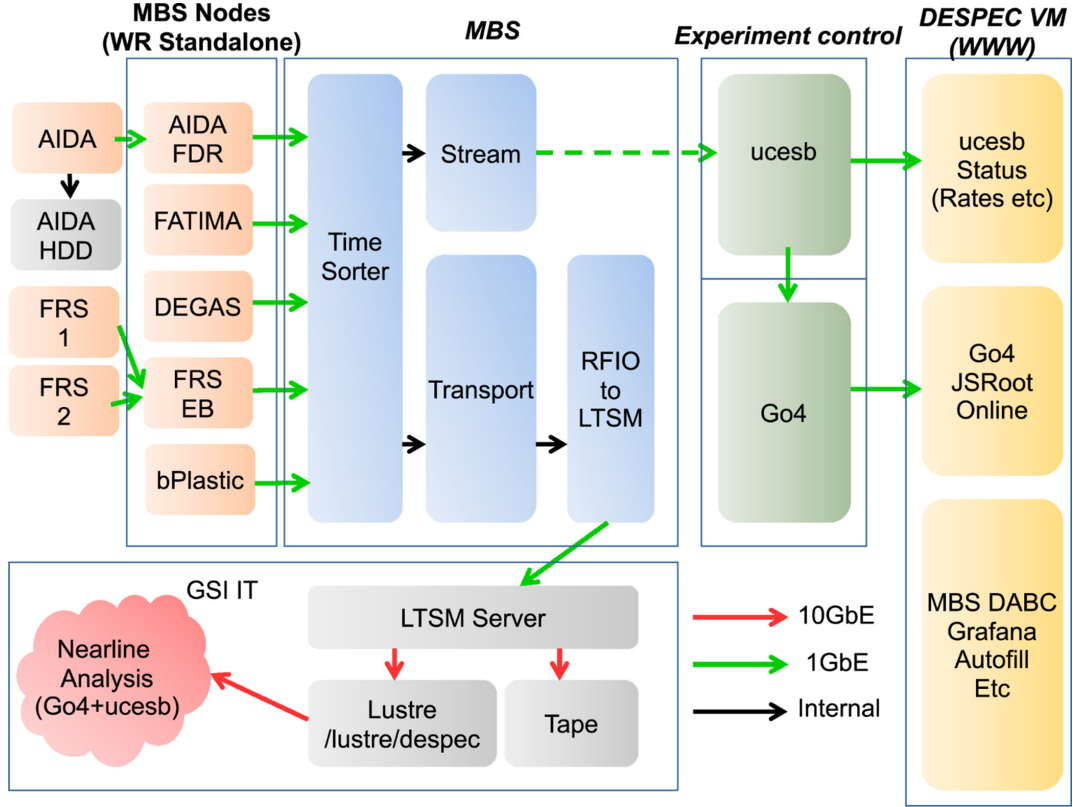


FIGURE 3.8: A flowchart explaining the datastream coming from the various DESPEC detectors showing the processes which combine them into coherent analysable data.
Taken from reference [8].

a time-sorting event builder which relies on the White Rabbit clock. In order to do this, the unpack and check every single bit (ucesb) process is required. This timesorter uses a 2 Hz synchronisation pulser to ensure that all connected DAQs are sending data simultaneously.

3.7.2 White Rabbit

The absolute start time of White Rabbit timing started at midnight on January 1st 1970. This signal is driven by a 125 MHz clock and is distributed to the various detector systems by an ethernet connection. This clock is used to synchronise all of the detector systems to create coincident events across detectors. The accuracy of the timestamp can be up to 1 ns but each detector system uses a different timing board to receive the signal which varies its accuracy. Table 3.1 displays the different timing boards for each detector system as well as their accuracy.

Detector System	Timing Electronics	Timing Card	Accuracy (ns)
FATIMA + FRS	VME	VETAR2	8
FATIMA + β Plastic	TAMEX	PEXARIA5	1
HPGe	FEBEX	PEXARIA5	0.1
AIDA	TAMEX	VETAR2/PEXARIA5 (HDMI)	0.125

TABLE 3.1: A summary of the timestamp accuracy of the White Rabbit clock for the different DESPEC subsystems depending on their timing electronics.

In order to synchronise the multiple subsystems a logic module was designed and constructed at GSI. The module creates two output pulses for every input pulse. The first of these is instantaneous with the second pulse being variable. When the first pulse fires the second variable pulse is also fired and consecutively fired at a rate of one every 50 ns after the initial hit. This means the n^{th} pulse occurs $(n - 1) \times 50$ ns after the first pulse with the cycle restarting every 32 or 64 iterations. By studying the time differences between the two signals it is possible to synchronise the data from the different subsystems.

3.7.3 ucesb Timestitching

The unpack and check every single bit (ucesb) code is used to build AIDA events and to time stitch the data for coincidence analysis. The timestitching process uses the white rabbit time stamps of signals from different subsystems to create coincidence events. This algorithm will take any two events from subsystems (or sub-events) within 2 μ s of each other and combine them into a single coincidence event. If any events come within 2 μ s of the latest sub-event it will also be combined into this event. Once a window of 2 μ s where no sub-events are detected the full event is considered complete. This pre-sorting allows for data to be written in a ROOT tree format which allows a full coincidence analysis between detector subsystems to be carried out.

Chapter 4

Gamma-ray Spectroscopy using DeSPEC

4.1 Experimental Details

The experimental data analysed in this thesis was obtained from experiment S480 of the DESPEC collaboration at the GSI Helmholtz Centre for Heavy Ion Research. A 980 MeV/nucleon ^{124}Xe primary fragmentation beam was impinged on a 4 g/cm^2 thick ^9Be target over the period of a week. The reaction products were transported into the FRS to be fully charge stripped and then separated according to their mass to charge ratio by setting the magnetic field strengths of the dipole magnets to focus the beam on ^{94}Pd ions. A cocktail of fully stripped ions were then fed through the SC41 and SC42 scintillators which sandwich a degrader, transported through the bPlast plastic scintillator for beta particle and heavy ion detection and implanted in one of three DSSSDs which make up AIDA. The gamma-ray emissions of these ions were then measured in the FATIMA and GTC arrays with the goal of ascertaining decay data pertaining to the isomeric 14^+ state in ^{94}Pd and the 8^+ states in ^{96}Pd and ^{94}Ru .

4.2 Particle Identification Spectra and Gating

The DESPEC system consists of a number of particle detectors which were used to place high precision gates on the gamma rays which were detected by the set-up. To begin identifying the ranges of these gates an initial gate was placed on the measured Z and A/Q of nuclei passing through the separator. The plot used to place these initial gates can be seen in figure 4.1 which shows the Z vs A/Q plot for ions that register

an energy tag in the S4 scintillator. The values of Z and A/Q were calculated by the $B\rho - TOF - \Delta E$ method.

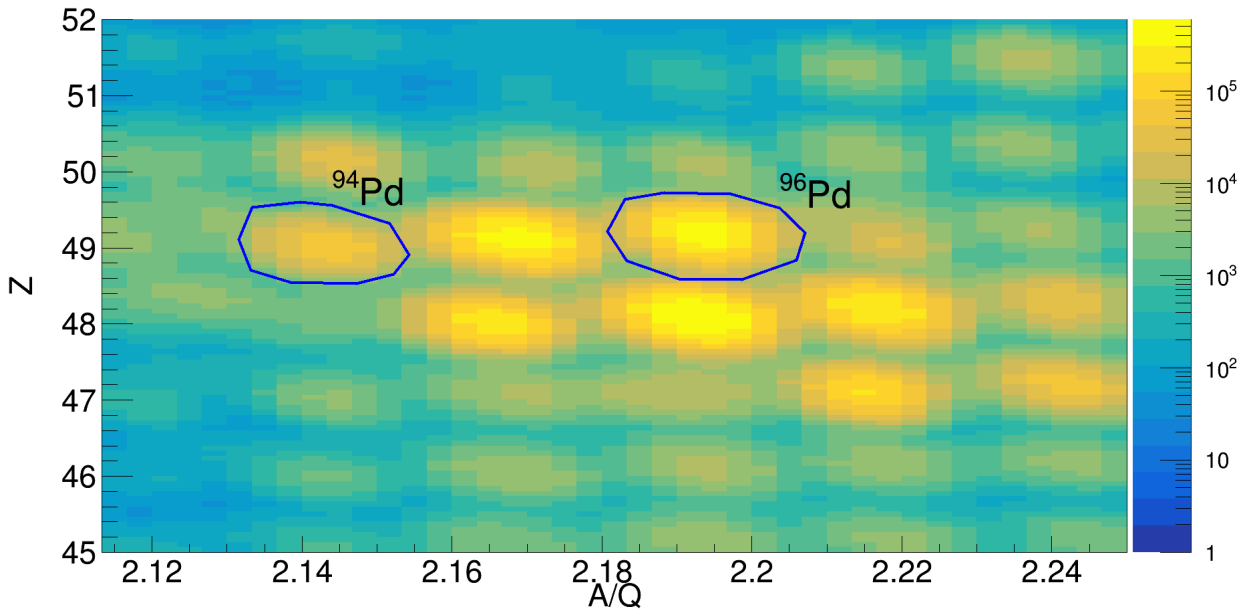


FIGURE 4.1: The measured, calibrated Z vs A/Q matrix for nuclei passing through the FRS from a subset of the data from S480.

Despite the slight offset in calibration the initial gates were placed on the particle identification regions corresponding to ^{96}Pd and ^{94}Pd ions seen in figure 4.1 and the resulting gamma rays seen in FATIMA between 40 ns and 400 ns after implantation in AIDA are shown in figures 4.2 and 4.3 respectively, with figures 4.4 and 4.5 showing the GTC response for gamma rays arriving 500 ns to 6 μs after implantation. These gating regions were chosen as they were amongst the most highly populated radionuclides with all of the highly populated regions also being checked for coincident gamma rays. These values when gated on, if correct, would show the expected gamma rays which decay from the isotope each region represents without those from other neighbouring species.

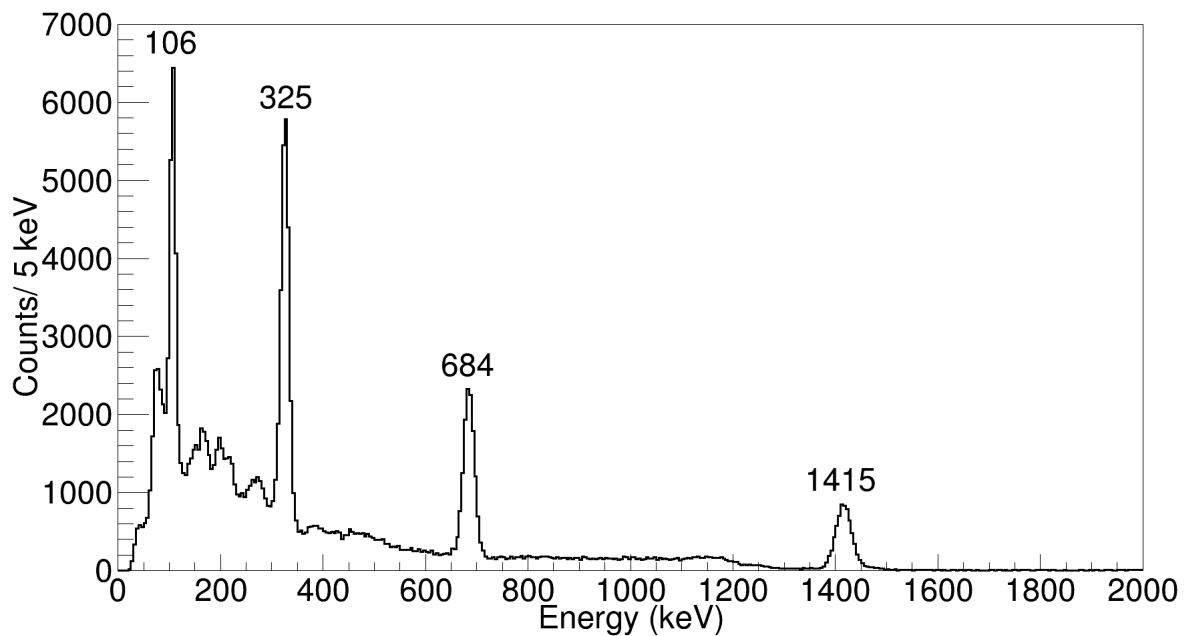


FIGURE 4.2: The γ rays detected by the FATIMA array between 40 ns and 400 ns after prompt implantation when gating on ^{96}Pd ions seen in the Z vs A/Q matrix.

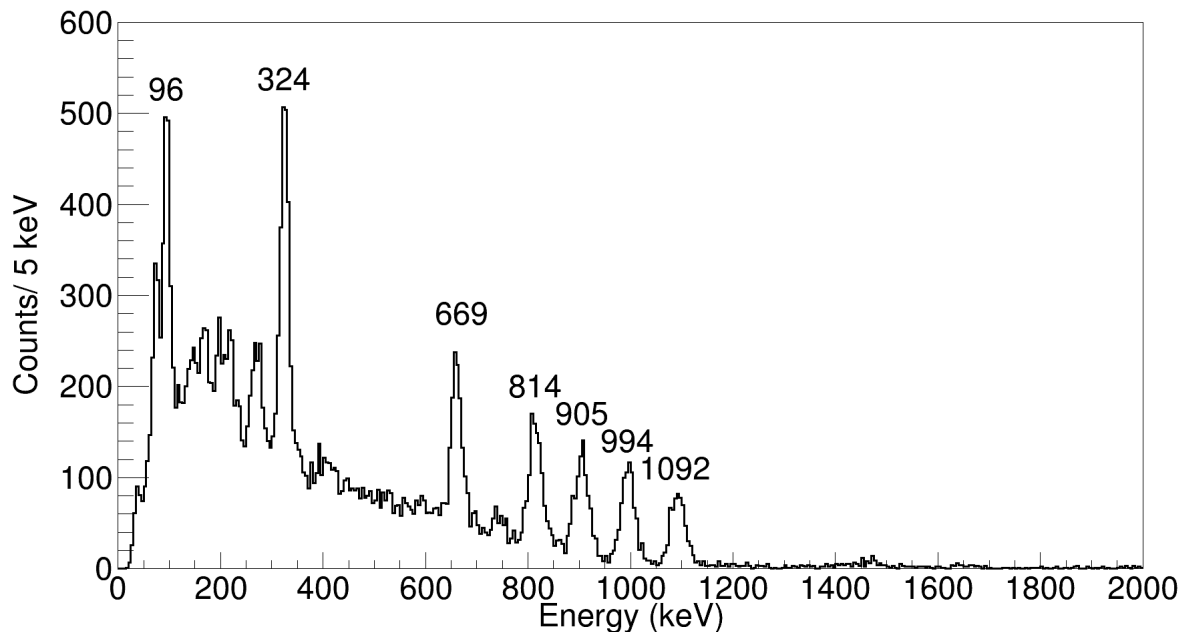


FIGURE 4.3: The γ rays detected by the FATIMA array between 40 ns and 400 ns after prompt implantation when gating on ^{94}Pd ions seen in the Z vs A/Q matrix.

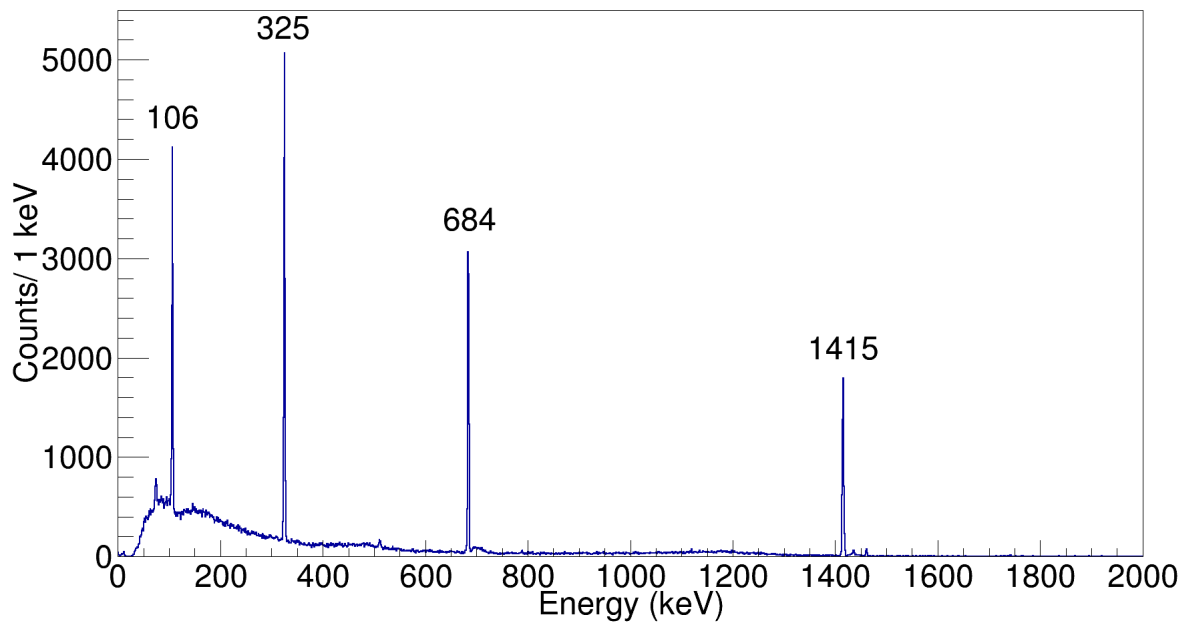


FIGURE 4.4: The γ rays detected by the germanium detectors between 500 ns and 6 μ s after prompt implantation when gating on ^{96}Pd ions seen in the Z vs A/Q matrix.

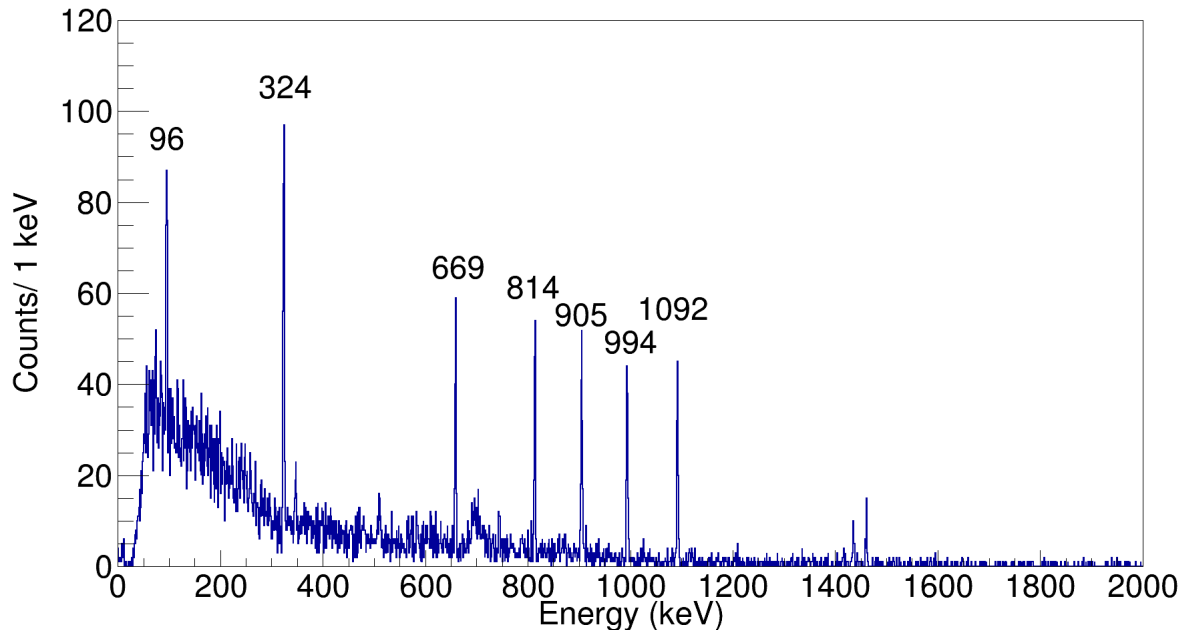


FIGURE 4.5: The γ rays detected by the germanium detectors between 500 ns and 6 μ s after prompt implantation when gating on ^{94}Pd ions seen in the Z vs A/Q matrix.

Each of these spectra show the expected gamma rays from each species with an additional two spectral peaks clearly present in figure 4.5 at 1435 keV and 1461 keV, which appear as a result of the internal decay of ^{138}La and natural background of

^{40}K respectively. By gating on individual prompt delayed gamma-ray transitions seen by the FATIMA array one is able to reverse gate on the Z vs A/Q spectra to better understand the positioning of the Pd ions and therefore refine the gating conditions used to produce spectra. The most effective transitions to gate on were those of the highest energy, with those being the 1415 keV $2^+ \rightarrow 0^+$ and 1092 keV $8^+ \rightarrow 6^+$ gamma rays in ^{96}Pd and ^{94}Pd respectively, due to the absence of any compton background from higher energy transitions in the spectra. Despite this, the background subtraction in Z vs A/Q improved the efficacy of the method when dealing with lower energy transitions. For these reasons the 106 keV and 684 keV transitions in ^{96}Pd and the 994 keV, 905 keV, 814 keV, 659 keV and 96 keV transitions in ^{94}Pd , along with the aforementioned 1415 keV and 1092 keV transitions were selected for this technique. Unfortunately, the 324 keV and 325 keV transitions were too similar in energy to be used to produce valuable spectra. If the Z vs A/Q regions of the 2D matrix of the resulting spectra looked to be similar to the applied gates in 4.1 the effectiveness of the PID systems would be proven. A background subtraction was carried out by projecting the coincident ion Z vs A/Q values seen when gating on a gamma-ray peak region from FATIMA and subtracting the Z vs A/Q spectra found when gating on a background region with the same width but higher in energy than the gamma-ray peak.

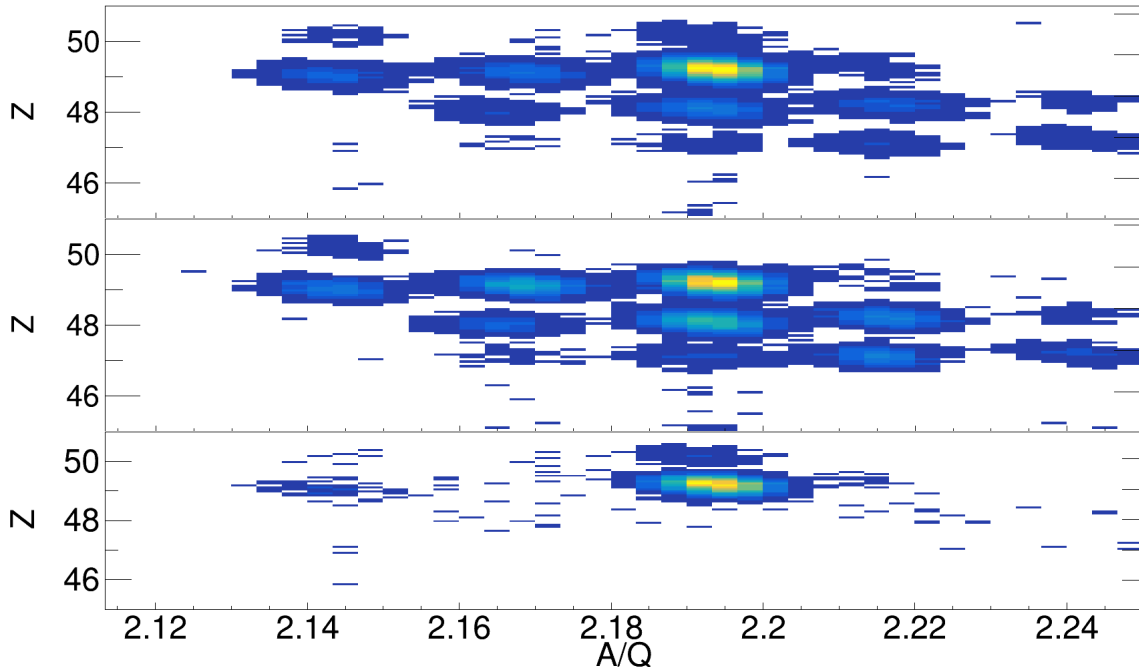


FIGURE 4.6: The Z vs A/Q of ions generated in the FRS detected in coincidence with a 106 keV γ ray detected by FATIMA 40 ns - 400 ns after prompt implantation (upper), the background region of 106 keV (central) and the subtraction of the central plot from the upper plot (bottom).

Figure 4.6 shows the outcome of this analysis with the upper plot in 4.6 showing

the Z vs A/Q for particles associated with a 106 keV gamma ray detected in FATIMA 40 - 400 ns after the prompt flash while the central plot shows the background spectra gated on background gamma rays detected at a higher energy with the same peak width as the 106 keV transition. The bottom plot in 4.6 is the result of a subtraction of the central from the upper plot and shows a clear reduction in the background coming from neighbouring species. By combining this spectra with the same versions for other transitions in ^{96}Pd and doing the same for the viable transitions in ^{94}Pd it was possible to accurately redefine the Z vs A/Q gates with a high level of confidence as well as proving the robustness of the FRS detectors along with the event building and time stitching processes.

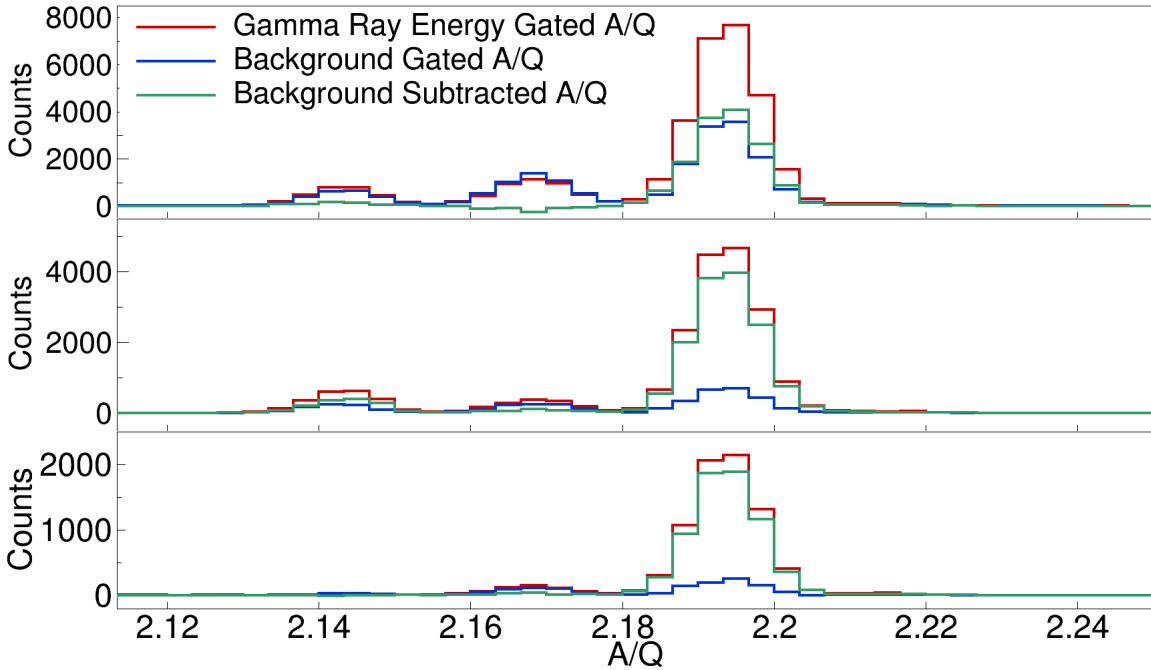


FIGURE 4.7: The $Z = 46$ projections of the Z vs A/Q of ions measured in the FRS detected in coincidence with the 106 keV (upper), 684 keV (central) and 1415 keV (bottom) transitions in ^{96}Pd measured 40 ns to 400 ns after prompt implantation. These spectra have been background subtracted and the γ rays of interest were detected post-prompt.

The projections of the background subtracted reverse gated A/Q of ions can be seen in figure 4.7 for the 106 keV (upper), 684 keV (central) and 1415 keV (bottom) transitions respectively. The 106 keV analysis shows the largest background region along with some over-subtraction due to its low energy and therefore proximity to delayed gamma rays from the prompt flash and therefore the maximum amount of Compton scattered gamma rays. Comparatively the 1415 keV gate shows the least amount of improvement and subtraction due to its already low levels of background while the 684 keV gate shows a middling level of improvement from background subtraction. These

Z vs A/Q of these plots were combined to define a tighter, more accurate gating region for ^{96}Pd ions.

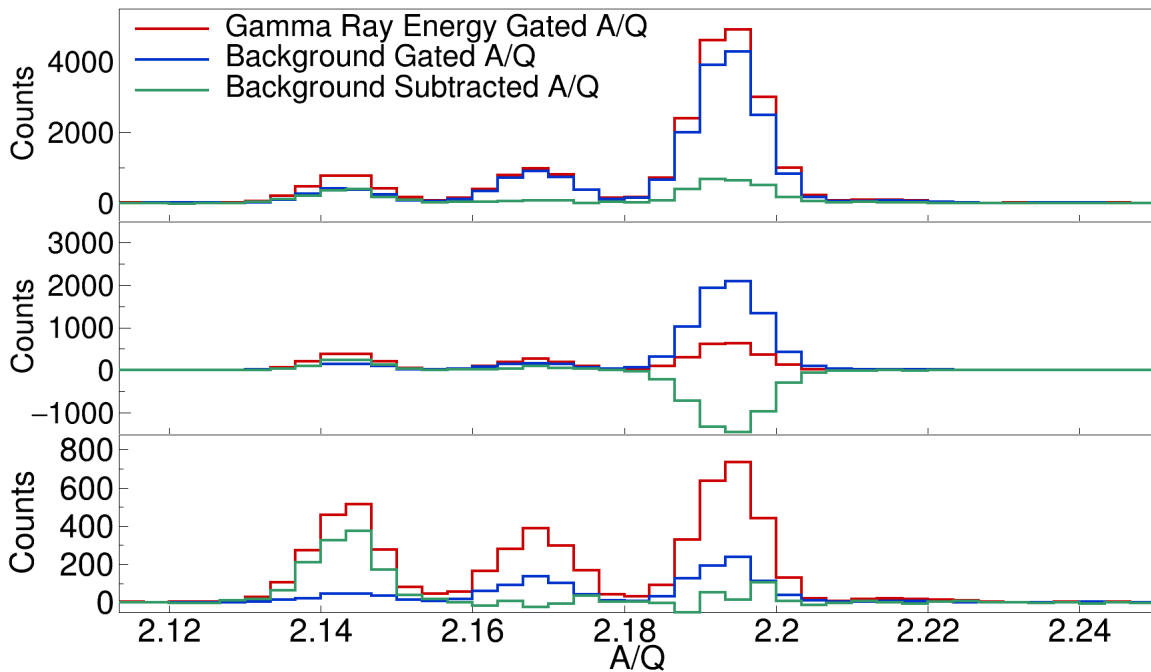


FIGURE 4.8: The $Z = 46$ projection of the Z vs A/Q of ions generated in the FRS detected in coincidence with the 96 keV (upper), 659 keV (central) and 814 keV (bottom) transitions in ^{96}Pd measured 40 ns to 400 ns after prompt implantation. These spectra have been background subtracted and the γ ray of interest were detected post-prompt.

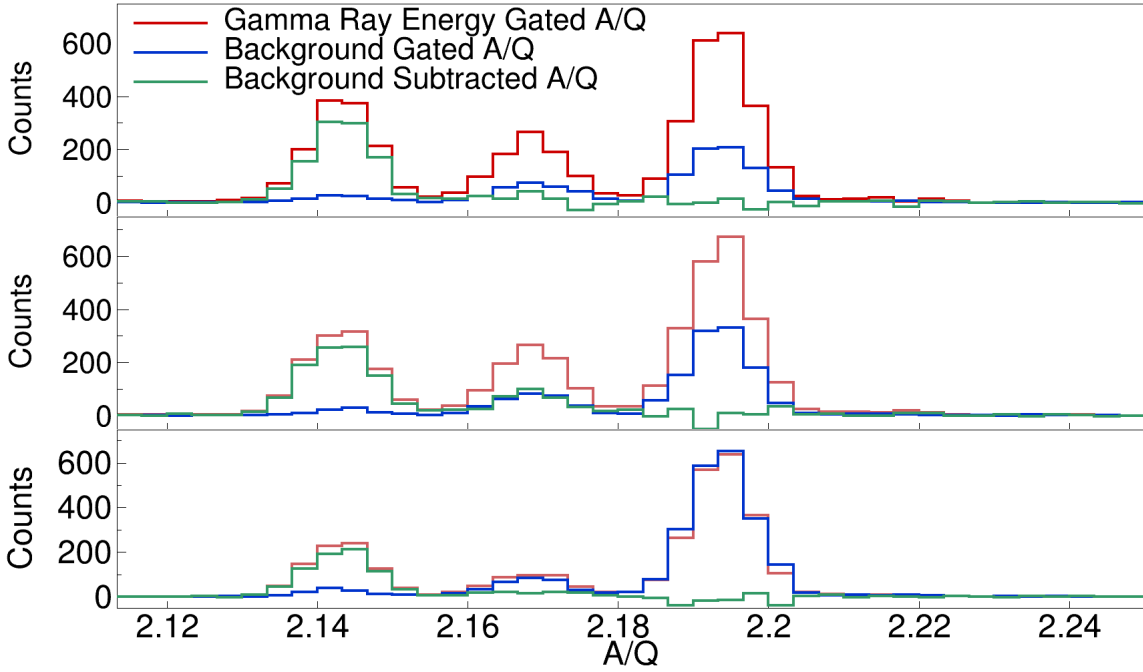


FIGURE 4.9: The $Z = 46$ projection of the Z vs A/Q of ions generated in the FRS detected in coincidence with the 905 keV (upper), 994 keV (central) and 1092 keV (bottom) transitions in ^{94}Pd measured 40 ns to 400 ns after prompt implantation. These spectra have been background subtracted and the γ rays of interest were detected post-prompt.

Analogous plots for ^{94}Pd are shown in figures 4.8 and 4.9 for low and high energy transitions respectively. The analysis seemed to favour the high energy transitions for the reasons discussed earlier as seen in figure 4.9 where the contaminants from ^{96}Pd and ^{95}Pd are almost completely removed. A slightly adjusted was employed when placing the background regions on the higher energy transitions due to their similar energies whereby smaller background regions between peaks were taken for the 814 keV, 905 keV and 994 keV subtractions and normalised for their ranges. The technique also seems to provide reasonable results for the low energy transitions as seen in figures 4.8 focussed on the 96 keV (upper) transition and focussed on the 814 keV transition (bottom). A large over-subtraction can be seen in the ^{96}Pd region of the central plot in figure 4.9 which is present due to the background region for the 659 keV transition overlapping with the peak region of the 684 keV transition in ^{96}Pd . Resultantly, the 659 keV gate was left out when deciding on a refined Z vs A/Q gate for ^{96}Pd .

It was also possible to carry out the same technique on other particle identification detectors such as AIDA, scintillators 41 and 42, and the β -Plastic detector. The energy response of scintillators 41 and 42, which are sandwiched by a degrader, were also studied when gating on the relevant high energy gamma rays in each isotope of interest. The

resulting SC41 vs SC42 energy spectra is shown in figure 4.10 with the highest energy gamma rays being used to minimize the effect of any compton scattering.

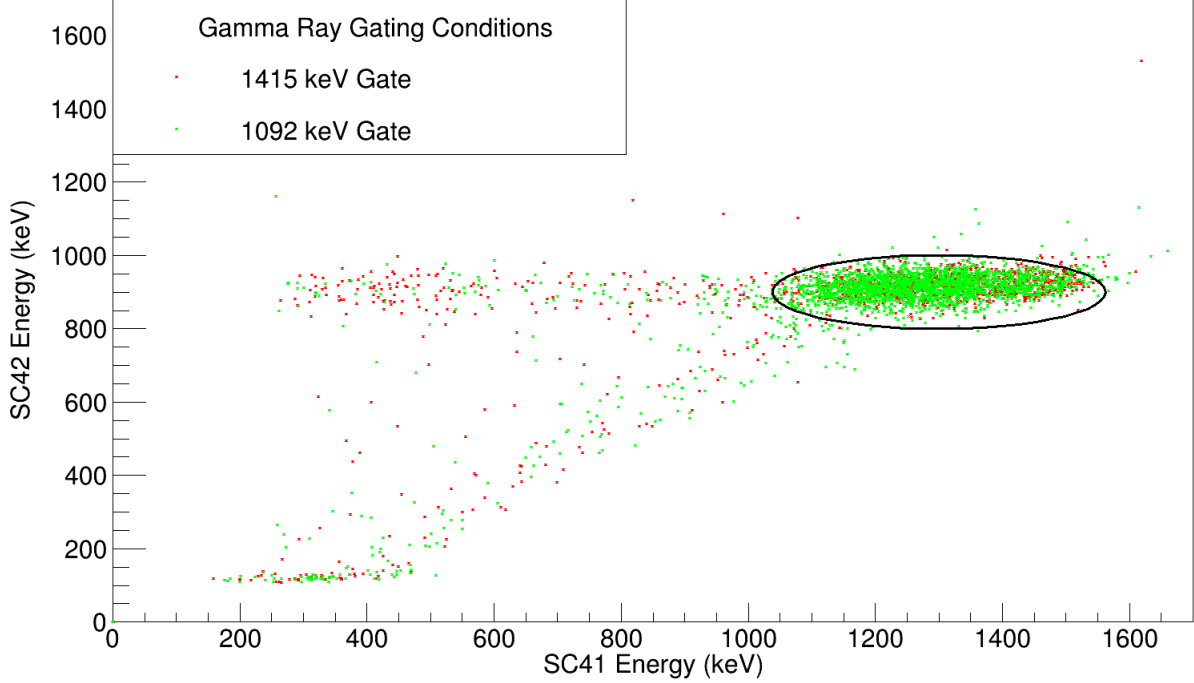


FIGURE 4.10: The SC41-42 energy spectra when gating on the prompt-delayed γ rays seen in FATIMA from the decays of ^{96}Pd (1415 keV) and ^{94}Pd (1092 keV). The black ellipse indicates the location of the resulting gate.

Here, a collection of events which are highlighted by the ellipse can be interpreted as passing through the degrader without undergoing nuclear reactions and were gated on as good events. Following this, the same methodology was used to determine the position of gates on the β -Plastic time over threshold parameter. Figure 4.11 shows the reverse gated spectra when observing the time over threshold measured by the detector and a gate was placed from 74000 ns - 78000 ns, enclosing the large peak in the region which represents the ions travelling through the FRS.

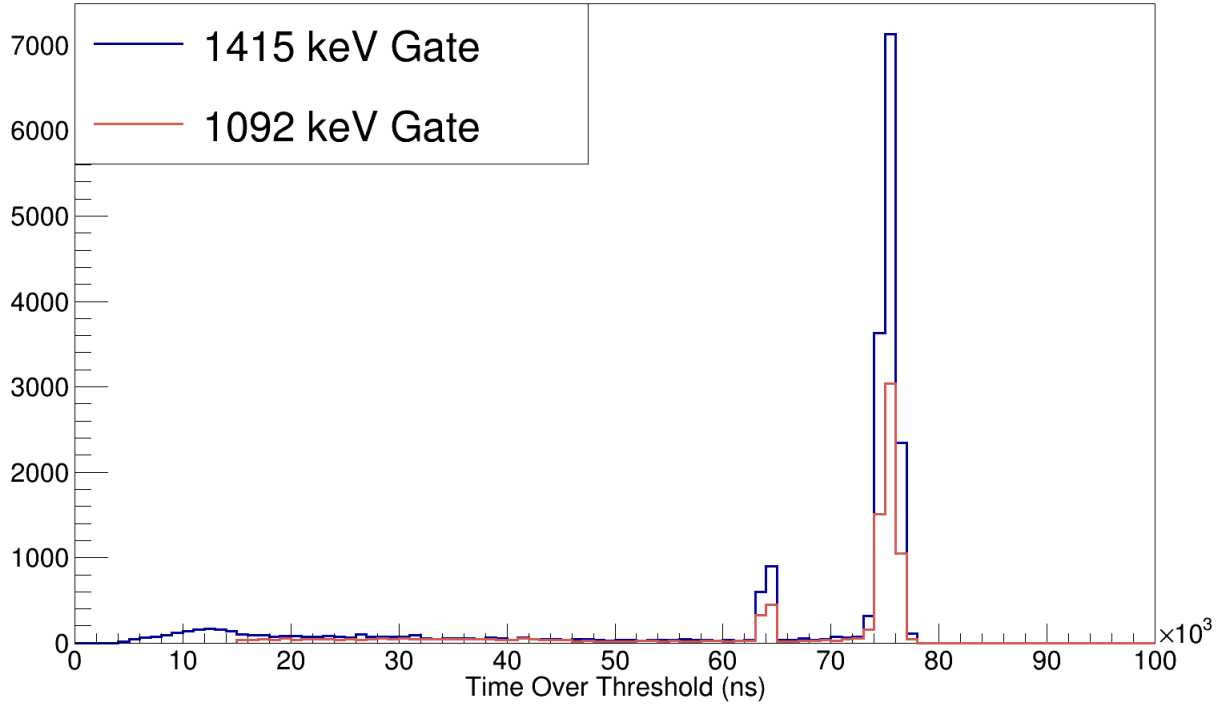


FIGURE 4.11: The β -Plastic Time Over Threshold (TOT) signal seen when gating on the prompt-delayed γ rays seen in FATIMA from the decays of ^{96}Pd (1415 keV) and ^{94}Pd (1092 keV).

Finally, a gate was placed on ions implanted in AIDA, defined by the boolean 'stopped' parameter which registers as true if there are no ions implanted in further AIDA layers and false for the opposite. This was the final gate which when combined with the SC41-SC42 energy deposited, bPlastic time over threshold and Z vs A/Q of ions in the FRS created the golden gating conditions for observing the gamma rays from the decay of ^{96}Pd and ^{94}Pd events. Figure 4.12 shows the number of ions implanted in each AIDA layer when detected in coincidence with 1415 keV and 1092 keV gamma ray.

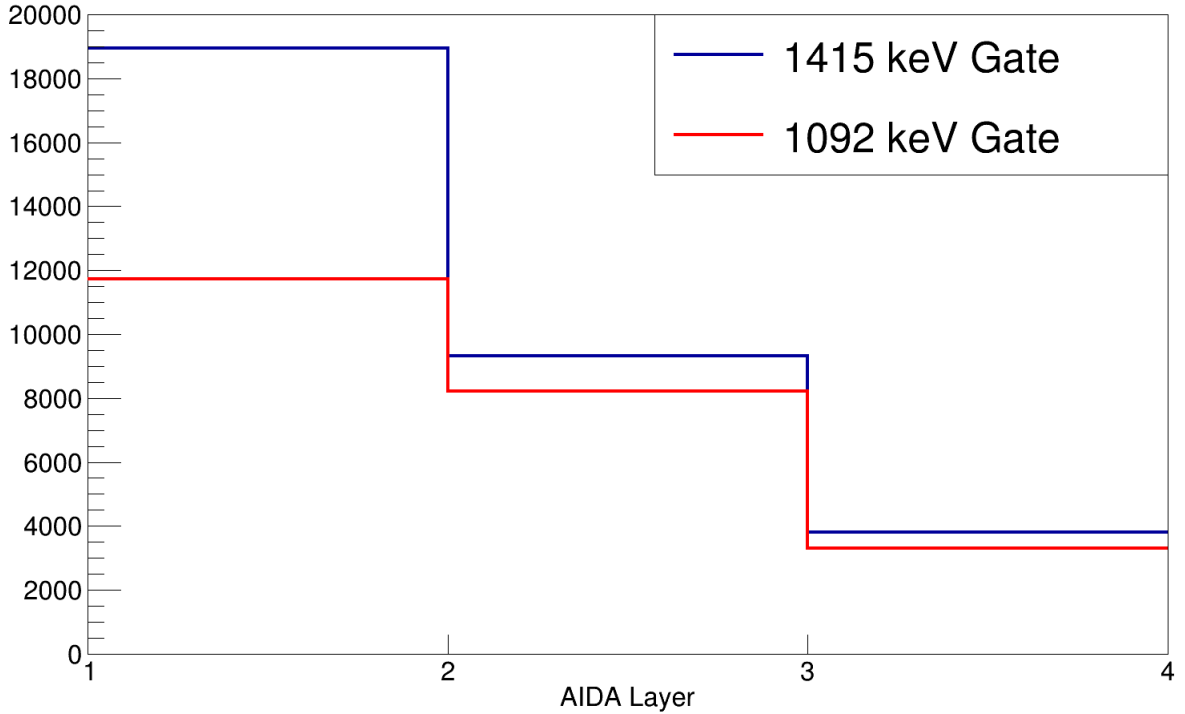


FIGURE 4.12: The location of ions deposited in AIDA detected in coincidence with 1415 keV (blue) and 1092 keV (red) gamma rays from ^{96}Pd and ^{94}Pd ions, detected in FATIMA.

4.3 Gamma-ray Analysis

4.3.1 Previously Reported Isomeric States

Due to the nature of S480 being the commissioning experiment of the DESPEC set-up it was vital that the subject matter partially focussed on isomeric states which were previously reported and identifiable to validate the efficacy of the spectroscopic detectors. While the original focus of this work was on the isomeric states of ^{96}Pd and ^{94}Pd an opportunity arose in the form ^{94}Ru which was also produced in the fragmentation process with a large enough yield reaching the S4 focal plane detectors to conduct analysis on. Figures 4.13 and 4.14 show the gamma rays seen when gating on the Z vs A/Q of ions ^{96}Pd and ^{94}Pd from 40 ns to 400 ns after the prompt flash. Figure 4.13 is also gated on the SC41 and SC42 scintillators, the β Plastic detector along with an AIDA 'stopped' condition while the ^{94}Pd spectra is solely tagged on the SC41/SC42 energy loss condition.

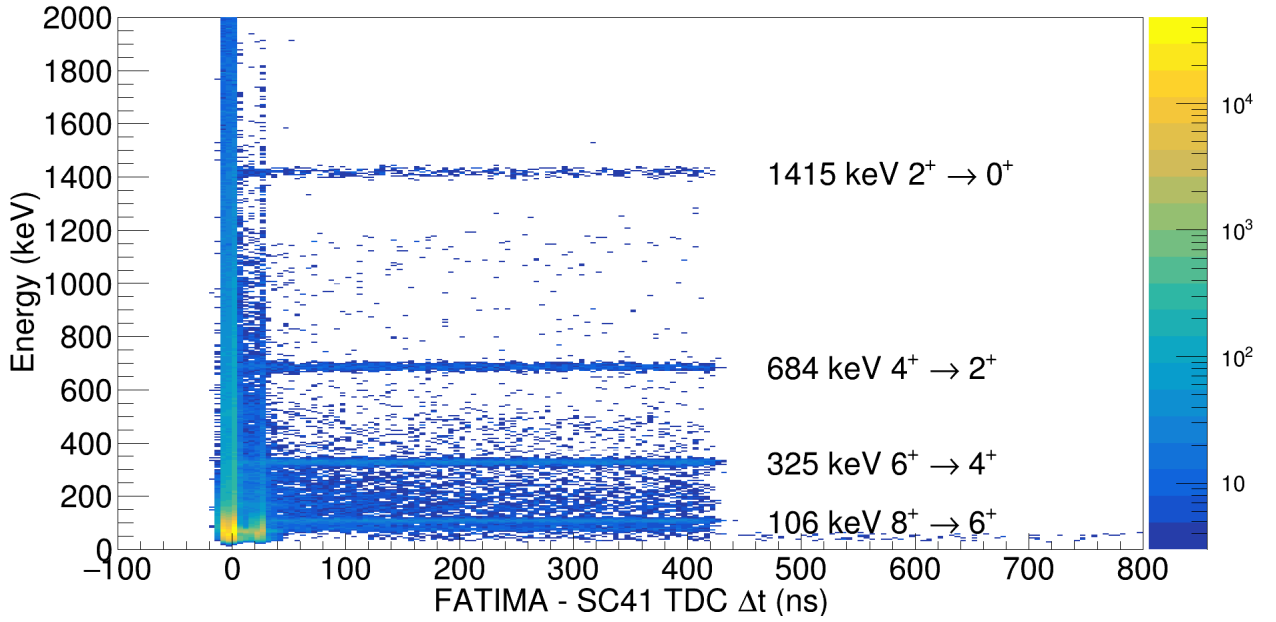


FIGURE 4.13: The γ -ray energy versus detected by FATIMA versus FATIMA - SC41 time difference when gating on the Z versus A/Q of ^{96}Pd ions seen in the FRS. Additional gating conditions are also applied on energy deposited in scintillators 41 and 42, the β -Plastic Time over Threshold (ToT) and the 'stopped' tag in AIDA

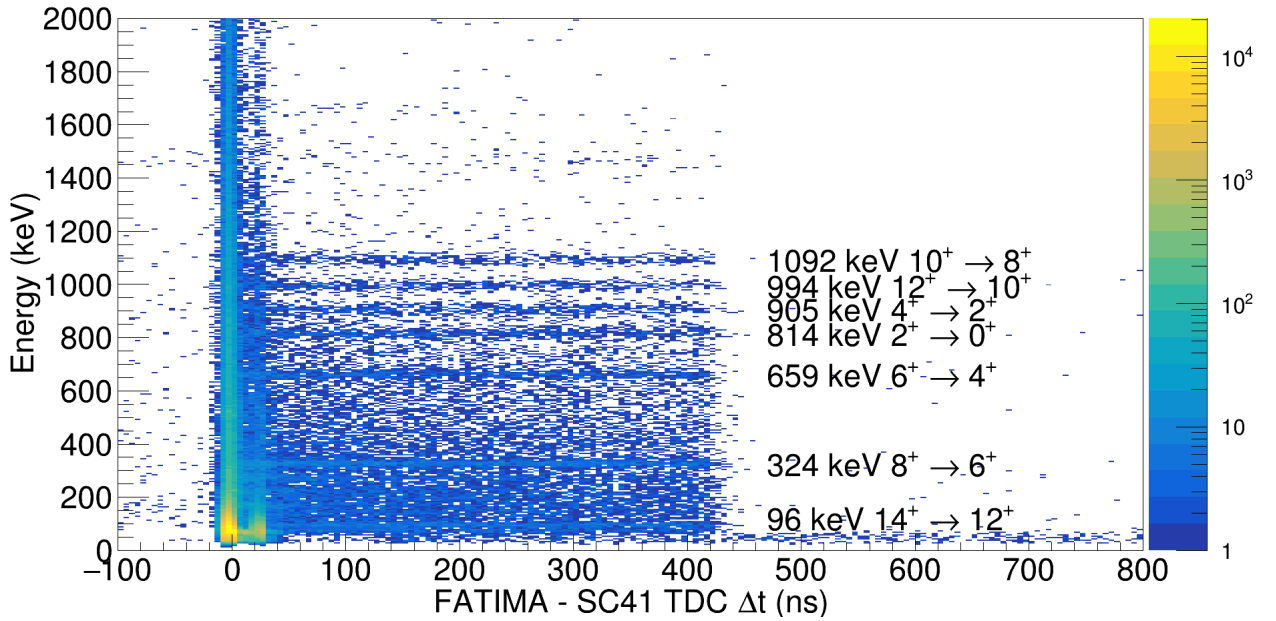


FIGURE 4.14: The γ -ray energy versus detected by FATIMA versus FATIMA - SC41 time difference. These events are gated on the Z vs A/Q of ^{94}Pd ions seen in the FRS and the energy deposited in scintillators 41 and 42.

These decisions were made due to the relative difference in the number of ^{96}Pd and ^{94}Pd ions (~ 10 million vs ~ 1 million) as well as the large drop in coincidence

efficiency when gating on the AIDA active stopper. The effects of the different gating combinations on the observed gamma rays of ^{96}Pd and ^{94}Pd can be seen in figures 4.15 and 4.16 for the FATIMA array.

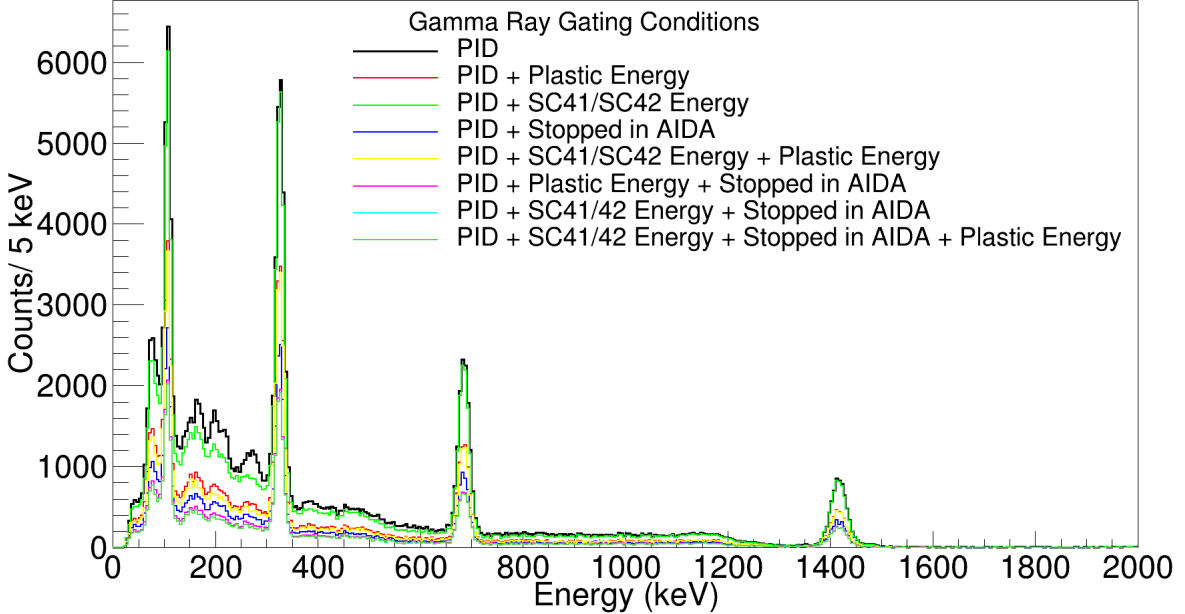


FIGURE 4.15: The different ^{96}Pd γ -ray spectra from isomeric cascades when gating on the different particle detectors in the DESPEC set-up.

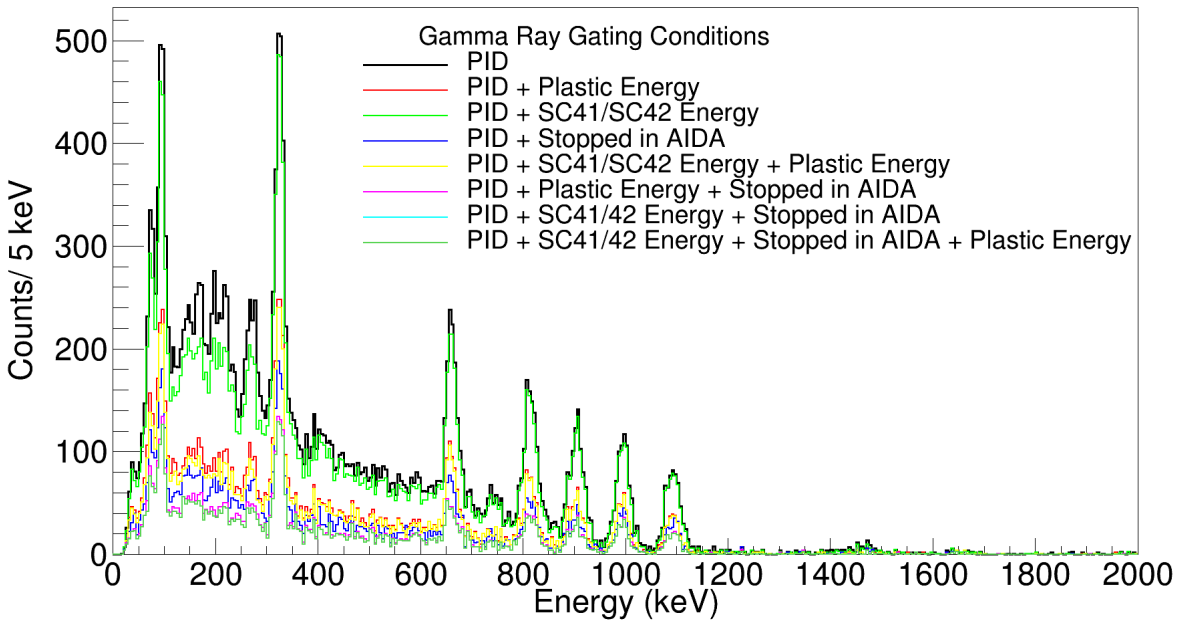


FIGURE 4.16: The different ^{94}Pd γ -ray spectra from isomeric cascades when gating on the different particle detectors in the DESPEC set-up.

Figures 4.17 and 4.18 show the energy vs time after implantation matrices for FRS and SC41/42 energy gated coincident gamma rays for ^{96}Pd and ^{94}Pd ions respectively. Figures 4.13 and 4.17 both clearly highlight the discrete energy transitions of 106 keV, 325 keV, 684 keV and 1415 keV which make up the isomeric cascade below the long lived 8^+ state. In the case of experiment S480 the FATIMA timing range was limited to 450 ns after implantation but the GTC detectors have a much larger range which allows the isomeric decay to be observed more clearly. The cascade below the relatively shorter lived 14^+ isomeric state in ^{94}Pd can also be identified in figures 4.14 and 4.18 where the decays can be seen as having almost fully decayed by ~ 2500 ns past prompt implantation.

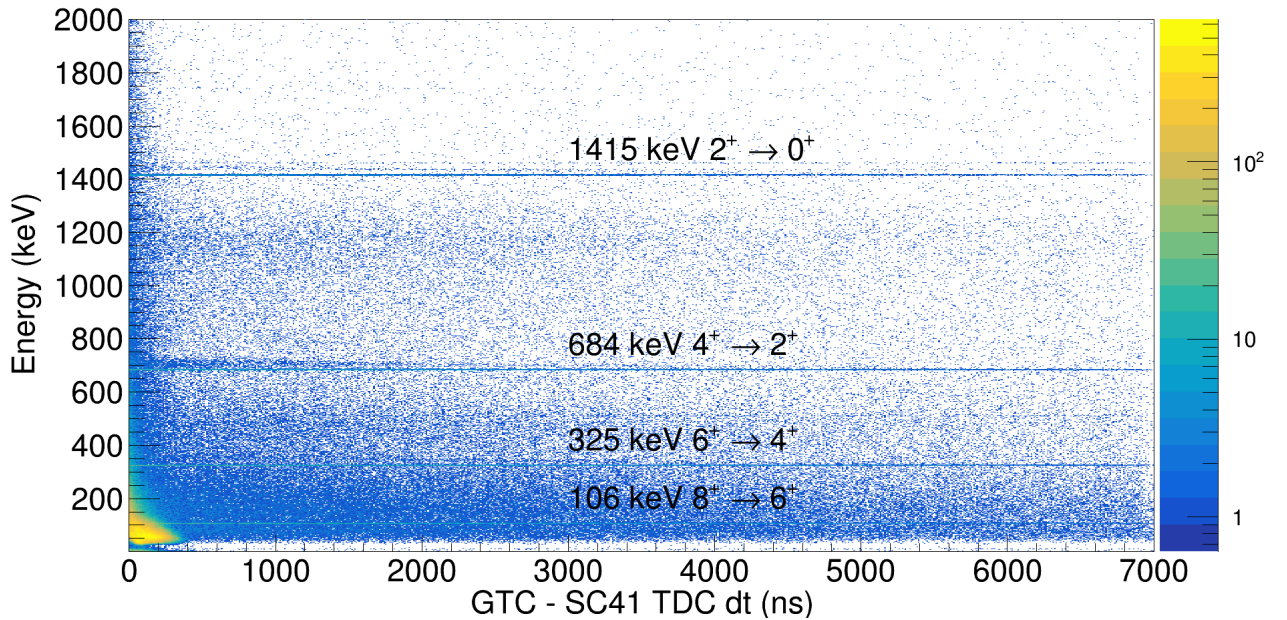


FIGURE 4.17: The γ -ray energy vs time difference with respect to scintillator 41 matrix measured by the GTC array when gating on ^{96}Pd detected in the FRS.

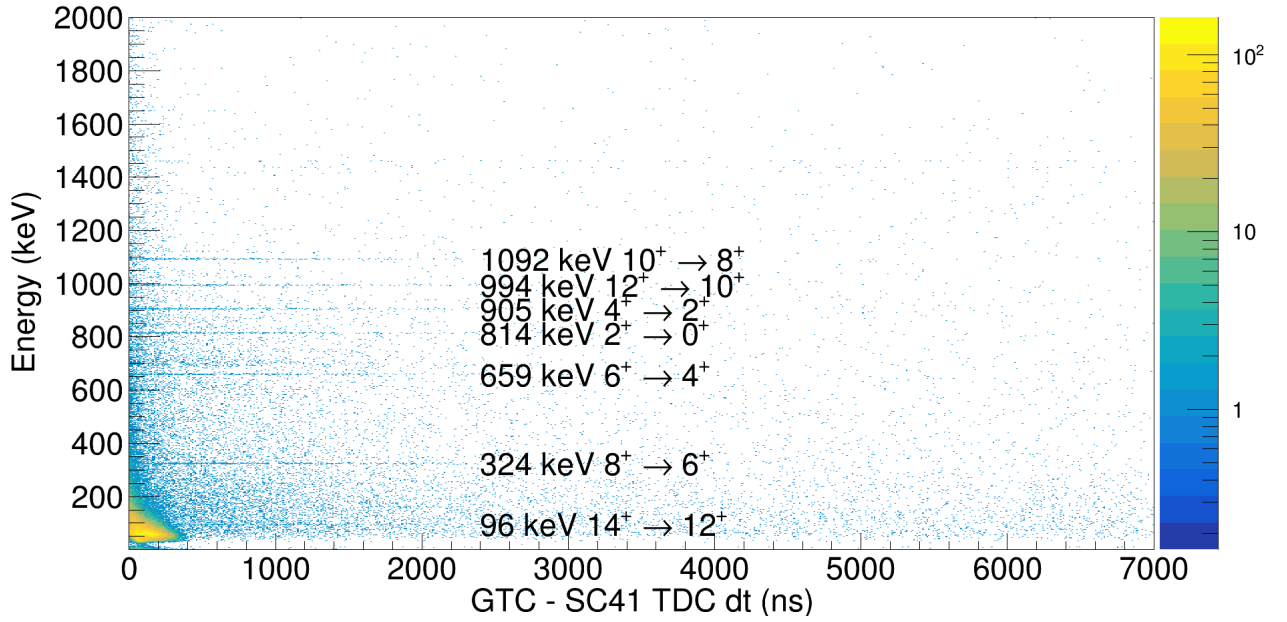


FIGURE 4.18: The γ -ray energy vs time difference matrix measured by the GTC array when gating on ^{94}Pd detected in the FRS.

In order to identify the tens of microsecond half-life isomer in ^{94}Ru another analysis technique was required to extend past the timing regime of the FATIMA and GTC arrays. This extended timing range used for the identification of the ^{94}Ru isomer was accessed by calculating the time difference between the White Rabbit timing signals of the FRS detectors and FATIMA detectors across different event windows. Figure 4.19 shows the energy vs White Rabbit time difference over this extended time range where the decays from the isomer cascading towards the ground state are highlighted.

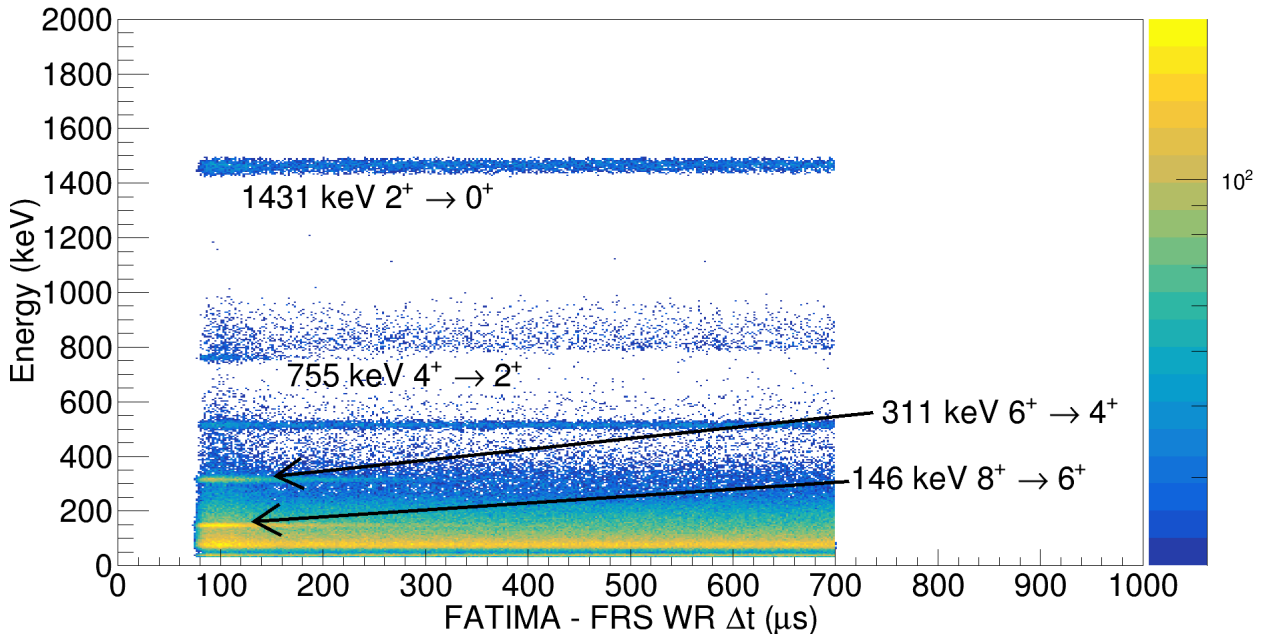


FIGURE 4.19: The FATIMA energy versus White Rabbit time difference with respect to the FRS for ^{94}Ru events. The 1431 keV transition partially overlaps with the activity associated with the internal decay in ^{138}La .

4.3.2 Isomer Half-life Measurements

Figure 4.20 shows the expected gamma rays in ^{96}Pd and the inset shows the sum of the timing data from the 1415 keV, 684 keV and 325 keV gamma rays which were binned likelihood fit to an exponential decay giving a value of $T_{\frac{1}{2}} = 1.84(2)$ μs which has a relatively strong agreement with work done by Hafner et al. [12] and Mach et al. [44]. Figure 4.20 b) shows the expected gamma rays and timing response for the ^{94}Pd gamma rays, specifically the 1092 keV, 994 keV, 905 keV, 814 keV, 659 keV and 324 keV gamma rays. The summed timing data from these points when fit to an exponential decay using a binned likelihood fit to give a value of $T_{\frac{1}{2}} = 499(9)$ ns which also give a strong agreement to work done by Hafner et al [12].

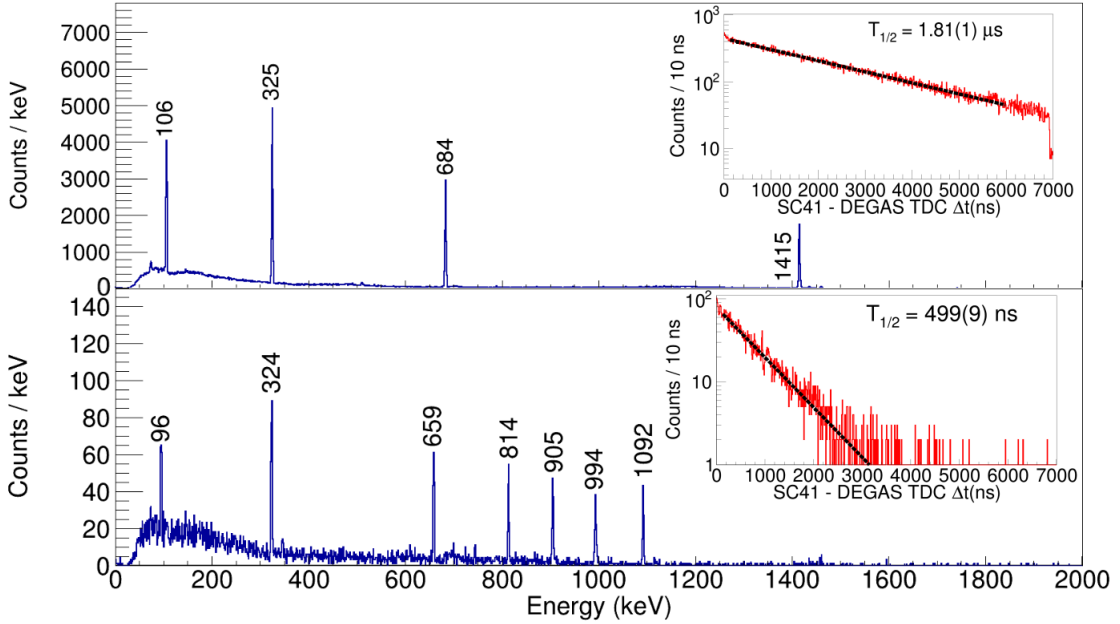


FIGURE 4.20: Gamma ray singles projections for ^{96}Pd (above) and ^{94}Pd (below) showing the energy cascades below the isomeric 8^+ and 14^+ states respectively. The decay curves seen in the insets were created by summing the background subtracted time projections of each individual transition (not including those below 200 keV) which was detected between 0 μs - 8 μs and fitting them with a single component exponential over a time range of 0.1 - 6.0 μs .

In the case of ^{94}Ru a normalised background subtraction was carried out between the decay region of 80 μs - 350 μs and the background region of 350 μs - 620 μs . The result of the background subtraction process can be seen in figures 4.21 which were generated by taking energy projections from figure 4.19. 4.21 a) shows the gamma rays detected within 80 μs - 350 μs after the implantation of the 8^+ isomer and displays the expected gamma rays along with lead X-rays at 90 keV, the pair production peak at 511 keV and the 1460 keV ^{40}K room background. Figure 4.21 b) shows a projection of the region 350 μs - 620 μs after implantation and one can clearly see the prominent background peaks previously mentioned. Figure 4.21 c) shows the subtraction of figure b) from figure a) which eliminates the background peaks and compton continuum seen in a) while increasing the peak to background ratio of the relevant gamma rays at 146 keV, 311 keV, 755 keV and 1431 keV.

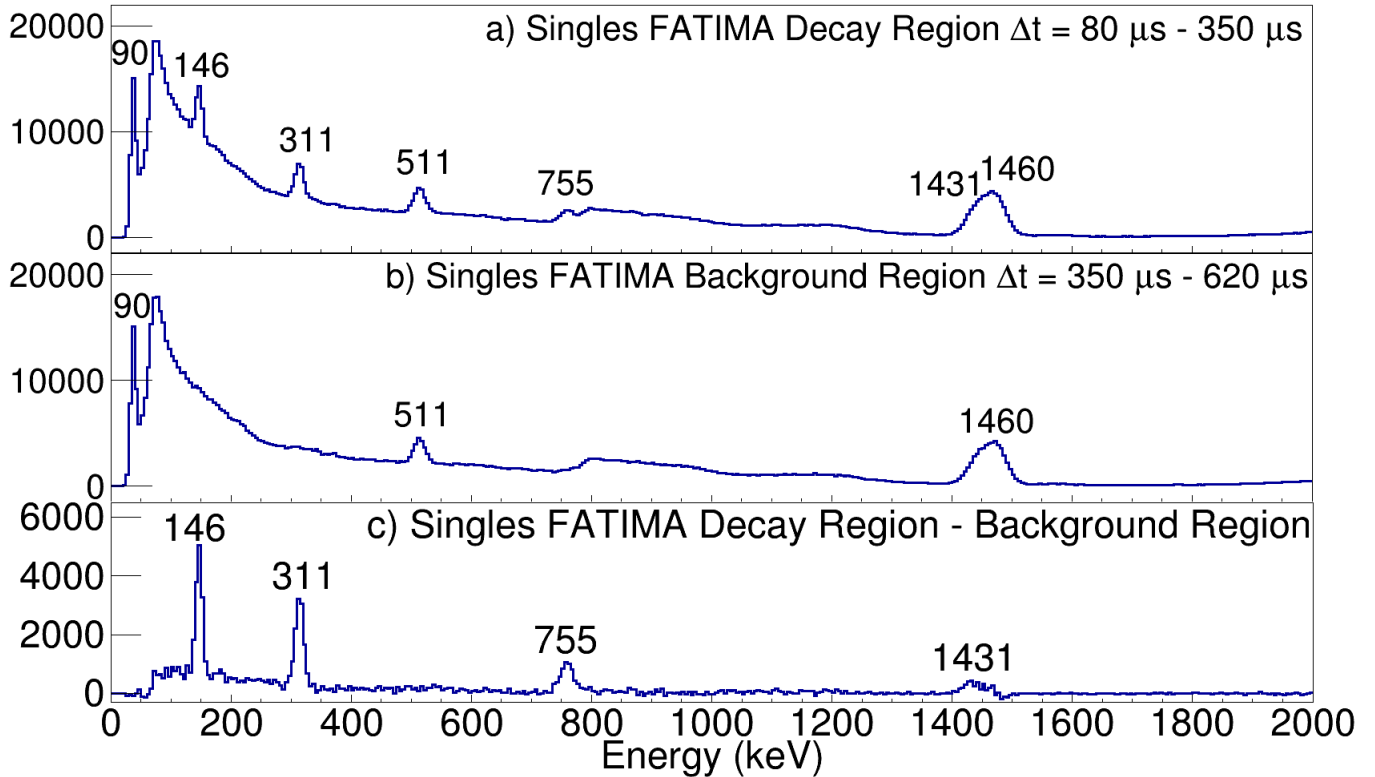


FIGURE 4.21: Gamma rays detected following the decay of the 8^+ isomeric state in ^{94}Ru within the White Rabbit timing range of a) the decay region of $80 \mu\text{s}$ to $350 \mu\text{s}$, b) the background region $350 \mu\text{s}$ to $620 \mu\text{s}$ and c) spectra b subtracted from spectra a to form a normalised background subtracted spectra.

In each of these cases it is worth noting that timing information from gamma rays exclusively above 150 keV were used due to the relatively high levels of background below this energy. By observing the timing data of the 1431 keV, 756 keV and 311 keV transitions in ^{94}Ru it was possible to extract a half-life value for the isomeric 8^+ state by fitting the timing data to an exponential decay curve with a linear background using a binned likelihood fit, as seen in figure 4.22. The value of the half-life was measured as $T_{\frac{1}{2}} = 64(1) \mu\text{s}$ which was also in agreement with previous works [12][44].

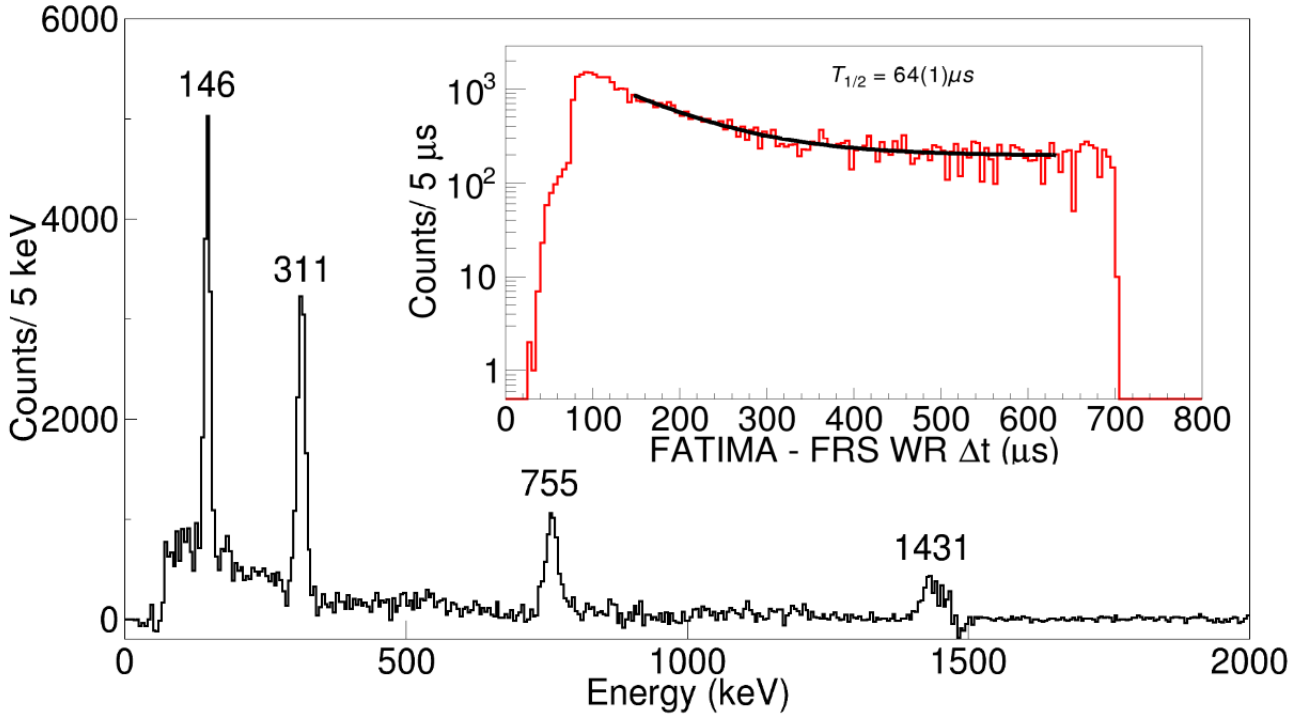


FIGURE 4.22: A singles γ -ray spectrum of the ^{94}Ru isomeric cascade generated from the extended timing window of the FATIMA - FRS White Rabbit time differences over the range of $80\ \mu\text{s}$ - $350\ \mu\text{s}$. A background subtraction has been carried out whereby the region from $350\ \mu\text{s}$ - $620\ \mu\text{s}$ was taken away to minimise the impact of background peaks. The inset shows a combination of background subtracted timing projections on the $146\ \text{keV}$, $311\ \text{keV}$, $755\ \text{keV}$ and $1431\ \text{keV}$ γ -ray transitions in ^{94}Ru with an exponential plus linear background fit over a range of $150\ \mu\text{s}$ - $650\ \mu\text{s}$.

4.3.3 Determination of FATIMA Full Energy Peak Detection Efficiency

In order to calculate the isomeric ratio of a given nuclei it is required to know the efficiency of the array. This is often done through source measurements taken before an experiment but in the case of S480 an internal check of the efficiency was performed. The ^{96}Pd decay data provided an avenue for this due to the FATIMA array's ability to discern time differences at the hundreds of ps scale allowing for the generation of $\gamma - \gamma$ matrices with stringent timing restrictions. By calculating the ratio between the number of counts of a given energy in the singles spectra to the number of counts observed at the same energy when gating on a coincident gamma-ray transition one will have calculated the singles efficiency of the array at the gated transition's energy. The formula used for this is defined in 4.1 [95].

$$\epsilon_{Singles} = \frac{Counts_{\gamma\gamma}}{Counts_{Singles}} \quad (4.1)$$

Where $\epsilon_{Singles}$ is the singles efficiency, at a particular energy where a $\gamma - \gamma$ coincidence gate is set, $Counts_{\gamma\gamma}$ is the number of counts in the gamma-gated spectra at a particular energy, and $Counts_{Singles}$ is the number of counts of that energy in the singles spectra. These values when divided by one another will give the efficiency of the array at the gated energy. This can be done with all coincident gamma rays and a weighted mean can be calculated for these values giving a final value for the efficiency at the gate energy. The weighted mean can be calculated using equation 4.2

$$W = \frac{\sum_{i=1}^n w_i X_i}{Counts_{Singles}} \quad (4.2)$$

Where n is the number of data points, X is the value of the i^{th} data point and w is the weighting of the i^{th} data point equivalent to the reciprocal of its uncertainty.

Figure 4.23 a) shows the ^{96}Pd Z vs A/Q, SC41-SC42 energy deposition, β -Plastic ToT and AIDA 'stopped' tag gated and singles gamma rays detected 40 ns to 400 ns after prompt implantation. Figure 4.23 b) shows the total projection of the $\gamma - \gamma$ coincidence matrix with the same stated gating conditions while c) - f) show the gamma rays detected in coincidence with the 106 keV, 325 keV, 684 keV and 1415 keV transitions.

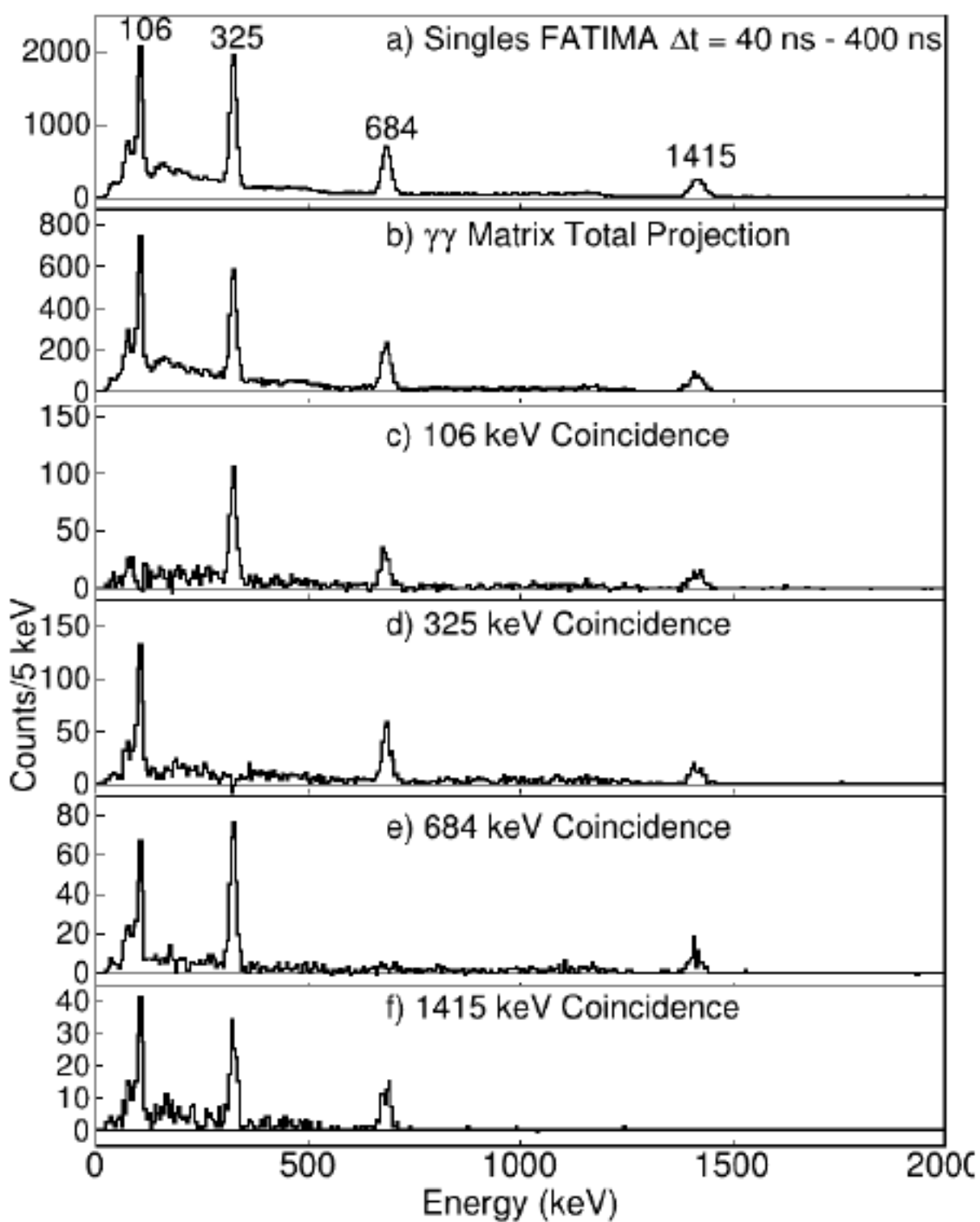


FIGURE 4.23: A set of gamma-ray spectra showing a) the singles FATIMA spectra projected on events detected 40 ns - 400 ns after the prompt flash, b) the total projection of a $\gamma - \gamma$ matrix sorted with a condition that two gamma rays had to arrive at FATIMA detectors within 40 ns of each other and c) through to f) showing the various coincidence gated projections of the $\gamma - \gamma$ matrix.

The efficiency of FATIMA at the transition energies in ^{96}Pd were calculated giving multiple data points at each energy using equation 4.1 and the weighted means at each energy were calculated using equation 4.2. These results are summarised below in figure 4.24.

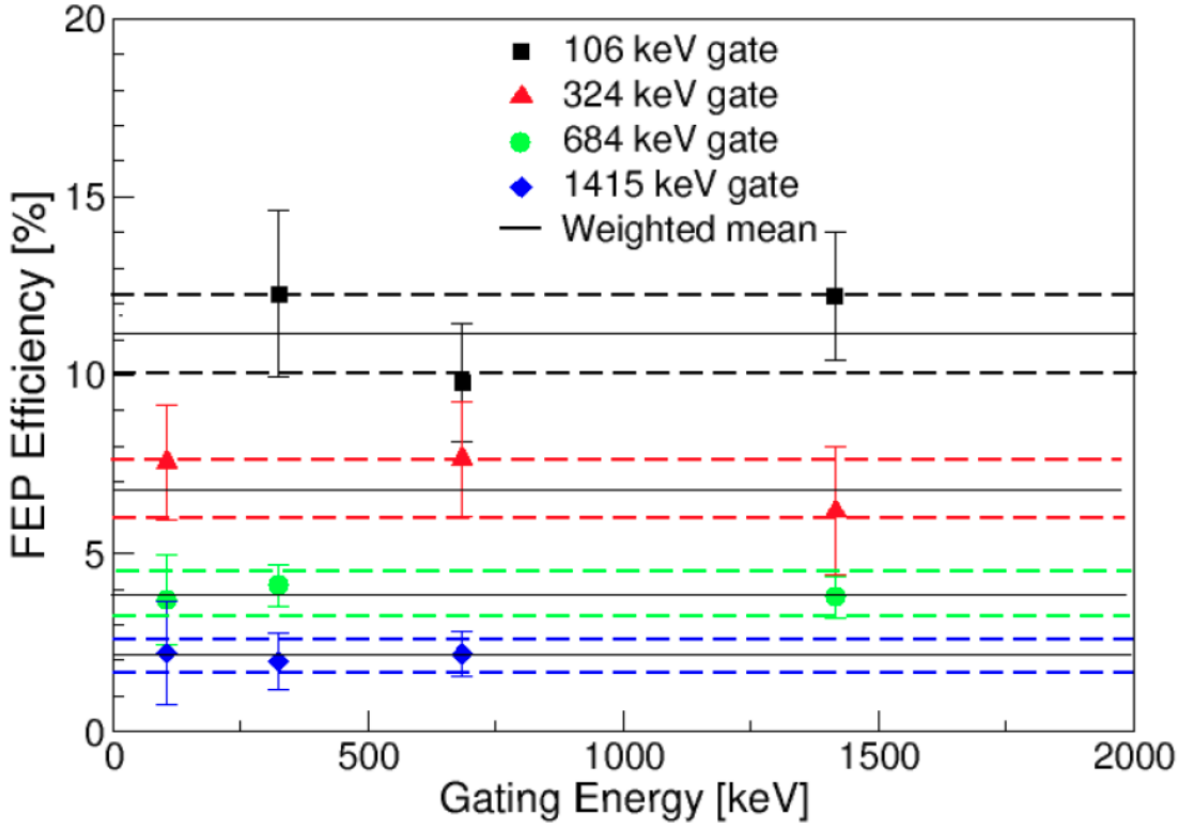


FIGURE 4.24: Weighted mean values for the calculated γ -ray full-energy peak efficiencies for the 106 keV, 325 keV, 684 keV and 1415 keV transitions associated with the decay of the isomeric 8^+ state. The dashed line represent the uncertainties in the weighted mean averages for each transition.

The full energy peak efficiencies of the FATIMA array were calculated to be 11.2(11)% at 106 keV 6.8(7)% at 325 keV 3.8(6)% at 684 keV and 2.1(5)% at 1415 keV.

4.3.4 Calculation of Isomeric Ratios

The isomeric ratio of an nucleus is the ratio of which an isomeric state is produced in a given nucleus and is defined in equation 4.3 [68–71, 96].

$$R = \frac{N_{Isomer}}{FGN_{Ions}} \quad (4.3)$$

N_{Ions} is the number of ions produced from the reaction mechanism, N_{Isomer} is equal to the number of ions produced in the isomeric state and is determined using equation 4.4.

$$N_{Isomer} = \frac{N_{\gamma i}}{\epsilon_{\gamma}} \frac{(1 + \alpha_i)}{b_{\gamma i}} \quad (4.4)$$

Where $N_{\gamma i}$ is the number of gamma rays observed of the i^{th} decay branch below the isomeric state, ϵ_{γ} is the detection efficiency of the gamma-ray array at the energy of the transition, $\alpha_{\gamma i}$ is the internal conversion coefficient for that transition and b_{γ} is the branching ratio of the transition. F is a correction factor for losses in the time of flight of the ions through the separator which is calculated using equation 4.5.

$$F = \exp^{-(\lambda_1 t_1 + \lambda_2 t_2)} \quad (4.5)$$

Where λ_1 and λ_2 correspond to the different decay constants depending on the charge state of the ions and t_1 and t_2 are the times of flight spent in that decay mode. The ions are fully stripped while travelling through the separator which means λ_1 must account for the lack of internal conversion in the decay time t_1 with λ_2 including internal conversion. G is a second correction factor which is used to account for the finite measurement time window and can be calculated using equation 4.6.

$$G = \exp^{-\lambda t_i} - \exp^{-\lambda t_f} \quad (4.6)$$

Where t_i and t_f are the initial start and finish times of the measurement after the production of the ions.

Figure 4.25 shows the exponential decay regimes of the isomeric states in ^{96}Pd and ^{94}Pd through the separator and after implantation align with the timing window which FATIMA had access to.

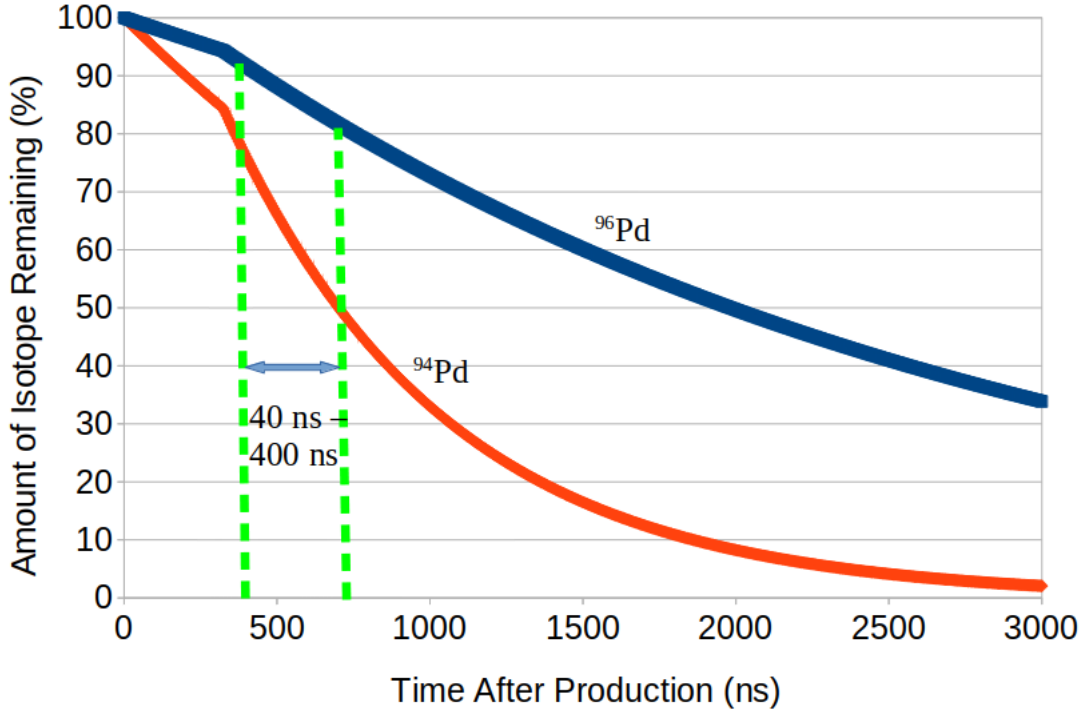


FIGURE 4.25: The decays of the ^{96}Pd and ^{94}Pd isomers through the separator. The dashed lines represent the timing window which FATIMA was used to measure decays. A clear change in the decay regimes can be seen to occur for both nuclei at 325 ns which is the time of flight through the separator. The neutral atom half-life used in equation 4.5 for the 8^+ state in ^{96}Pd is equal to 1.81(1) μs while the fully stripped ion has a half-life of 3.86(2) μs . Similarly the 14^+ state in ^{94}Pd has a half-life of 499(9) ns as a neutral ion and 1.32(3) μs when fully stripped. These increased half-lives are associated with the internal conversion coefficients from the 106 keV and 96 keV E2 transitions from these states in ^{96}Pd and ^{94}Pd respectively.

the time of flight from production to the stopper (350 ns?) ; the neutral atom isomer half-lives used for the 8^+ decay in ^{96}Pd ($I_p=8^+$; $T_{1/2}=1.8 \mu\text{s}$) and ^{94}Pd ($I_p=14^+$; $T_{1/2}=499 \text{ ns}$) and the inflight-fully-stripped half-lives for these same isomers as used in this calculation from the increased half-lives associated with the internal conversion coefficients for 106 and 96 keV E2 transitions in Palladium respectively.

The increase in decay rate seen at 325 ns coincides with the time of flight of the beam through the separator after which the ions may start gathering electrons, opening the previously closed internal conversion decay channel and in turn decreasing the half-life of the state. Before calculating the isomeric ratio, one must account for any branches in the decay schemes of the isotopes. In the case of ^{96}Pd the decay is 100% fed $8^+ \rightarrow 6^+ \rightarrow 4^+ \rightarrow 0^+$. By using values for α_i calculated from literature [53] along with the knowledge that the transitions below ^{96}Pd are 100% fed with a slight branch in ^{94}Pd (90-10). Upon discerning this one is then able to use 4.4 to calculate a value for N_{Isomer} . Finally, the corrections in F and G can be calculated and combined using equation 4.3 to calculate an isomeric ratio value for each transition below the isomer. A weighting factor

can then be calculated for each transition by taking the reciprocal of the uncertainty and the weighted mean of the calculated isomeric ratios can be combined into a final value using equation 4.2. $N_{\gamma i}$ was measured by fitting the peaks in figure 4.25. It is worth noting that figure 4.25c) has undergone the background subtraction described in section 4.3.2 which results in a slight over-subtraction of the 1461 keV and 1435 keV background peaks from ^{40}K and ^{138}La respectively while figures a) and b) have had no background subtraction applied to them.

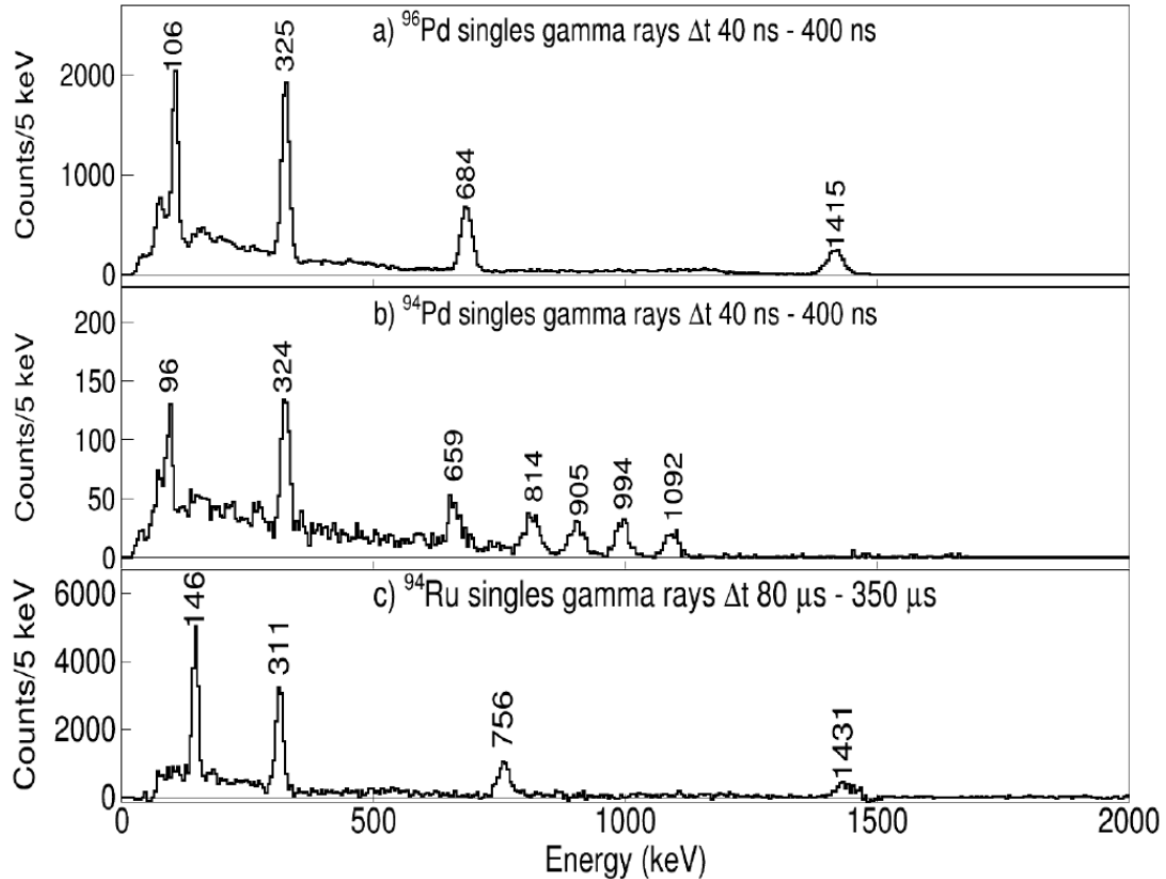


FIGURE 4.26: The singles γ rays detected in FATIMA gated on the different ion species seen in the FRS projected across the time ranges.

A collection of the isomeric ratios calculated for each energy used to obtain the final isomeric ratio values for $^{96,94}\text{Pd}$ and ^{94}Ru can be seen in figure 4.27.

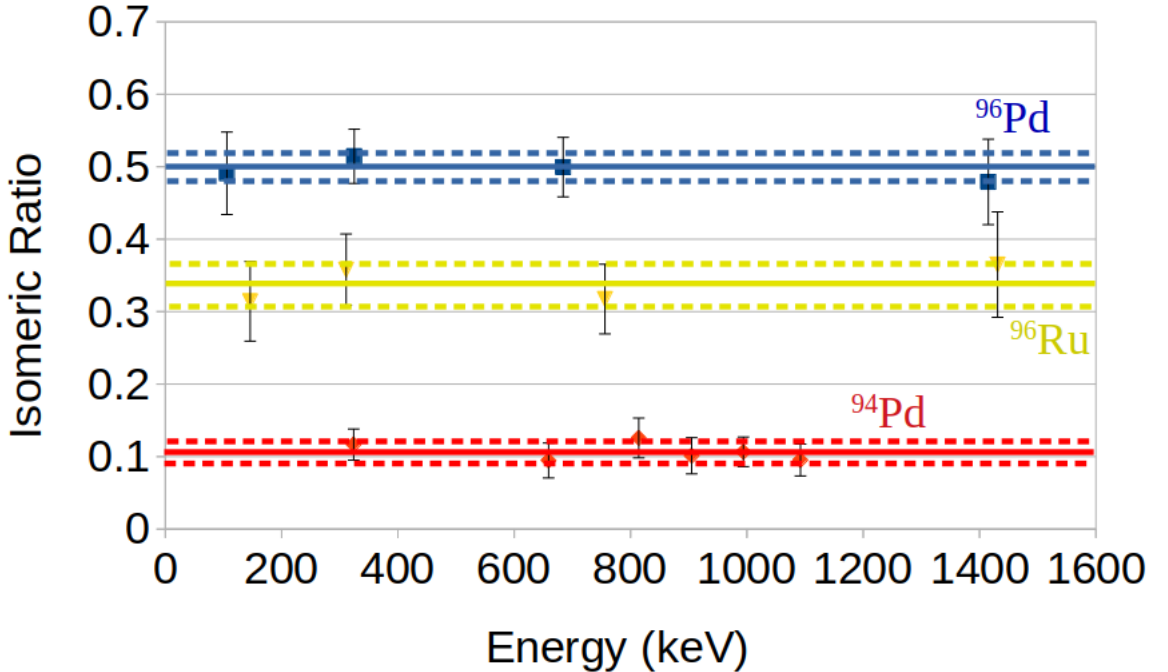


FIGURE 4.27: The isomeric ratios of the isomeric states in ^{96}Pd , ^{94}Pd and ^{94}Ru . Each data point was calculated using a different energy transition and were combined using weighted means to determine a final value. The solid lines correspond to the final value of the isomeric ratio for each nuclei and the dashed lines show the margin of error.

A summary of the measured isomeric ratios and half-lives of the isomeric states in ^{96}Pd , ^{94}Pd and ^{94}Ru are listed in table 4.1.

Ion	I^π	$T_{\frac{1}{2}}$	α	R	Lit. R [12]
^{96}Pd	8^+	$1.81(1) \mu\text{s}$	$1.134(16)$	$50(2)\%$	$51(6)$
^{94}Pd	14^+	$499(9) \text{ ns}$	$1.62(2)$	$11(1)\%$	$15(2)$
^{94}Ru	8^+	$64(1) \mu\text{s}$	$0.334(5)$	$34(3)\%$	$53(6)$

TABLE 4.1: A summary of the measured half-lives and isomeric ratios of ^{96}Pd , ^{94}Pd and ^{94}Ru .

4.4 DESPEC NPTool Simulation

As the first experiment in the DESPEC campaign S480 was an excellent opportunity to validate a novel Monte Carlo GEANT4/NPTool [97, 98] simulation. Monte Carlo simulations refer to a form of computational experiment which relies on rigorous random sampling to obtain a numerical result. This method is very suitable for use when modelling radiation detectors due to the random nature of radioactive decay along with the multiple probabilistic ways in which radiation can interact with matter. By running

experiments with enough statistics one can learn a lot about the different ways in which radiations of interest may interact with the different parts of an experimental setup, allowing for potential oversights such as excess shielding or insufficient detector efficiency to be addressed early on. While this work will only focus on the FATIMA response the simulation contains geometries representing all of the DESPEC subsystems including the AIDA active stopper, the β -Plastic scintillation detector, the GTC array as well as scintillator SC41 and 42. Figure 4.28 shows the NPTool geometry of the simulation discussed in this section [99].

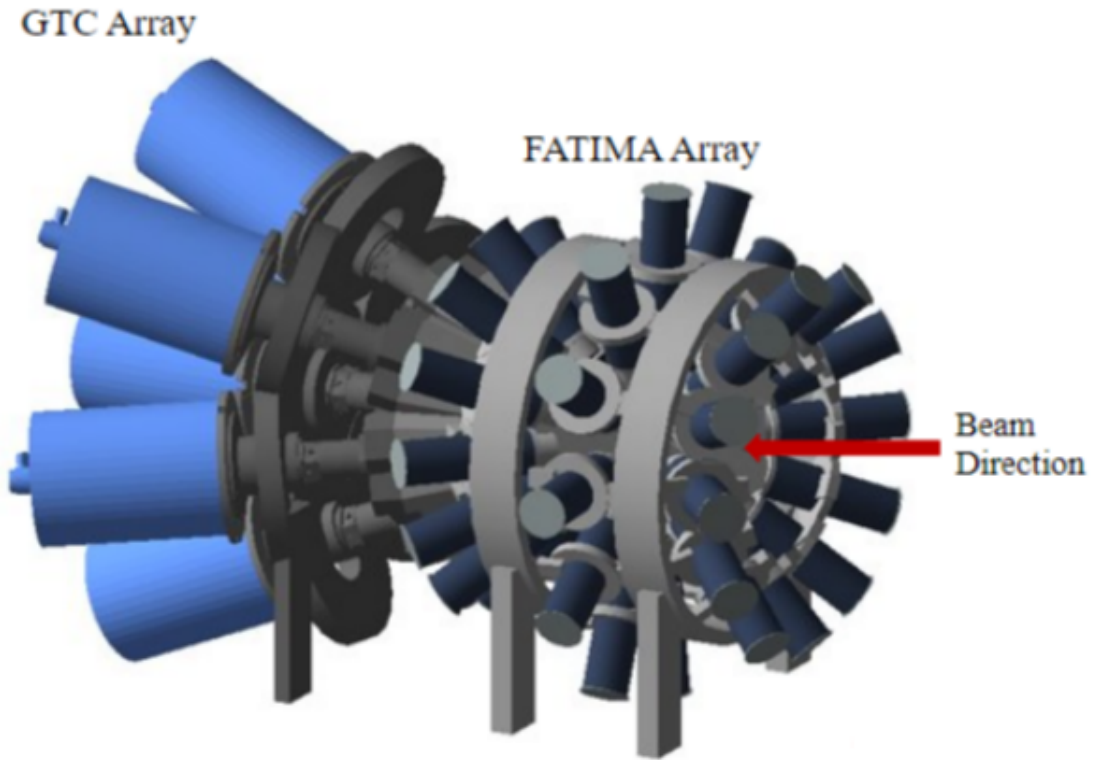


FIGURE 4.28: The GEANT4/NPTool simulation representation of the DESPEC set-up featuring the 36 FATIMA detectors.

This project was developed with the goal of reproducing the response of the FATIMA array to provide additional insight when planning future experiments. This simulation was validated using a direct comparison of the efficiency response seen in figure 4.23 with the measured singles to doubles efficiency ratio using data points from a simulated mixed source. The simulated response of FATIMA was shown in figure 4.29 for 10^6 simulated decays of the 8^+ isomer in ^{96}Pd .

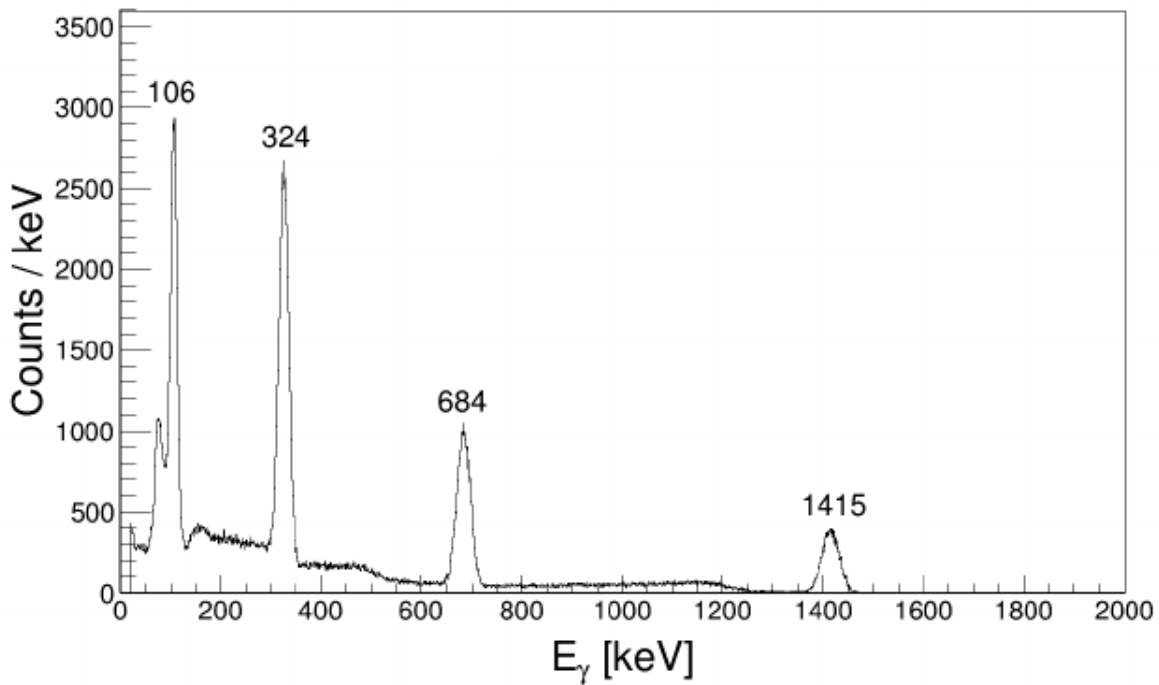


FIGURE 4.29: A GEANT4 simulated spectra for FATIMA run with 10^6 simulated events. The simulation emulates the $I^\pi = 8^+$ isomeric cascade in ^{96}Pd for a source placed in the centre of the array with the DESPEC configuration.

Data points for the simulated efficiency were determined by simulating 10^6 decays of the following radionuclides: ^{241}Am , ^{109}Cd , ^{57}Co , ^{139}Ce , ^{51}Cr , ^{83}Sr , ^{137}Cs , ^{54}Mn , ^{88}Y , ^{65}Zn and ^{60}Co which compose the NPL mixed gamma-ray source with energies ranging from 59.5 keV to 1836 keV which provided enough statistics for each source to keep statistical uncertainties low. The response for these simulations are shown in figure 4.30.

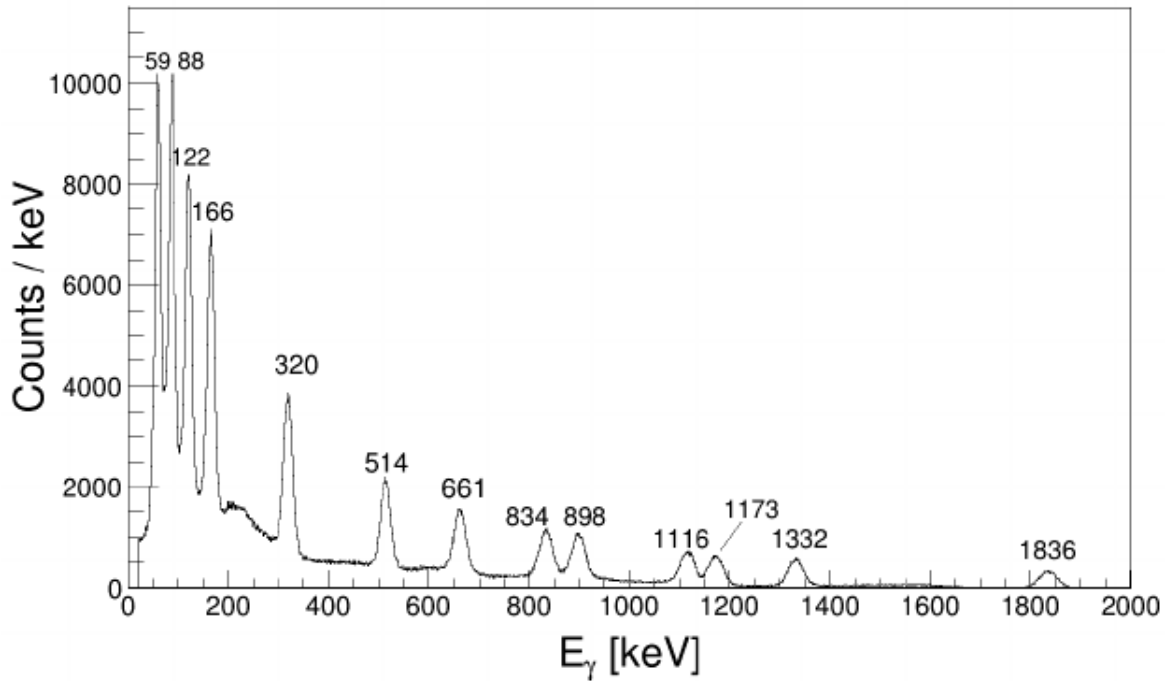


FIGURE 4.30: A GEANT4 simulated spectra displaying the FATIMA response for 10^6 decays of ^{241}Am , ^{109}Cd , ^{57}Co , ^{139}Ce , ^{51}Cr , ^{83}Sr , ^{137}Cs , ^{54}Mn , ^{88}Y , ^{65}Zn and ^{60}Co .

The efficiency of the simulated response can be easily calculated as a ratio between the number of events in the photo-peak and the number of simulated events. A comparison between the simulated efficiencies and that of the experimental set-up can be seen in figure 4.31.

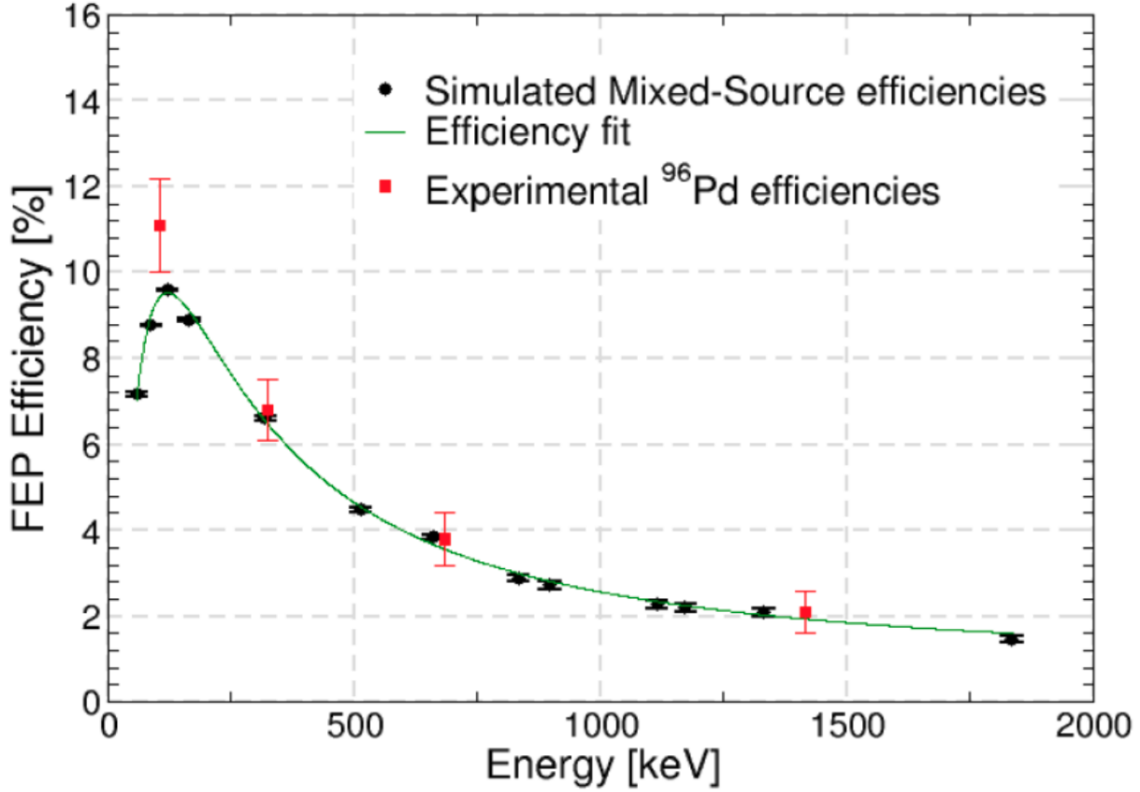


FIGURE 4.31: A comparison between the full energy peak efficiencies measured in experiment S480 and those simulated through the mixed γ -ray source.

The FATIMA simulations employ a Poisson-like energy response function through the use of a random Gaussian smearing of the instrumental energy response [100]. The random Gaussian smearing was performed using the measured σ of FATIMA as a function of gamma-ray energy using the transitions in the isomeric cascade. This plot can be seen in figure 4.32 which was fit to $\sigma = 0.92E^{0.39}$ across the range of 106 keV to 1415 keV. With this equation one is able to "smear" a simulated gamma ray event by randomly altering the energy of the fired gamma ray by an amount dependent on σ which in turn produces a detector response more in line with what is expected for a detector in-situ.

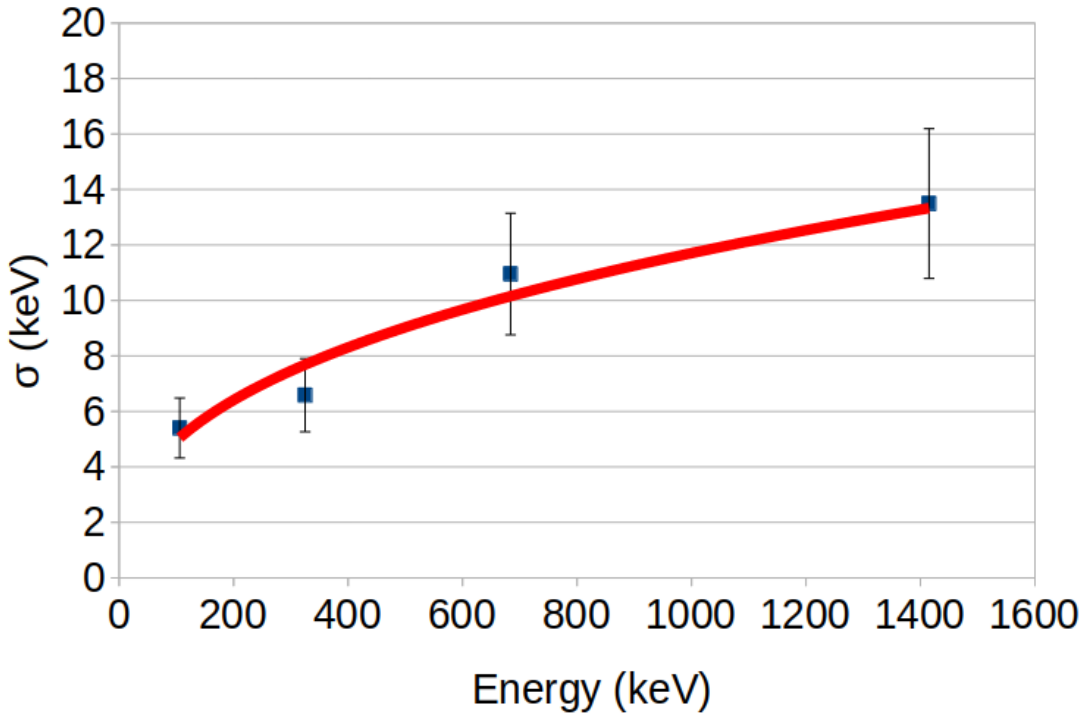


FIGURE 4.32: A measure of the value of the σ of Gaussian peaks in FATIMA vs gamma ray energy. A power law fit was used to determine the relationship $\sigma = 0.92E^{0.39}$.

In order to directly compare the simulated with with the experimental data the isomeric ratio analysis was used to determine the number of expected isomeric decays in a time period of 40 ns to 400 ns after implantation assuming a 325 ns time of flight through the FRS for the fully stripped ^{96}Pd ion. This calculation provided a value of 97,970 isomeric cascades which were simulated and compared to the experimental data gathered in the aforementioned timing range with the comparative response shown in figure 4.33.

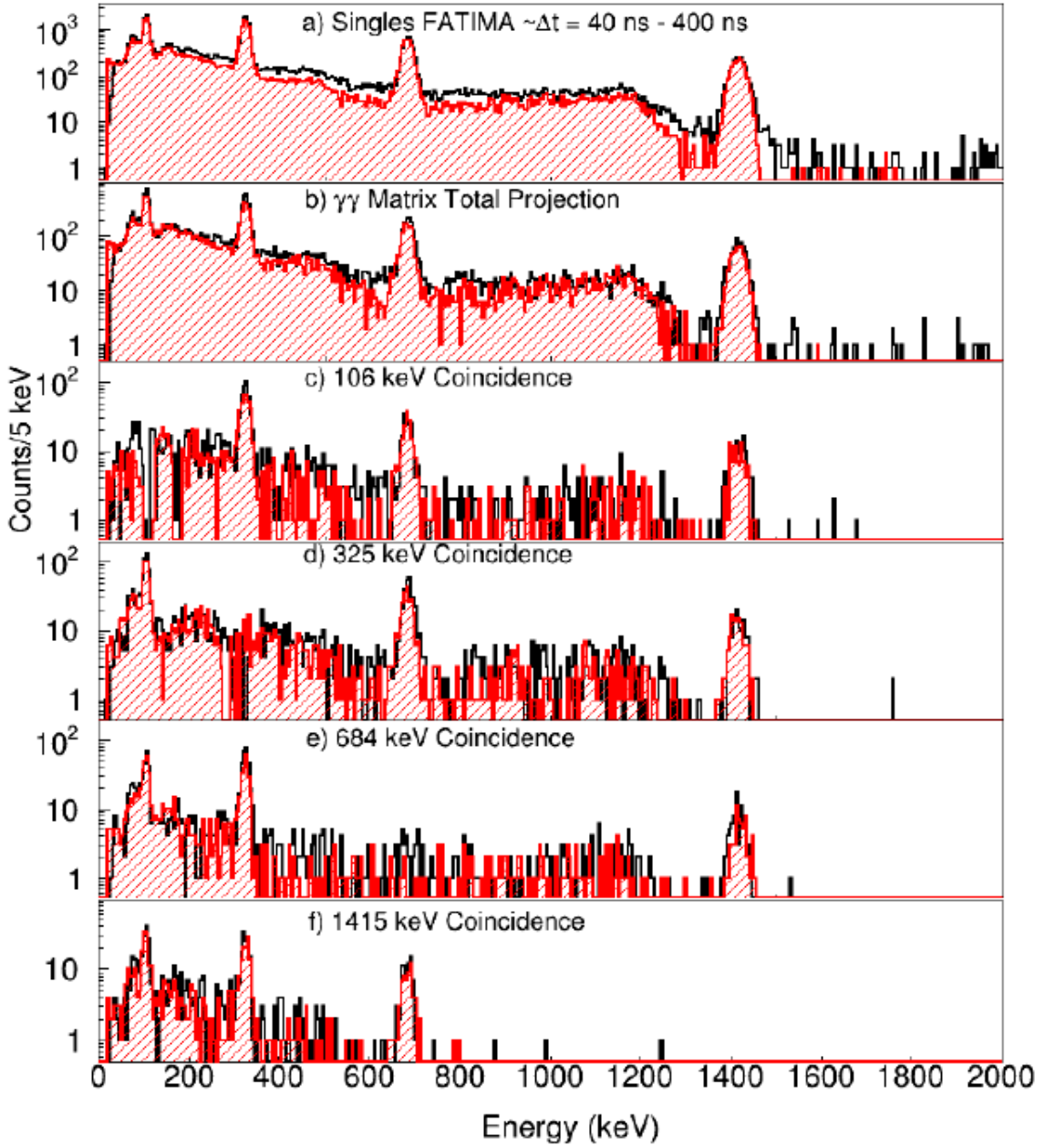


FIGURE 4.33: FATIMA spectra comparing the experimental (black) and simulated (red shaded) responses for decays of the ^{96}Pd isomer for decays between 40 and 400 ns following implantation in AIDA. The simulated spectra was generated for 97,970 isomeric cascades in this timing window. The figures show a) singles spectra and b) total projections for the coincidence matrices. c) - f) show the background subtracted coincidence spectra gated on the 106 keV, 325 keV, 684 keV and 1415 keV transitions respectively.

There is a comparatively higher level of background in the experimental data for energies greater than 325 keV. This is to be expected due to the uncontaminated nature of the simulation with the background likely being associated with the internal activity

of the LaBr₃(Ce) crystal [5]. Namely, the internal activity comes from the 789 keV gamma ray from the β^- decay branch of ¹³⁸La to ¹³⁸Ba. A second decay channel in the form of electron capture is also present with ¹³⁸La decaying into the first excited state of ¹³⁸Ce at 1435 keV seen in figures 4.33 a) and b) slightly higher in energy than the 1415 keV peak. This contamination is not as prominent in the coincidence data which requires a time difference between gamma rays of less than 40 ns.

Chapter 5

Fast Timing Measurements and Discussion

5.1 Fast Timing Results

Following the careful selection of particle identification gates it was possible to extract the final half-lives of interest by observing the time differences between pairs of gamma rays in FATIMA detectors with the addition of a time of flight correction due to travel time of the gamma rays to the detectors. This time of flight correction could only be made for the half-life measurements in ^{96}Pd due to the significant reduction in statistics when gating on pairs of particle detectors in the case of ^{94}Pd and ^{94}Ru . The correction was made by altering the timing response of the detector by accounting for the distance between the position of implantation in AIDA and the position of FATIMA detectors for gamma rays travelling at the speed of light in air. Additionally, an extra sorting condition was placed on the ^{96}Pd matrix which only accepted data from pairs of detectors on the same TDC board. This was done to remove the effect of the small chance of a 25 ns offset being present in the time differences of pairs of detectors on different TDC boards. The correction was only required for the ^{96}Pd measurements due to the half-life of the 6^+ state. These calibrated and collected data were then sorted into $E_\gamma - E_\gamma - \Delta T$ cubes with a time difference range of 100 ns. Following this, half-lives for the states of interest in ^{96}Pd , ^{94}Pd and ^{94}Ru were extracted and their $\text{B}(\text{E}2)$ values were calculated which allowed for comparisons with theoretical enhanced shell model calculations. Predictions of the $\text{B}(\text{E}2)$ values for ^{96}Pd and ^{94}Pd were made using the JUN45 and Gross-Fenkel models.

5.1.1 Transitions Populated Following the Decay of the 8^+ Isomer in ^{96}Pd

Figure 5.1 shows the gamma-ray energy versus gamma-ray timing difference between gamma rays detected in coincidence with a 1415 keV $2^+ \rightarrow 0^+$ transition in ^{96}Pd . The three different coincident transitions are labelled and clearly show a difference in the timing regimes of the half-lives of the states below the isomeric 8^+ state with the 2^+ state appearing to be promptly decayed through while the 4^+ and 6^+ states display longer half-lives.

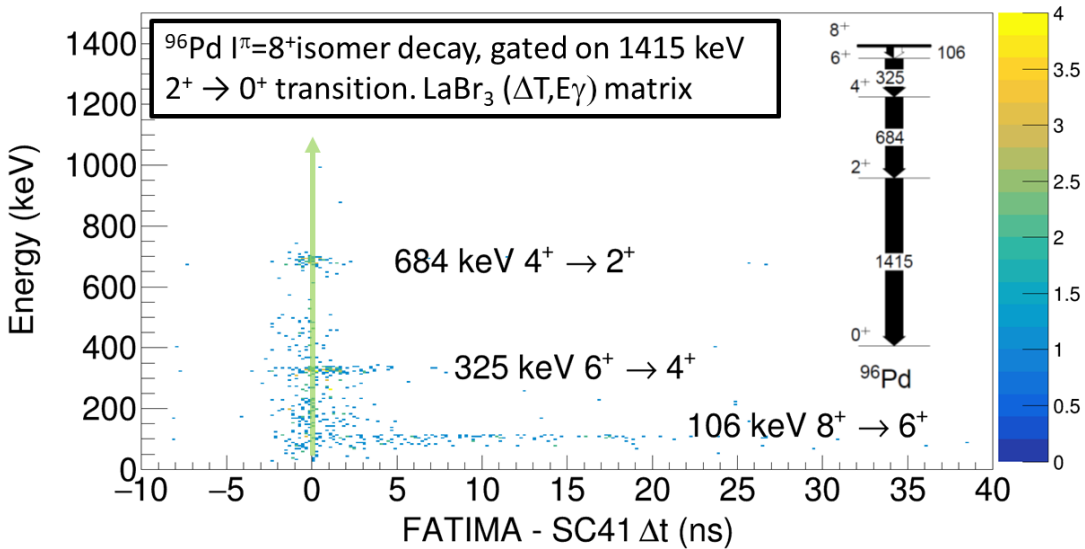


FIGURE 5.1: Background subtracted $E_\gamma - E_\gamma$ coincidence spectra for isomer delayed events gated on ^{96}Pd with the conditions that both gamma rays were detected between 40 and 400 ns after the implantation in AIDA.

Figures 5.2 a), b) and c) are projections of a $E_\gamma - E_\gamma$ energy matrix gated on the 1415 keV, 684 keV and 325 keV yrast band transitions in ^{96}Pd . The spectra have undergone a one dimensional normalised background subtraction which includes applying an energy gate to a region lower in energy than the peak area and subtracting this background gate from the main coincident gate. The background region is taken lower in energy to ensure the subtraction of higher energy, compton-scattered gamma rays from the peak region. As a result the 1415 keV subtraction does very little as there are no gamma rays in the cascade above this energy while the 325 keV subtraction shows a larger improvement in peak to total ratios due to it sitting on a Compton background for scatters from the 1415 keV and 684 keV peaks as well as the natural background peak at 1460 keV (^{40}K) and the 511 keV annihilation peak.

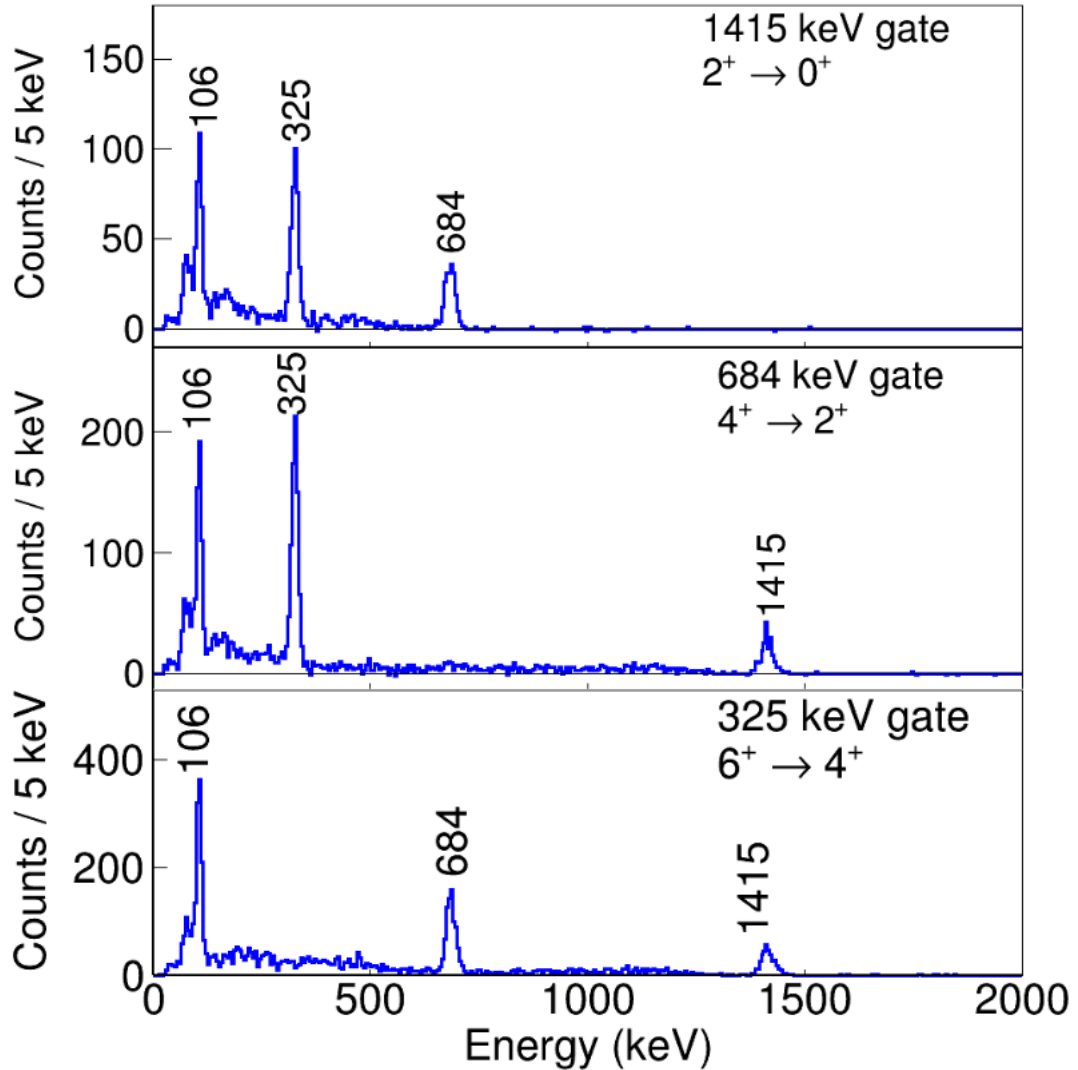


FIGURE 5.2: Background subtracted $E_\gamma - E_\gamma$ coincidence spectra for isomer delayed events gated on ^{96}Pd with the conditions that both gamma rays were detected between 40 and 400 ns after the implantation in AIDA.

Gates were then placed on pairs of coincident gamma rays in order to extract half-life plots for the 2^+ , 4^+ and 6^+ states in ^{96}Pd . These spectra can be seen in figure 5.3 and have had a normalised two dimensional background subtraction algorithm applied to them. This algorithm is described in equation 5.1 and is applied to reduce the effect of random events in the peak region.

$$S_f = S_{p1p2} - S_{p1bg2} - S_{bg1p2} + 2 * S_{bg1bg2} \quad (5.1)$$

Where S corresponds to a given spectra gated on either the peak "p" and/or background "bg" region(s) of the gamma rays (1 or 2) in the cascade. 5.3

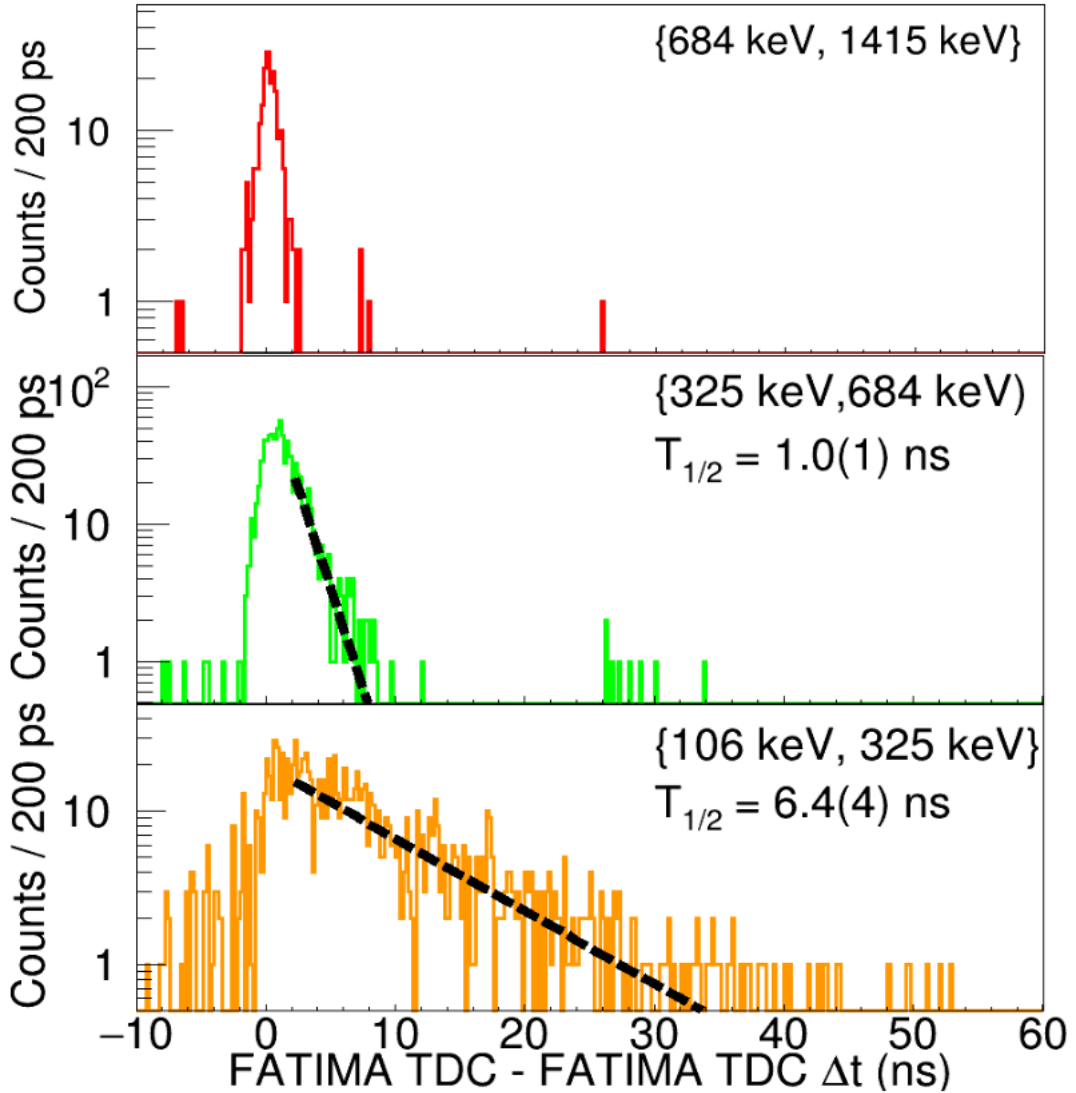


FIGURE 5.3: The ^{96}Pd isomer gated time difference spectra for the $8^+ \rightarrow 6^+ \rightarrow 4^+ \rightarrow 2^+ \rightarrow 0^+$ yrast decay sequence using FATIMA at DESPEC. The time spectra are fitted to a single exponential decay function between 2 and 40 ns after the nominal $\Delta T = 0$ time.

Figure 5.3 (upper) shows a prompt relationship between the timing signals of the 1415 keV and 684 keV gamma rays, signalling an instantaneous (< 100 ps) decay of the 2^+ state. Figure 5.3 (central) shows a longer lived 4^+ state with a half-life of $1.0(1)$ ns and a clear contrast can be seen with a). Finally, 5.3 (bottom) shows a much longer lived 6^+ state with a half-life of $6.4(4)$ ns. This analysis shows a strong agreement on the work done by Mach et al. when analysing the same nucleus. A slight reduction in the uncertainty in the 6^+ half-life is seen while the 4^+ half-life shows an increase in uncertainty but despite this all measurements are in agreement. The ability of this experimental set-up to reproduce previously measured half-lives improves the confidence of the next measurements which were carried out.

5.1.2 Transitions Populated Following the Decay of the 14^+ Isomer in ^{94}Pd

Figure 5.4 (upper) shows a total projection of the $E_\gamma E_\gamma \Delta T$ cube on a gamma-rays axis which shows the cascade of gamma rays below the 14^+ isomer while b) and c) show background subtracted spectra gated 324 keV and 1092 keV gamma-rays spectra respectively.

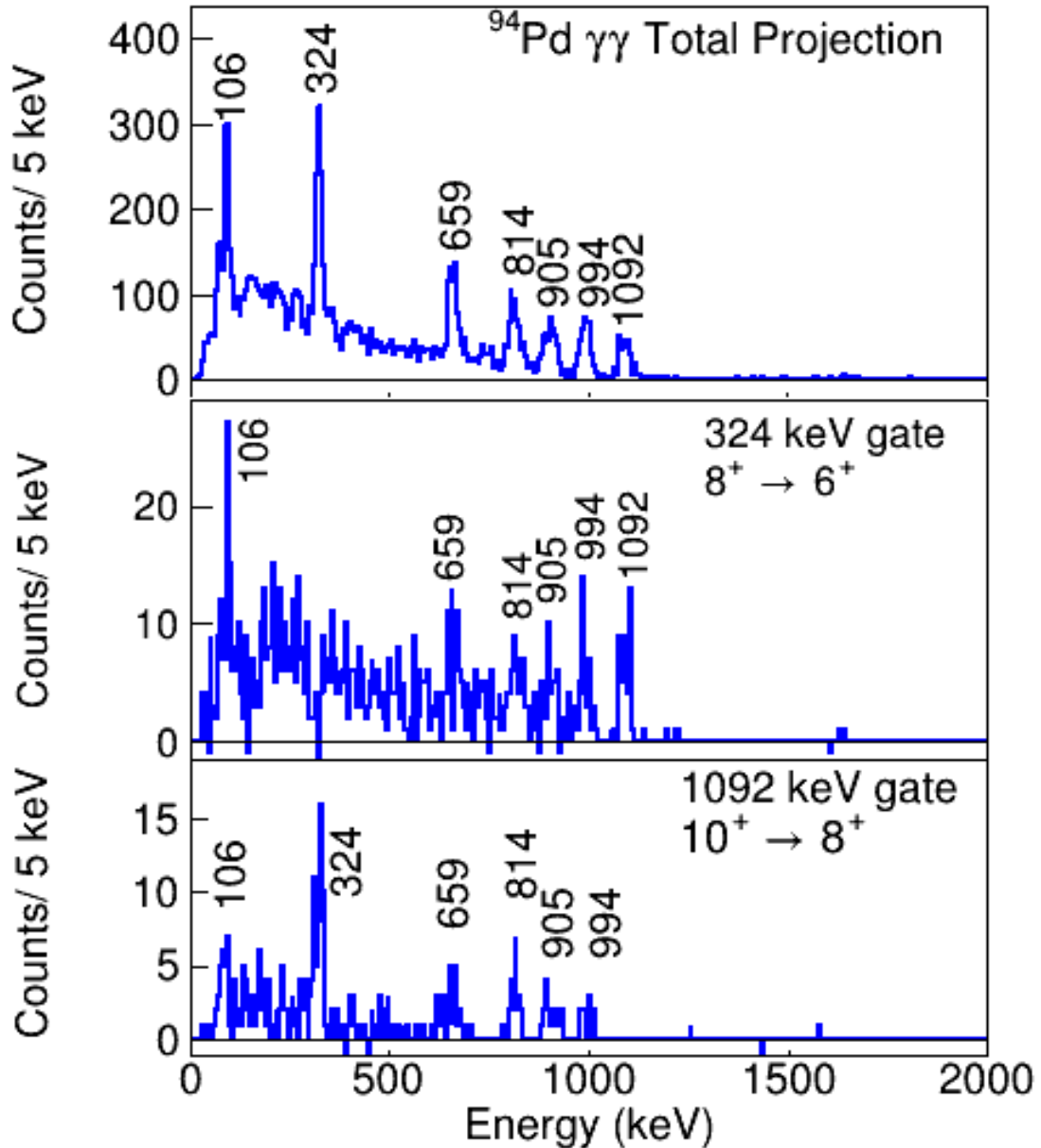


FIGURE 5.4: The FATIMA gamma-rays energy vs FATIMA - SC41 time difference spectra resulting from a gate on ^{96}Pd ions from the FRS detectors, a high energy ion event in the bFast plastic scintillation detector, a clean signal through the SC41 and SC42 scintillators and an implantation in AIDA.

Figures 5.5 a) to f) show the 2D background subtracted half-life plots for the 2^+ , 4^+ , 6^+ , 8^+ , 10^+ and 12^+ states. All states other than the 8^+ show a prompt decay, characterised by a Gaussian distribution centred at 0 ns with no exponential decay. The 8^+ when fit to an exponential decay gives a $1.2(3)$ ns half-life.

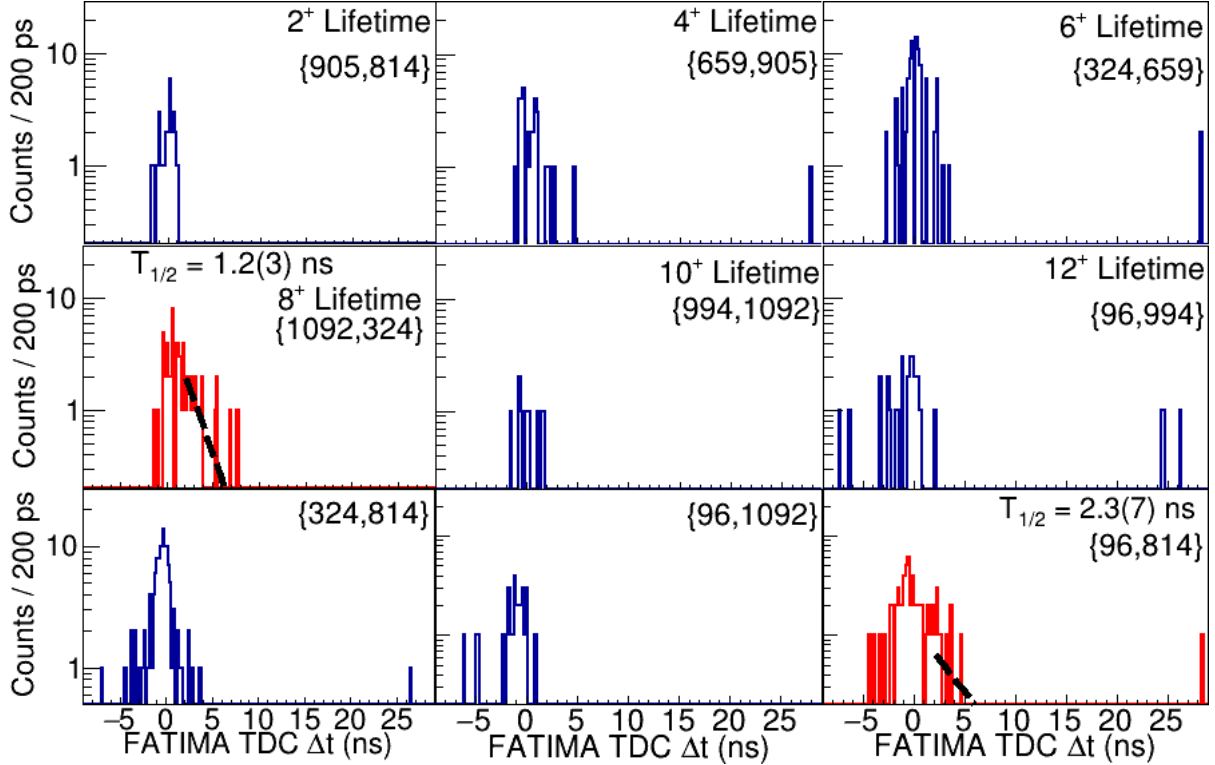


FIGURE 5.5: The FATIMA - FATIMA TDC time differences for various combinations of start stop timing conditions. The plots show from the top row left to right the 2^+ , 4^+ and 6^+ half-lives which all appear to be prompt transitions. The central plot and the plot to its right show the 10^+ and 12^+ half-lives which are also prompt. The central-left plot in red shows the half-life of the state of interest with a half-life value of $1.2(3)$ ns. The bottom row of figures from left to right show a series of time difference plots gated above and below the 8^+ state.

While the counts in these plots are incredibly clean due to the extensive background subtraction along with a strong gating parameter there is a statistical limitation due to the low number of ^{94}Pd ions created by the projectile fragmentation reaction along with its low isomeric ratio. Due to the prompt nature of the ^{94}Pd yrast band states either side of the 8^+ it is possible to collate extra statistics by gating on all of the pairs of gamma-ray transitions either side of the state provided that all pairs of transitions higher or lower than the state of interest are mutually prompt.

Figure 5.6 (upper) shows a summed time difference spectra gated on the 96 keV, 994 keV and 1092 keV gamma rays using each of them as stop and start timing conditions. This plot is centred at 0 ns implying that the times between these transitions are prompt. 5.6 (bottom) shows the same, summed plot for pairs of transitions below

the 8^+ state which displays the same properties as the plot in the upper plot. The central plot in figure 5.6 shows a summed plot of all pairs of transitions going across the 8^+ state with an exponential decay fit applied to it. This fit gives a value of $1.13(9)$ ns for the first measurement of the half-life of the 8^+ state in ^{94}Pd showing an improvement in the accuracy of the method and a reduction in uncertainty, likely due to the increase in statistics.

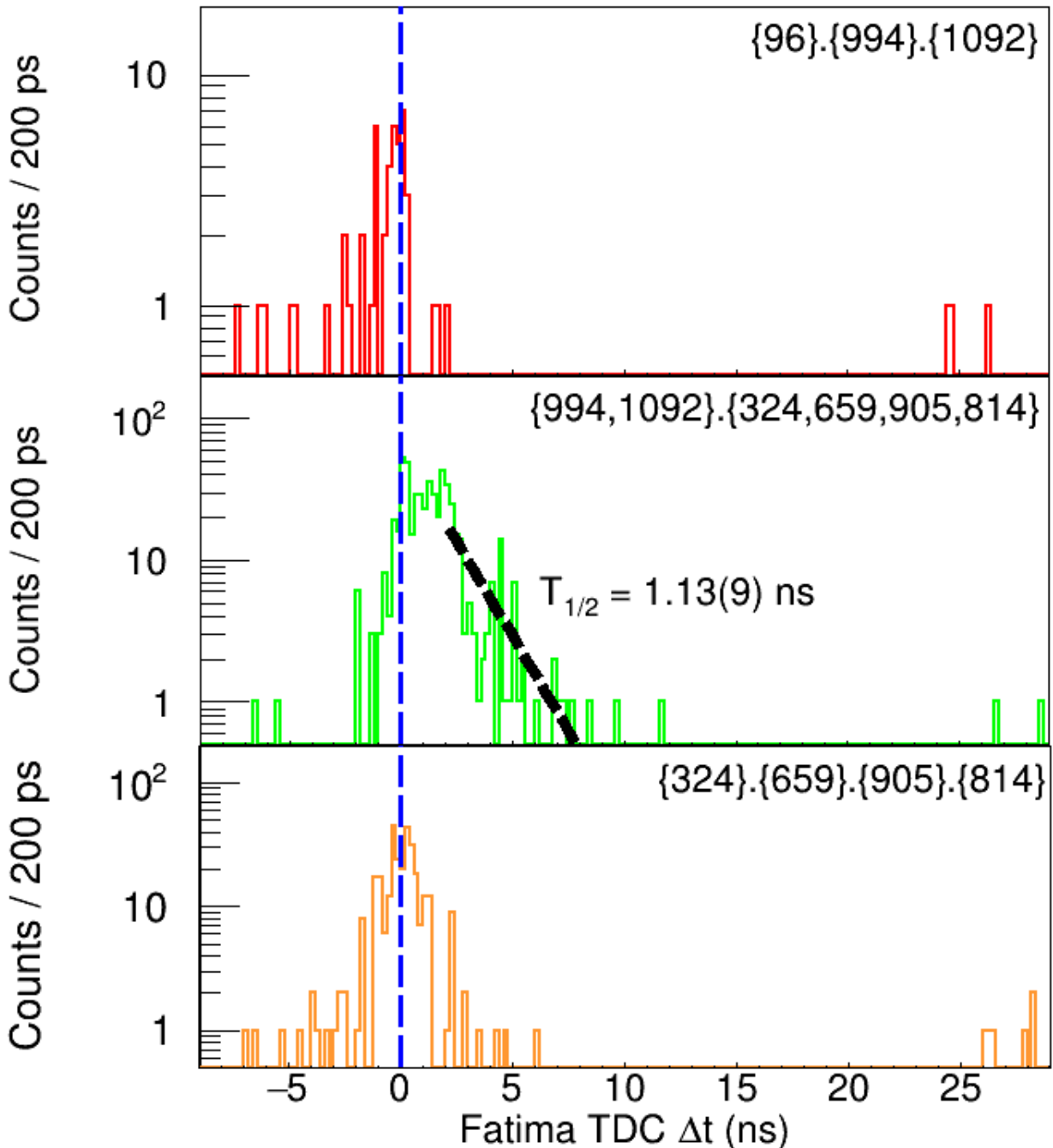


FIGURE 5.6: Time difference figures for isomeric transitions above and below the 8^+ state in ^{94}Pd . The top figure shows the combinations of transitions above the state while the bottom figure shows those time differences for the combinations below. The central figure is a measurement of the half-life of the 8^+ state fit with an exponential decay function. This plot was constructed by using all gamma rays above the state as a start condition and any of those below as a stop.

5.1.3 Transitions Populated Following the Decay of the 8^+ Isomer in ^{94}Ru

Figure 5.5 (upper) shows the ^{94}Ru PID gated, background subtracted gamma rays below the 8^+ isomeric state in ^{94}Pd gated on 1431 keV gamma rays. The 146 keV, 311 keV and 755 keV transitions can be seen in the gate as well as the ~ 35 keV ^{138}Ba X-rays following the electron capture peak of ^{138}La . This peak is solely present in the 1431 keV gate because the electron capture is followed by a 1436 keV transition from an excited state in ^{138}Ba to its ground state which is within the gating range of the $2^+ \rightarrow 0^+$ transition. The central and bottom plots in figure 5.7 are gated on 311 keV and 755 keV transitions respectively and show the other coincident gamma rays in the cascade.

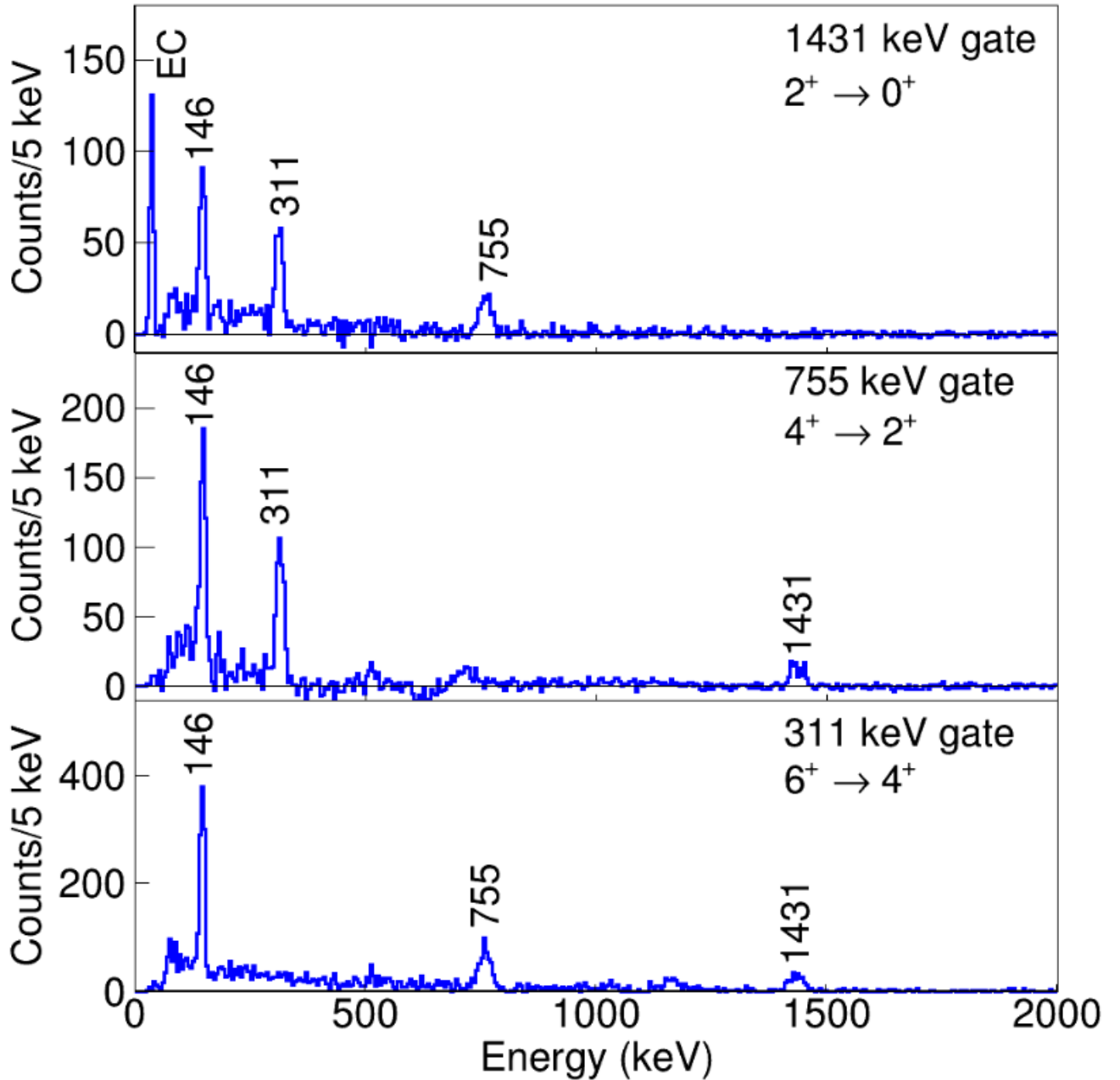


FIGURE 5.7: The background subtracted $\gamma - \gamma$ coincidence spectra for isomer delayed events gated on ^{94}Ru with the condition that the gamma rays were detected between $80\ \mu\text{s}$ and $350\ \mu\text{s}$ after the implantation in the AIDA stopper. The EC label represents the La K x-rays in coincidence with the $1436\text{ keV }2^+ \rightarrow 0^+$ transition in ^{138}Ce arising from the internal activity of the $\text{LaBr}_3(\text{Ce})$ detectors.

Figures 5.8 a) b) and c) show the $\gamma - \gamma$ time differences between the two transitions across the 6^+ , 4^+ and 2^+ states. The 6^+ and 4^+ states present a prompt time difference meaning these are extremely short lived states. The exponential decay in counts seen in the 2^+ state gives a value of $T_{\frac{1}{2}} = 63(4)\ \text{ns}$. This value is consistent with and reproduced by work done by Das et al., [101] which gives a value of $T_{\frac{1}{2}} = 65(2)\ \text{ns}$ for

nuclei populated via the beta-delayed proton emission channel from ^{95}Pd , using data from this experiment. Hafner et al. [12] also produces a comparable result of $T_{\frac{1}{2}} = 64(4)$ ns with the data being gathered from the fragmentation of a ^{124}Xe beam carried out at Radioactive Ion Beam Factory of the RIKEN Nishina Center, Japan. These comparable results further improve the confidence level of for the measurement of the half-life of the 8^+ state in ^{94}Pd .

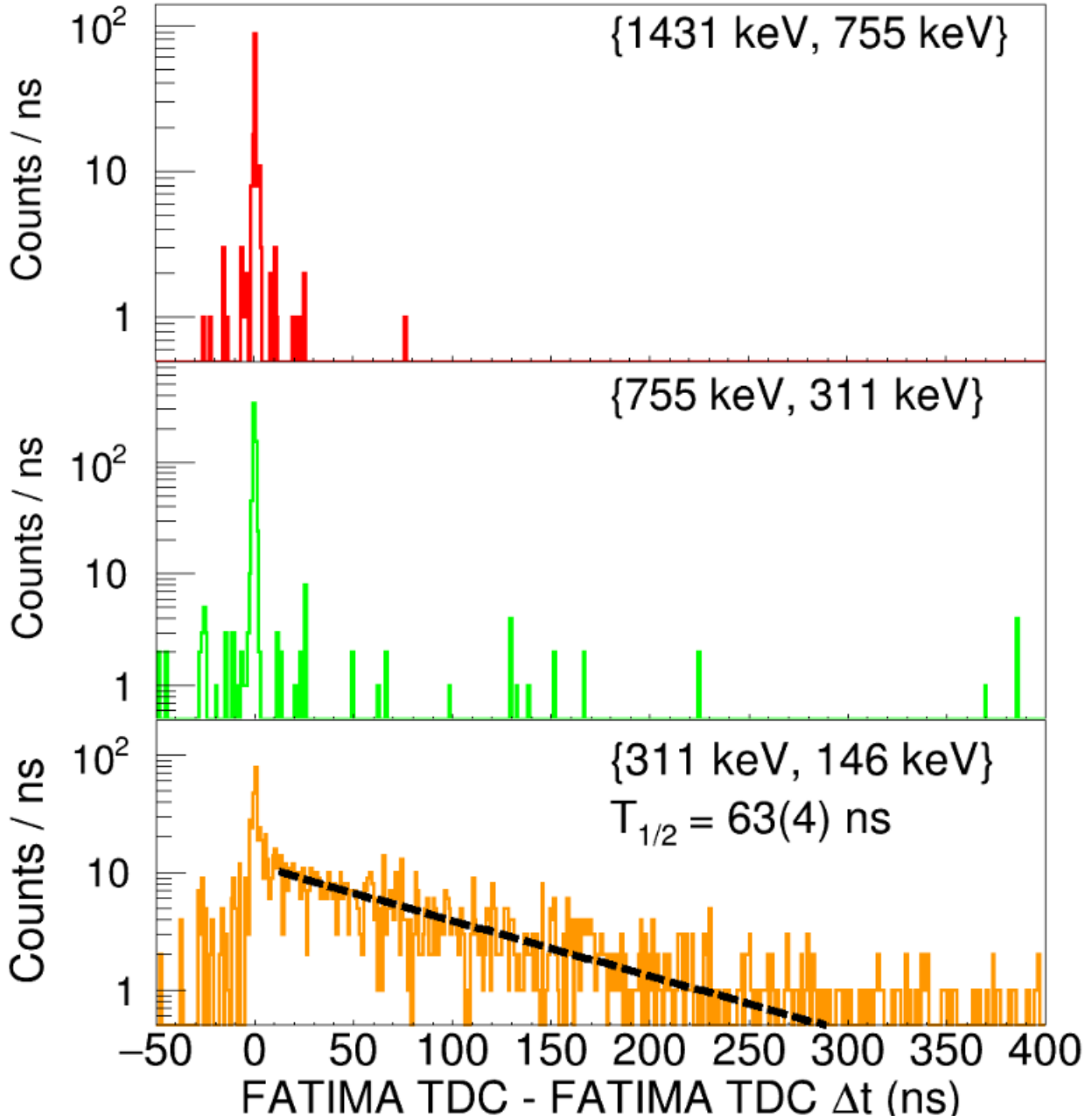


FIGURE 5.8: ^{94}Ru isomer-gated time difference spectra for the $8^+ \rightarrow 6^+ \rightarrow 4^+ \rightarrow 2^+ \rightarrow 0^+$ yrast decay sequence using the FATIMA system at DESPEC. The time spectra are fitted to a single exponential decay function between 2 and 300 ns after the nominal $\Delta T = 0$ time.

5.1.4 Calculation of B(E2) Values

The results from this work are summarised below in table 5.1 with the B(E2) values calculated using equation 2.23. The largest source of uncertainties for these results were statistical in nature and arose from the fits in the half-lives for these measurements with the high precision of the detectors contributing very little in comparison.

Ion	E_x (keV)	E_γ (keV)	$I_i - I_f$	$T_{\frac{1}{2}}$	Lit. $T_{\frac{1}{2}}$	α_{tot}	$B(E2: I \rightarrow I-2) \downarrow e^2 b^2$
$^{94}\text{Pd}_{48}$	4884	96	$14^+ \rightarrow 12^+$	499(9) ns	515(10) ns	1.62(2)	$5.3(1) \times 10^{-3}$
	2702	324	$8^+ \rightarrow 6^+$	1.2(3) ns	—	0.0229(4)	$1.3(3) \times 10^{-2}$
$^{96}\text{Pd}_{50}$	2531	106	$8^+ \rightarrow 6^+$	1.81(1) μs	1.84(2) μs	1.134(16)	$1.09(1) \times 10^{-3}$
	2424	325	$6^+ \rightarrow 4^+$	6.4(4) ns	6.3(6) ns	0.0227(4)	$2.4(2) \times 10^{-3}$
$^{94}\text{Ru}_{50}$	2099	684	$4^+ \rightarrow 2^+$	1.0(1) ns	1.0(1) ns	0.00243(4)	$3.8(4) \times 10^{-4}$
	1415	1415	$2^+ \rightarrow 0^+$	Prompt	<17 ps	<0.001	$>5 \times 10^{-4}$
$^{94}\text{Ru}_{50}$	2644	146	$8^+ \rightarrow 6^+$	64(1) μs	64(4) μs	0.334(5)	$1.0(1) \times 10^{-5}$
	2498	311	$6^+ \rightarrow 4^+$	63(4) ns	65(2) ns	0.0238(4)	$3.1(2) \times 10^{-4}$

TABLE 5.1: A summary of the half-life measurements and calculated $B(E:I \rightarrow I-2) \downarrow$ values in ^{96}Pd , ^{94}Pd and ^{94}Ru . The literature values are taken from [12, 44] and the internal coefficients are taken from the BRICC database [53]

5.2 Comparison of Results With Shell Model Calculations

Figures 5.9 and 5.10 shows a comparison between the calculated B(E2) values in units of $e^2 \text{fm}^4$ for the isomeric cascades in ^{96}Pd and ^{94}Pd using the collective JUN45 interaction force along with the seniority reliant Gross-Fenkel interaction. The Gross-Fenkel model operates in the $g_{\frac{9}{2}} p_{\frac{1}{2}}$ model space and often produces smaller B(E2) values than the JUN45 interaction which operates in the $f_{\frac{5}{2}} p_{\frac{3}{2}} p_{\frac{1}{2}} g_{\frac{9}{2}}$ space. These larger B(E2) values predicted by JUN45 correspond to the larger model space with the nucleons of interest forming more collective states which in turn lead to the prediction of higher spin states. Meanwhile, the Gross-Fenkel interaction predicts a maximum spin of 8^+ in ^{96}Pd due to this being the maximum allowed spin in the $g_{\frac{9}{2}}$ model space with a seniority of 2.

Figure 5.9 shows that the experimentally measured values for $B(E2: J \rightarrow J-2)$ correlate well with the predictions made by the Gross-Fenkel calculations for the $8^+ \rightarrow 6^+ \rightarrow 4^+ \rightarrow 2^+ \rightarrow 0^+$ isomeric gamma-ray cascade in ^{96}Pd . Furthermore, a strong correlation is also seen between the Gross-Fenkel prediction and the experimental data with

the prediction made by the JUN45 interaction for the $B(E2)$ of the $8^+ \rightarrow 6^+$ transition, proving the effectiveness of the seniority as a quantum number for this nucleus.

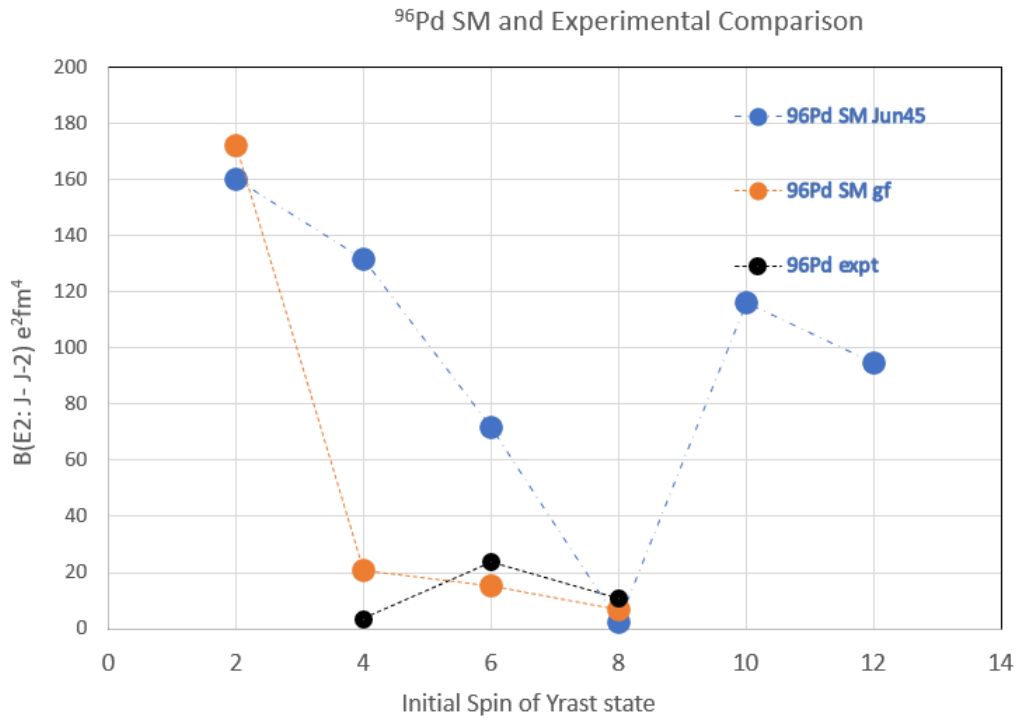


FIGURE 5.9: A plot comparing the Gross-Fenkel and JUN45 interaction force predictions of the $B(E2)$ values of the transitions below the isomeric cascade in ^{96}Pd .

Finally, the experimentally measured $B(E2)$ values for the $8^+ \rightarrow 6^+$ transition in ^{94}Pd show a strong agreement with the Gross-Fenkel prediction for $B(E2)$ values of states including and below the 14^+ meaning the seniority regime continues to provide a strong contribution to the energetics of ^{94}Pd despite the loss of two neutrons when compared with ^{96}Pd .

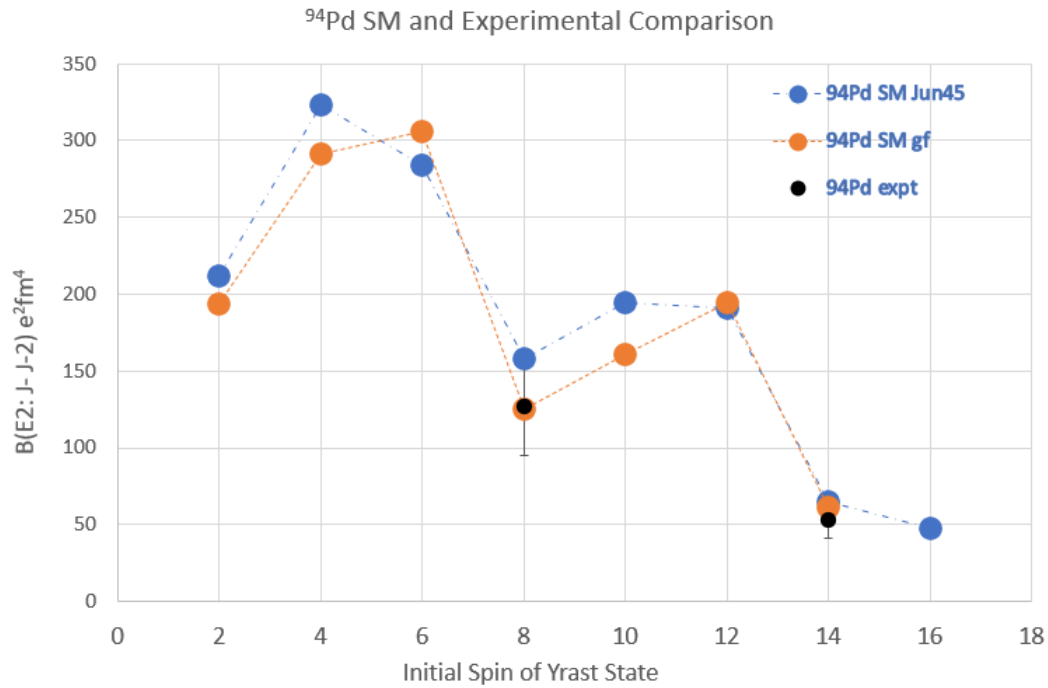


FIGURE 5.10: A plot comparing the Gross-Fenkel and JUN45 interaction force predictions of the $B(E2)$ values for the transitions below the isomeric cascade in ^{94}Pd .

Chapter 6

Conclusion

The results from the commissioning run of the DESPEC set-up have been presented in this thesis. Experiment S480 has yielded a number of scientific results pertaining to the isomeric yrast 8^+ , 14^+ and 8^+ states in ^{96}Pd , ^{94}Pd and ^{94}Ru respectively. Despite the limitations of the timing range of FATIMA the isomeric ratios of these states have been measured to be $R = 50(2)\%$, $11(1)\%$ and $34(3)\%$ respectively which are in agreement with previous literature measurements. The isomeric ratio measurements were used to validate a novel Monte Carlo GEANT4/NPTool simulation of the DESPEC set-up @ GSI. The full energy peak efficiencies of FATIMA at energies of 106 keV, 325 keV, 684 keV and 1415 keV have been measured at $11.2(11)\%$, $6.8(7)\%$, $3.8(6)\%$ and $2.1(5)\%$ respectively which compare favourably with the simulated results of $9.85(3)\%$, $6.5(2)\%$, $3.65(1)\%$ and $1.96(2)\%$ respectively. Now validated, this simulation will be greatly useful in the planning of future fast timing and decay spectroscopy experiments by providing insight into the response of the FATIMA array when observing gamma rays of interest.

Additionally, half-lives for the states below the isomer have been measured using the FATIMA system at the FAIR-0 facility. The 8^+ , 6^+ , 4^+ and 2^+ states in ^{96}Pd were measured to have half-lives of $1.81(1)$ μs , $6.3(6)$ ns, $1.0(1)$ ns and ~ 17 ps respectively. Additionally the 14^+ and 8^+ states in ^{94}Pd revealed measured half-lives of $499(9)$ ns and $1.2(3)$ ns while the 8^+ and 6^+ states in ^{94}Ru were found to posses half-lives of $64(1)$ μs and $63(4)$ ns respectively. These measurements were combined with the energies of these excited states to provide a robust test of state-of-the-art shell model calculations carried out with the aim of determining the role of nucleon-nucleon pairing near closed shell nuclei. The half-life measurements were used to calculate $B(E2)$ values for all states with these calculations showing a strong agreement of the measured $B(E2)$ value for the $8^+ \rightarrow 6^+$ transition in ^{94}Pd with the prediction made when using the Gross-Fenkel

interaction model. This proves the significance of the seniority interaction in nucleon-nucleon pairing in ^{94}Pd before the breakdown of seniority in ^{92}Pd , thus improving our understanding of nuclear energetics around the ^{100}Sn region of the nuclear chart.

A number of lessons were learned through the runtime of experiment S480. As the commissioning run of the set-up issues such as AIDA event processing were improved and the error of cross-board TDC desynchronisation were solved. Furthermore, the development of the NPTTool simulation of the DESPEC set-up will prove to be an excellent tool in the planning of future experiments. When fully completed the simulation will give future researchers the ability to view accurate predictions of gamma-ray and particle spectra which are greatly useful when pushing the boundaries of known nuclear data.

6.1 Future Work

There still remains many measurements to be made of near-closed shell nuclei. Proposals have been submitted for an experimental campaign for the International Detector Assembly for fast-Timing measurements of Exotic Nuclei (IDATEN) array. IDATEN is a proposed hybrid array composed of FATIMA $\text{LaBr}_3(\text{Ce})$ detectors as well as 1.5" x 1.5" $\text{LaBr}_3(\text{Ce})$ detectors which make up the KHALA array. Simulation work has already begun on combining the current existing FATIMA detector simulation with the KHALA detectors to provide a level of support and planning for this upcoming campaign focussed on fragmentation decay spectroscopy at RIBF, RIKEN similar to the foundations which were laid for the use of FATIMA in the DESPEC setup in reference [102]. A design schematic of the proposed setup taken from the IDATEN technical proposal can be seen in figure 6.1. Interesting applications also exist in the form of potentially using FATIMA or other scintillation detectors as fast-neutron detectors with work being done recently to show this application [103].

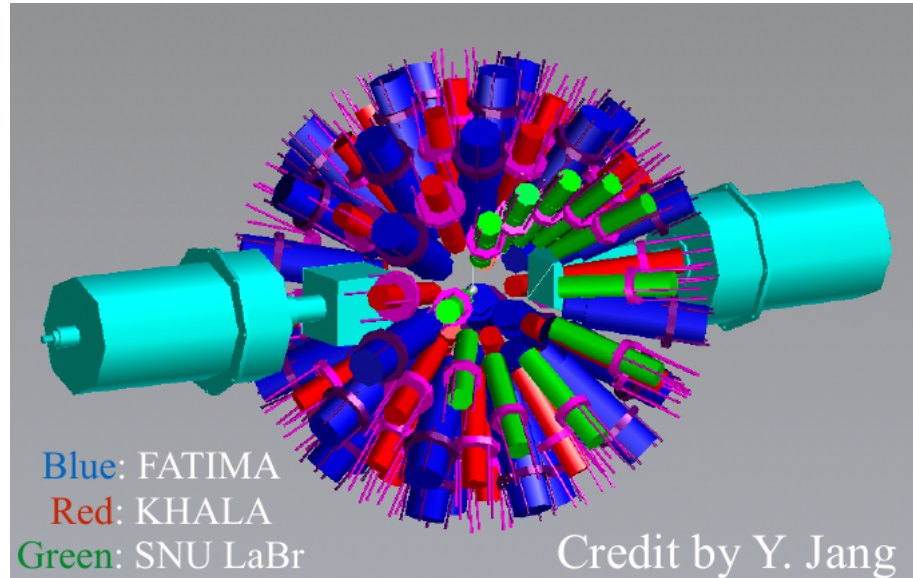


FIGURE 6.1: The schematic of the proposed IDATEN array consisting of 36 1.5" x 2" $\text{LaBr}_3(\text{Ce})$ FATIMA detectors, 48 1.5" x 1.5" $\text{LaBr}_3(\text{Ce})$ KHALA detectors and 2 SNU clover type HPGe detectors taken from work done by Y. Jang.

Appendix A

Research Outputs

A.1 Main Author Publications

S. Jazrawi, D.T. Doherty, J.M. Allmond, P.H. Regan, et al., A High-Resolution Study of the $^{110}\text{Tc} \rightarrow ^{110}\text{Ru} \rightarrow ^{110}\text{Rh} \rightarrow ^{110}\text{Pd}$ Decay Chain with the GRETINA Array Proceedings of the 27th International Nuclear Physics Conference 2019 Journal of Physics: Conference Series 2020, 1643(1) 012140 (2020)

S. Jazrawi, A. Yaneva, M. Polettini, P.H. Regan, et al., Commissioning the FAst TIMing array (FATIMA) at FAIR Phase-0: Half-lives of excited states in the N=50 isotones ^{96}Pd and ^{94}Ru Proceedings of the 15th International Symposium on Radiation Physics 2021 Radiation Physics and Chemistry, 110234. (2022)

M.M.R Chishti, S. Jazrawi, R. Shearman, P.H. Regan et al., Response of the FAst TIMing Array (FATIMA) for DESPEC at FAIR Phase-0. Submitted to Nuclear Instruments and Methods in Physical Research A, (2022)

A. Yaneva, S. Jazrawi, B.Das, M.Mikolajczuk, M.Górska, P.H.Regan, B.Cederwall, J.Jolie, G.Benzoni, et al., Fast-timing measurement in ^{96}Pd : Improved accuracy for the lifetime of the 4_+^1 state. Submitted to Proceedings, Zakopane Conference on Nuclear Physics (2022)

A.2 Other Publications as Contributing Author

R.B. Gerst, A. Blazhev, N. Warr, J.N. Wilson, M. Lebois, ... S. Jazrawi. Prompt and delayed γ spectroscopy of neutron-rich ^{94}Kr and observation of a new isomer. Physical Review C, 102(6), 064323. (2020)

A.R.L. Kennington, G. Lotay, D.T. Doherty, D. Seweryniak, S. Zhu, ... S. Jazrawi Search for Nova Presolar Grains: γ -Ray Spectroscopy of ^{34}Ar and its Relevance for the Astrophysical ^{33}Cl (p, γ) Reaction. Physical Review Letters, 124(25), 252702. (2020)

A.R.L. Kennington, G. Lotay, D.T. Doherty, D. Seweryniak, S. Zhu, ... S. Jazrawi Level structure of the $T_z = -1$ nucleus ^{34}Ar and its relevance for nucleosynthesis in ONe novae. Physical Review C, 103(3), 035805. (2021)

M. Polettini, S. Jazrawi, M.M.R. Chishti, A. Yaneva, A. Banerjee, DESPEC Phase-0 campaign at GSI SIF Congress (No. 2-3, p. 67). (2020)

J.N. Wilson, D. Thisse, M. Lebois, ... S. Jazrawi Angular momentum generation in nuclear fission, Nature, 590(7847), 566-570. (2021)

G. Lotay, S. Gillespie, A. Williams, B. Davids, ... S. Jazrawi First Direct Measurement of an Astrophysical p-Process Reaction Cross Section Using a Radioactive Ion Beam. Physical Review Letters, 127(11), 112701. (2021)

A.K. Mistry, H.M. Albers, T. Arıcı, A. Banerjee, ... S. Jazrawi The DESPEC setup for GSI and FAIR. Nuclear Instruments and Methods in Physics Research Section A: Accelerators, Spectrometers, Detectors and Associated Equipment, 1033, 166662. (2022)

B. Das, B. Cederwall, ... S. Jazrawi Nature of seniority symmetry breaking in the semimagic nucleus ^{94}Ru Physical Review C, 105(3), L031304. (2022)

A.3 Presentations Given

A.3.1 Oral Presentations

High-Resolution β -delayed γ -ray Study of the $^{110}\text{Tc} \rightarrow ^{110}\text{Ru} \rightarrow ^{110}\text{Rh} \rightarrow ^{110}\text{Pd}$ Isobaric Decay Chain Presented at the Advanced Nuclear Science and Technology Techniques (ANSTT2) Workshop, iThemba Labs, South Africa, 2019

High-Resolution β -delayed γ -ray Study of the $^{110}\text{Tc} \rightarrow ^{110}\text{Ru} \rightarrow ^{110}\text{Rh} \rightarrow ^{110}\text{Pd}$ Isobaric Decay Chain Presented at the Universities' Nuclear Technologies Forum (UNTF) Workshop, University of Surrey, United Kingdom, 2019

High-Resolution β -delayed γ -ray Study of the $^{110}\text{Tc} \rightarrow ^{110}\text{Ru} \rightarrow ^{110}\text{Rh} \rightarrow ^{110}\text{Pd}$ Isobaric Decay Chain Presented at the 75th Scottish Universities Physics Alliance (SUSSP) and 20th Science and Technology Facilities Council (STFC) Summer School in Nuclear Physics and its Applications, St. Andrews University, United Kingdom, 2019

A Preliminary Analysis of Isomeric and Yrast State Lifetimes in $^{96,94}\text{Pd}$ using FATIMA @ DESPEC Presented at Lockdown Nuclear Physics Seminars, University of Liverpool, UK, 2020 (Online)

First results from FATIMA within the DESPEC collaboration at FAIR-0 Presented at the International Symposium on Radiation Physics (ISRP) Kuala Lumpur, Malaysia, 2021 (Online)

Commissioning the Fast TIMing Array (FATIMA) at FAIR-0: Lifetimes of Excited states in the N=50 isotones ^{96}Pd and ^{94}Ru Presented at the Institute Of Phyics (IOP) Nuclear Physics Conference, University of Surrey, United Kingdom, 2022

A.3.2 Poster Presentations

High-Resolution β -delayed γ -ray Study of the $^{110}\text{Tc} \rightarrow ^{110}\text{Ru} \rightarrow ^{110}\text{Rh} \rightarrow ^{110}\text{Pd}$ Isobaric Decay Chain Presented at the 27th International Nuclear Physics Conference (INPC), Glasgow, United Kingdom, 2019

High-Resolution β -delayed γ -ray Study of the $^{110}\text{Tc} \rightarrow ^{110}\text{Ru} \rightarrow ^{110}\text{Rh} \rightarrow ^{110}\text{Pd}$ Isobaric Decay Chain Presented at the Conference on Applied Radiation Metrology (CARM), National Physical Laboratory, United Kingdom, 2019

Yrast State Lifetime Mesurements in $^{96,94}\text{Pd}$ using FATIMA @ DESPEC Presented at the Institute Of Physics (IOP) Joint Astroparticle Physics (APP), High Energy Particle Physics (HEPP) and Nuclear Physics (NP) Conference, Online, 2021

Simulated response for the DESPEC Gamma Array at FAIR Presented at the Institute Of Physics (IOP) Nuclear Physics Conference on behalf of M.M.R Chishti, University of Surrey, United Kingdom, 2022

Commissioning the Fast TIMing Array (FATIMA) at FAIR-0: Lifetimes of Excited states in the N=50 isotones ^{96}Pd and ^{94}Ru Presented at the Institute Of Phyics (IOP) Nuclear Physics Conference, University of Surrey, United Kingdom, 2022

Bibliography

- [1] T. Faestermann et al., Progress in Particle and Nuclear Physics **69**, 85 (2013)
- [2] M. Honma, Physical Review C **80**, 064323 (2009)
- [3] B. S. Nara Singh et al., Physical Review Letters **107**, 172502 (2011)
- [4] M. Rudigier et al., Nuclear Instruments and Methods in Physics Research A **969**, 163967 (2020)
- [5] P.H. Regan, Radiation Physics and Chemistry **116**, 38-42(2015)
- [6] O. Hall et al., Physics Letters B **816**, 136266 (2021)
- [7] A. Blazhev et al., Journal of Physics: Conference Series. **205**, 012035 (2010)
- [8] A.K. Mistry et al., Nuclear Instruments and Methods in Physics Research A **1033(1)**, 166662 (2022)
- [9] L. Zamick, Physical Review C **93**, 034327 (2016)
- [10] A. Blazhev, et al., Physical Review C **69**, 064304 (2004)
- [11] T.S. Brock et al., Physical Review C **82**, 061309(R) (2011)
- [12] G. Häfner et al., Physical Review C **100**, 024302 (2019)
- [13] A.B. Garnsworthy et al., Physical Review C **80**, 064303 (2009)
- [14] M. Górska et al., Zeitschrift für Physik A **A353**, 233 (1995)
- [15] R. Grzywacz et al., Physical Review C **55**, 1126 (1997)
- [16] H. Grawe and M. Hass, Physics Letters B **120**, 63-66 (1983)
- [17] N. Marginean et al., Physical Review C **67**, 061301(R) (2003)
- [18] J.J. Ressler et al., Physical Review C **69(3)**, 034317 (2004)
- [19] M.A. Caprio et al., Physical Review C **85(3)**, 034324 (2012)

- [20] A.I. Morales et al., Physics Letters B **781**, 706-714 (2018)
- [21] C.J. Chiara et al., Physical Review C, **84(3)**, 037304 (2011)
- [22] C. Qi et al., Physics Letters B, **773**, 616-619 (2017)
- [23] A. Escuderos, Physical Review C **73(4)**, 044302 (2006)
- [24] M. Górska, Physics **4(1)**, 364-382 (2022)
- [25] A.F. Lisetskiy et al., Physical Review C **70**, 044314 (2004)
- [26] B. Cederwall et al., Nature **469**, 68-71 (2011)
- [27] F. Nowacki et al., Physical Review Letters **107**, 172502 (2011)
- [28] P. Boutachkov et al., Physical Review C **84**, 064323 (2009)
- [29] P.J.Davies et al., Physics Letters B **767**, 474-479 (2017)
- [30] P.J.Davies et al., Physical Review C **99**, 021302(R) (2019)
- [31] J. Park et al., Physical Review C **96**, 044311 (2017)
- [32] J. Park et al., Physical Review C. **99**, 034313 (2019)
- [33] F.J.D. Serduke et al., Nuclear Physics A **256**, 45 (1976)
- [34] R. Gross and A. Frenkel, Nuclear Physics A **267**, 85 (1976)
- [35] S. Zerguine et al., Physical Review C **83**, 064314 (2011)
- [36] Z. X. Xu et al., Nuclear Physics A. **877**, 51 (2012)
- [37] C. Qi et al., Physical Review C **84**, 021301 (2011)
- [38] P. Van Isacker et al., International Journal of Modern Physics E **22**, 1330028 (2013)
- [39] L. Coraggio et al., Physical Review C **85**, 034335 (2012)
- [40] ENSDF Database, www.nndc.bnl.gov/ensdf/, (Site Visited September 2022).
- [41] M. Górska, P.H. Regan, B. Cederwall, J. Jolie et al., *Structure of the heaviest $N = Z$ nuclei: Seniority Transitions and EM Transition Rates in ^{94}Pd* , Proposal for NUSTAR Phase-0 Experiments (2019)
- [42] C. Plettner et al., Nuclear Physics A **733**, 20 (2004)
- [43] M. LaCommara et al., Nuclear Physics A **708**, 167 (2002)

- [44] H. Mach et al., Physical Review C **95**, 014313 (2017)
- [45] E. Gapon et al., Naturwissenschaften **43**, 792-793 (1932)
- [46] W. Pauli, Zeitschrift für Physik **Feb**, 765-783 (1925)
- [47] D.R. Lide, CRC Press, Handbook of Chemistry and Physics (84th edition) (2003-2004)
- [48] D.S. Saxon et al., Physical Review **2**, 577-578 (1954)
- [49] K.S. Krane, Wiley, Introductory Nuclear Physics (1987)
- [50] R. Casten and R.F. Casten, Oxford University Press, Nuclear structure from a simple perspective(Vol. 23) (2004)
- [51] P. Walker et al., Nature **399(6731)**, 35-40 (1999)
- [52] G.D. Dracoulis et al., Reports on Progress in Physics **79(7)**, 076031 (2017)
- [53] T. Kibédi et al., Nuclear Instruments and Methods in Physics Research Section A **589**, 202-229 (2008)
- [54] A.Z. Schwarzschild et al., Annual Review of Nuclear Science **18(1)**, 265-290 (1968)
- [55] P.J. Nolan et al., Reports on Progress in Physics **42(1)**, 1 (1979)
- [56] F.G. Kondev et al., Atomic Data and Nuclear Data Tables **103**, 50-105 (2015)
- [57] V.F. Weisskopf et al., Physical Review **83(5)**, 50-105 (1951)
- [58] B.A. Brown et al., Annual Review of Nuclear and Particle Science **38(1)**, 29-66 (1988)
- [59] L. Coraggio et al., Progress in Particle and Nuclear Physics **62(1)**, 135-182 (2009)
- [60] V. Boldrini et al., Journal of Physics D: Applied Physics **52(3)**, 035104 (2019)
- [61] P.H. Regan et al., EPJ Web of Conferences **63**, 01008 (2013)
- [62] D.N. Grozdanov et al., Methods in Physics Research A **1014**, 165741 (2021)
- [63] V.Vedia et al., Nuclear Instruments and Methods in Physics Research A **857**, 98-105 (2017)
- [64] A. Camp et al., Applied Radiation and Isotopes **109**, 512-517 (2016)
- [65] B. Longfellow et al., Nuclear Instruments and Methods in Physics Research Section A **916**, 141-147 (2019)

- [66] O.B. Tarasov et al., Nuclear Instruments and Methods in Physics Research B **266**, 4657-4664 (2008)
- [67] J. Kurcewicz et al., Physics Letters B **717**, 371-375 (2012)
- [68] M. Pfützner et al., Physical Review C **65**, 064604 (2002)
- [69] Zs. Podolyák et al., Physics Letters B **632(2-3)**, 203-206 (2006)
- [70] M. Bowry et al., Physical Review C **88(2)**, 024611 (2013)
- [71] K.A. Gladnishki et al., Physical Review C **69(2)**, 024617 (2004)
- [72] J. J. Gaimard et al., Nuclear Physics A **531**, 709 (1991)
- [73] K. H. Schmidt et al., Nuclear Physics A **710**, 157 (2002)
- [74] A. Kelic et al., Proceedings of the Joint ICTP-IAEA Advanced Workshop on Model Codes for Spallation Reactions **530**, 181-221 (2008)
- [75] M. Berger, NIST, "XCOM: Photon Cross Sections Database" <http://physics.nist.gov/PhysRefData/Xcom/Text/XCOM.html>, (Site Visited December 2022).
- [76] O. Klein et al., Zeitschrift für Physik **52**, 853-868 (1929)
- [77] G.F. Knoll, "Radiation Detection and Measurement," John Wiley & Sons, New York, (2010)
- [78] T. Kajino, ResearchGate, "Current Status of r-Process Nucleosynthesis" <https://www.researchgate.net/publication/>, (Site Visited September 2022).
- [79] H. Geissel et al., Nuclear Instruments and Methods in Physics Research B **70**, 286-297 (1992)
- [80] J. Simpson et al., Zeitschrift für Physik A **358**, 139-143 (1997)
- [81] P.J.R. Mason et al., Physical Review C **88(4)**, 044301 (2013)
- [82] T. Daniel et al., Physical Review C **95(2)**, 024328 (2017)
- [83] S. Ilieva et al., Physical Review C **94(3)**, 034302 (2016)
- [84] J.M. Régis et al., Physical Review C **95(5)**, 054319 (2017)
- [85] P. Spagnoletti et al., Physical Review C **95(2)**, 021302 (2017)
- [86] P. Spagnoletti et al., Physical Review C **100(1)**, 014311 (2019)
- [87] E.R. Gamba et al., Physical Review C **100(4)**, 014311 (2019)

- [88] R.L. Canavan et al., Physical Review C **101(2)**, 024313 (2020)
- [89] M. Rudigier et al., Physical Review C **100(4)**, 014311 (2020)
- [90] G. Häfner et al., Physics Letters B **103(3)**, 034317 (2021)
- [91] G. Fruet et al., Physical Review Letters **124(19)**, 192701 (2020)
- [92] M. Heine et al., Nuclear Instruments and Methods in Physics Research Section A **903**, 1-7 (2018)
- [93] J. Ha et al., Physical Review C **101(4)**, 044311 (2020)
- [94] F. Browne et al., Physics Letters B **750**, 448-452 (2015)
- [95] A.D. Bacelar et al., Physical Letters B **723**, 302-306 (2013)
- [96] S.J. Steer et al., Physical Review C **84(4)**, 044313 (2011)
- [97] S. Agostinelli et al., Nuclear Instruments and Methods in Physics Research Section A **506(3)**, 250-303 (2003)
- [98] A. Matta et al., Journal of Physics G: Nuclear and Particle Physics **43** 045113 (2016)
- [99] M.M.R. Chishti et al., submitted to Nuclear Instruments and Methods in Physical Research A (2022)
- [100] G.S. Li et al., Nuclear Instruments and Methods in Physics Research Section A **987**, 164806 (2011)
- [101] B. Das et al., Physical Review C **105**, L031304 (2022)
- [102] O.J. Roberts et al., Nuclear Instruments and Methods in Physics Research Section A **748**, 91-95 (2014)
- [103] M.P. Taggart et al., Nuclear Instruments and Methods in Physics Research Section A **975**, 164201 (2020)